

AD-A280 942



(1)

DTIC
ELECTE
JUL 01 1994
S F D

A RADAR VECTOR SLOPE GAUGE FOR
OCEAN MEASUREMENTS

Vahid Hesany

Radar Systems and Remote Sensing Laboratory
Department of Electrical Engineering and Computer Science, University of Kansas
2291 Irving Hill Road, Lawrence, Kansas 66045-2969
TEL: 913/864-4835 * FAX: 913/864-7789 * OMNET: KANSAS.U.RSL

RSL Technical Report 8621-4

May 1994

164P6 94-20284



This document has been approved
for public release and sale; its
distribution is unlimited

Sponsored by:

Office of Naval Research
Arlington VA 22217-5000

Grant N00014-89-J-3221

ABSTRACT

The radar images of the ocean surface are modulated about the mean brightness by variations in radar signal associated with the large-scale ocean waves. Controlled radar experiments with simultaneous surface measurements allow quantifying the modulation of the radar signal by the ocean waves. Current attempts at describing this modulation often depend on point measurements of wave height. The important vector slope of the ocean must usually be derived either from point measurements and linear assumptions or from arrays of wave wires or pitch-and-roll buoys that cannot be in the radar footprint. We developed a 35-GHz vector slope gauge/scatterometer using a single switched-beam antenna. It can measure three adjacent height profiles of the ocean, from which we can derive two orthogonal components of the slope. We used the vector slope gauge during the North Sea SAXON-FPN experiment in November, 1990. Simultaneous measurements of the orthogonal components of the long-wave slopes and the backscattered power permit determination of the relative contribution to the overall modulation of the radar signal by slope modulation and hydrodynamic modulation of Bragg-resonant ripple amplitude.

Some examples of results are given.

Accession For	
NTIS	CRA&I <input checked="" type="checkbox"/>
DTIC	TAB <input type="checkbox"/>
Unannounced <input type="checkbox"/>	
Justification	
By	
Distribution /	
Availability Codes	
Dist	Avail and/or Special
A-1	

TABLE OF CONTENTS

Chapter 1: Introduction	8
Chapter 2: Basic Design Principles for Short-Range FM-CW Radars	14
2.1) Introduction	14
2.2) IF spectrum	17
2.3) The discriminator	23
2.4) Range accuracy	31
2.5) Other approaches to IF processing	34
2.6) Range side-lobes	39
2.7) IF spectrum for an extended target	43
2.8) Summary	48
Chapter 3: A Vector Slope Gauge and Scatterometer for Ocean	
Measurements	49
3.1) Introduction	49
3.2) Principle of operation	52
3.3) System block diagram	54
3.4) Summary	67

Chapter 4: SAXON-FPN Experiment and Data Analysis	68
4.1) Introduction	68
4.2) The SAXON-FPN experiment	70
4.3) Slope measuring principle and accuracy	75
4.4) Evaluation of orthogonal components of slope surface	78
4.5) Estimating the dominant wave direction	83
4.6) Modulation transfer functions at Ka band	90
4.7) Conclusion	95

Chapter 5: Measurement of Hydrodynamic Modulation of Radar

Scatter from the Sea	97
5.1) Introduction	97
5.2) The radar cross-section modulation	98
5.3) Tilt modulation	101
5.4) Short-wave spectra	102
5.5) A model for cross section modulation	105
5.6) First-order approximation of the hydrodynamic effects	109
5.7) Effects of the nonlinearities of σ_{tilt}^o	113
5.8) Some experimental results	127
5.9) Conclusions	133

Chapter 6: Conclusions and Recommendations	
6.1) Background	134
6.2) Vector slope gauge and its application	134
6.3) Measurements of MTF	135
6.4) Recommendations	137
Appendix A: The Vector Slope Gauge Hardware Documentation	143
References	167

Chapter 1

INTRODUCTION

The relatively recent advent of spaceborne radars has led to greatly increased interest in the nature of the microwave backscattering from the ocean. Remote sensing radars have the potential of measuring length, direction and height of the ocean waves, sea surface winds and direction over wide areal expanses. Obtaining environmental information from radar requires theoretical models of microwave scattering and understanding of the dynamics of the air-sea interface.

Controlled radar experiments accompanied by proper measurements of environmental parameters serve a dual purpose. (1) They allow verifying the theoretical scattering and boundary-layer models, and point out the range of applicability or the limitations of these models. (2) When theoretical models are inadequate, empirical models can be developed from the experimental data, thereby paving the way for new theoretical models. Many of the current applications of the radar remote sensing of the sea rely on a combination of both empirical and theoretical models.

The Real-Aperture Radar (RAR) and Synthetic-Aperture Radar (SAR) have attracted the most attention among the various microwave remote sensing instruments. RAR is the simplest of the two. RAR images are maps of the microwave intensity of a scene; changes in the average image intensity are

directly related to variations in the radar cross section of the surface. The main limitation of beam-limited RAR is its azimuthal resolution, which restricts it to aircraft applications (Ulaby, et al., 1982), except for gross resolutions such as obtained with the Okean series of spaceborne RARs (Kalmikov, et al., 1993). SAR has a much a finer resolution. It uses the Doppler-frequency-shift in the returns from the surface to synthesize a much larger aperture than its physical antenna. The fine resolution of SAR makes it ideal for spaceborne applications.

Both real- and synthetic-aperture images of the ocean show wavelike patterns. Consequently, efforts have been underway for more than a decade to explain the modulation of the signal strength, particularly as it applies to SAR. For a real-aperture radar system the modulation of the radar cross section by the large-scale waves is totally responsible for the formation of the wave images. For synthetic-aperture radar systems, the motion of the water associated with the large-scale waves is also important in the image formation. The first satellite devoted to remote observation of sea by SAR was SEASAT. It was launched by NASA in June 1978. Others including SIR-A, -B, and -C, ERS-1, and JERS-1 followed. These and many other experiments have clearly demonstrated the potential of SAR for imaging of the ocean waves. Ideally, one hopes to obtain a two-dimensional spectrum of ocean waveheights from the SAR images, but SAR imaging of ocean waves is still not fully understood, and many questions remain unanswered.

To understand the imaging process, one must understand the nature of microwave scattering from the ocean surface. In early wave-tank experiments with mechanically generated ripples of small magnitude, Wright(1968) demonstrated that only ripples with lengths comparable to the radar wavelength are primarily responsible for scattering. This scattering mechanism is commonly referred to as Bragg-resonant scattering. One often models the sea surface as small-scale ripples (capillary and short gravity waves) superimposed on the large-scale waves. The short ripples or Bragg waves riding on the large-scale waves are responsible for scattering. Wright (1968), Bass et al. (1968), Valenzuela (1978), and Ulaby, et al. (1982), used first-order perturbation techniques to derive microwave scattering from short ripples. This model is called composite-surface scattering or the two-scale scattering model. It may not be valid for high wind speeds where much of the surface is affected by breaking waves and wedge-shaped crests are common. Where it does apply, the scattering cross section depends on the local angle of incidence, on the small Bragg-resonant ripples, which are tilted by the large-scale wave slopes, and on variations in ripple amplitude.

Since the radar only "sees" the Bragg ripples, the long-waves are imaged through their modulation of the short ripples and the underlying slopes. To convert microwave scattering cross sections to wave parameters, one needs information about how large-scale waves affect Bragg ripples.

The modulation of microwave cross section by the large-scale ocean waves is due to two effects: (a) the tilt modulation and (b) the hydrodynamic-aerodynamic modulation. The tilt modulation is a purely geometric effect because ripples are seen by the radar at different local angles of incidence depending on their location on the long waves. The passing large-scale waves tilt the surface upon which the ripples reside, producing a new local angle of incidence, modifying the Bragg resonance wavelength. The hydrodynamic modulation is caused by interactions between ripples and large-scale waves. This results in a nonuniform distribution of the small-scale ripples of a given wavelength over the large-scale wave (Keller and Wright, 1975; Alpers and Hasselmann, 1978; Phillips, 1981). Aerodynamic effects, associated with wind turbulence driven by the large-scale waves, may also contribute to hydrodynamic modulation of ripples. Interactions between short and long waves, the hydrodynamic modulation, affect the backscatter strength by changing the amplitude of the Bragg ripple.

For low to moderate sea states, the linear model described by Wright (1980), Plant (1981), Alpers, et al.(1981) is often used to describe the modulation. The model assumes that the microwave-scattered power is linearly dependent, through the MTF, on the long-ocean-wave height or its slope, or, alternatively, the horizontal component of the orbital velocity. Transfer functions based on this model contain both tilt (or slope) and hydrodynamic-aerodynamic modulation.

Numerous experiments to measure the MTF have been conducted in recent years. These experiments involved measurements of radar signal strength and simultaneous measurements either of Doppler frequency shift of the radar signal or waveheight in the radar beam. These experiments have a major shortcoming in that they depend on point measurements of height or Doppler. Point height and Doppler measurements may be converted to slope if one assumes long-crested waves, with no slopes parallel to the crests, and also that linearity assumptions are valid. The actual slope modulation of the signal, however, depends on the vector slope, which also has components normal to the direction of wave travel.

In view of the difficulties with the current methods of measuring the ocean surface profile, the need for a new instrument capable of measuring the instantaneous slope of the long waves was apparent. Therefore, we designed a Vector-Slope-Gauge (VSG) to fulfill this need. It can measure two components of the long-wave slopes. With instantaneous measurements of slope and backscattering signal, one can remove the contribution of the tilt modulation to the overall radar-signal modulation and obtain estimates of the hydrodynamic modulation.

In Chapter 2, we outline the fundamental design principles of short-range FM-CW radars, particularly as they apply to the design of the VSG. The VSG system and its operation are described in Chapter 3. The VSG was operated during the SAXON-FPN experiment, which took place in November 1990, on the

German NORDSEE platform. Chapter 4 contains a description of the SAXON-FPN experiment. We also present an algorithm for extracting the orthogonal components of slope from the VSG measurements and present examples of the directional wave spectra measured by the VSG. In Chapter 5 we outline a new procedure for separating tilt and hydrodynamic modulations. Concluding remarks are contained in Chapter 6.

Chapter 2

BASIC DESIGN PRINCIPLES FOR SHORT-RANGE FM-CW RADARS

2.1) Introduction

Radar can measure range to distant targets by either amplitude, phase, or frequency modulating (FM) an RF carrier. Pulse modulation is the usual method of amplitude modulation. In pulse radars the round-trip delay between the transmitted pulse and its echo is the direct measure of the target range. In FM radars one uses the difference in transmitted and received signal frequencies to extract the range information. Any form of frequency modulation of the carrier can be used to obtain range information. The linear frequency modulation of the carrier has the distinct advantage that the difference frequency is directly proportional to range. This simplifies the design, analysis, and construction of the radar system.

In principle, the FM radar is similar to a pulse radar for range measurements. In a pulse radar, the time delay associated with the echo pulse is a direct measure of the range. For an FM-CW radar the frequency shift of the IF spectrum is proportional to the target range. Due to the duality of time and frequency, the two approaches theoretically yield the same performance. The major advantage of the FM-CW radar over the pulse radar is that it is simpler to implement. For the

same average power, the pulse radar requires higher peak power. FM radar is also more suitable for short ranges than the pulse radar. Pulse radars normally use duplexers or switches that turn off the receiver when a pulse is transmitted. This is done to protect the receiver during transmission. The duplexers add to the loss in the receiver channel, and the recovery time of the switch determines the minimum range at which an echo can be received. Thus, short-range pulse radars require low-loss fast duplexers. This and the use of very short pulses make the design of a short-range pulse radar and its data system more complicated and costly.

In the following discussion, we analyze the performance of FM radar with triangular frequency modulation. We also discuss some methods of IF signal processing for short-range FM radars. In the early sections, we focus on the point-target case, as this simplifies the analysis while providing good insight into the operation of the FM radar. In a latter section, we address the effect of an extended target on the radar performance.

Figure 2.1 shows the basic FM-CW radar system that we consider. The system consists of an RF oscillator, a triangular modulating waveform generator, a mixer, and a pair of transmitting and receiving antennas. The output of the mixer is the IF (Intermediate Frequency) signal.

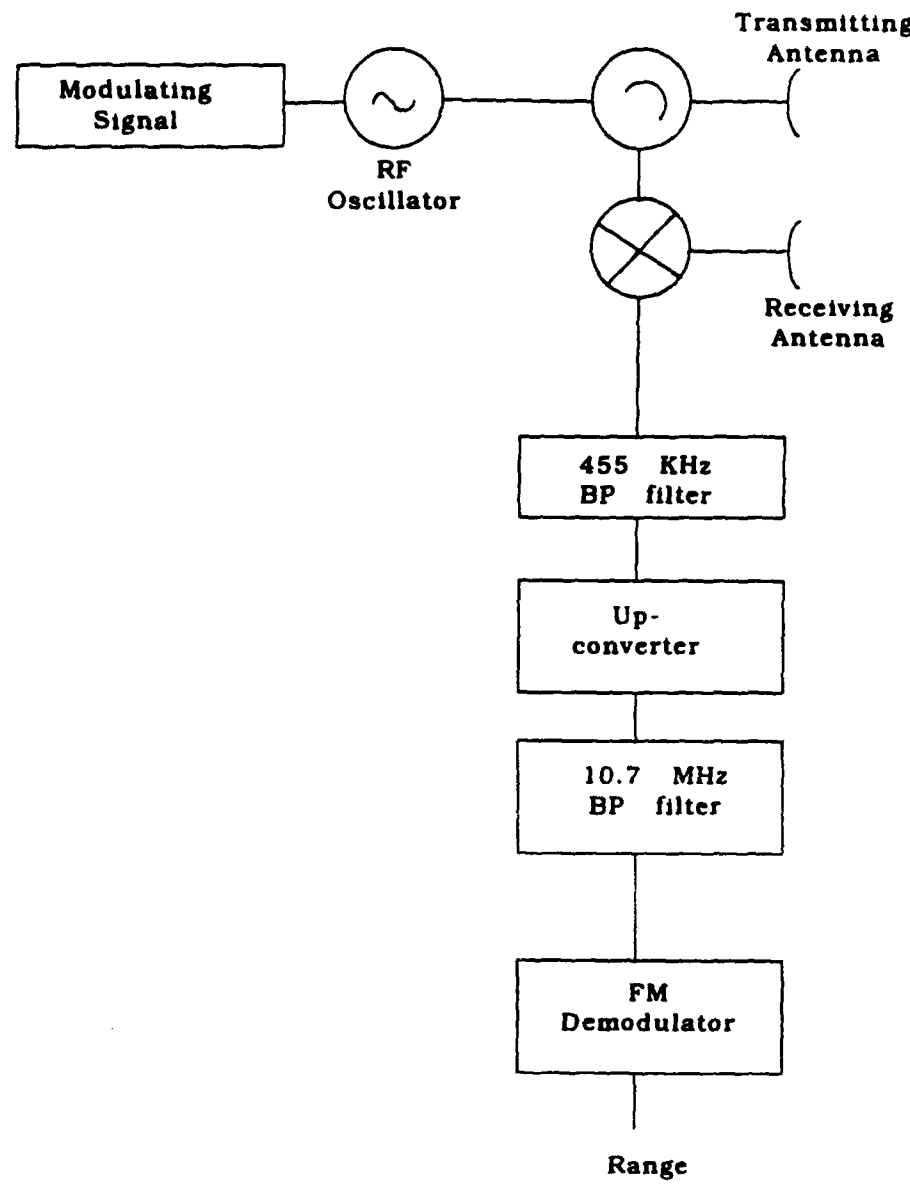


Figure 2.1) Basic FM-CW radar.

The resulting IF signal has a frequency offset proportional to the range to the target. The IF signal is then passed through a band-pass filter. For the VSG, the nominal frequency of the IF was around 455 KHz, and its bandwidth was limited by the band-pass filter to roughly 200 KHz. The VSG IF is upconverted to a higher frequency and then passes through a narrow-band 10.7-MHz bandpass filter. A limiter, following the bandpass filter, feeds the FM demodulator that produces the final output. The output of the demodulator is a voltage that is proportional to the IF signal frequency and, hence, the range to the surface. The importance of the upconversion is that it compresses the wide percentage-bandwidth IF signal to a narrow-band signal. For the VSG, the bandwidth compression ratio is $\frac{10.7 \text{ MHz}}{455 \text{ KHz}} = 23.5\%$.

2.2) IF spectrum

In this section we derive the expression for the IF spectrum of the FM-CW radar shown in Figure 2.1. The IF signal is periodic, having the same period as the modulating signal. We first find the continuous IF spectrum for one modulation period. The extension to the periodic case is straightforward, since the repetitive nature of the modulating signal replaces the continuous spectrum with a line spectrum, with the line spacing equal to the modulating signal period.

Figure 2.2 shows instantaneous transmitted frequency versus time. The frequency of the transmitted signal is linearly swept over an RF bandwidth B.

Each up-sweep is followed by an identical down-sweep. Figure 2.2 also shows the echo signal, which is a time-delayed replica of the transmitted waveform. The delay τ , due to the travel to and from the target is

(1)

$$\tau = 2R/c$$

where R is the range to the target and c is the velocity of light. The transmitted frequency for one modulation period is

$$\omega_T = \omega_o - 2\alpha t \quad -T_m/4 \leq t \leq T_m/4 \quad (2)$$

$$\omega_T = \omega_o - 2\alpha(t - T_m/2) \quad T_m/4 \leq t \leq 3T_m/4$$

where $\alpha = (2\pi B)/T_m$, and T_m is the modulation period. The modulation rate, or the FM rate, is $f_m = 1/T_m$. The instantaneous transmitted phase is

(3)

$$\phi_T = \int' \omega_T dt$$

which simplifies to

$$\phi_T = \omega_o t + \alpha t^2 + A_1 \quad -T_m/4 \leq t \leq T_m/4 \quad (4)$$

$$\phi_T = \omega_o t - \alpha t^2 + \alpha T_m t + A_2 \quad T_m/4 \leq t \leq 3T_m/4$$

where A_1 and A_2 are arbitrary constants.

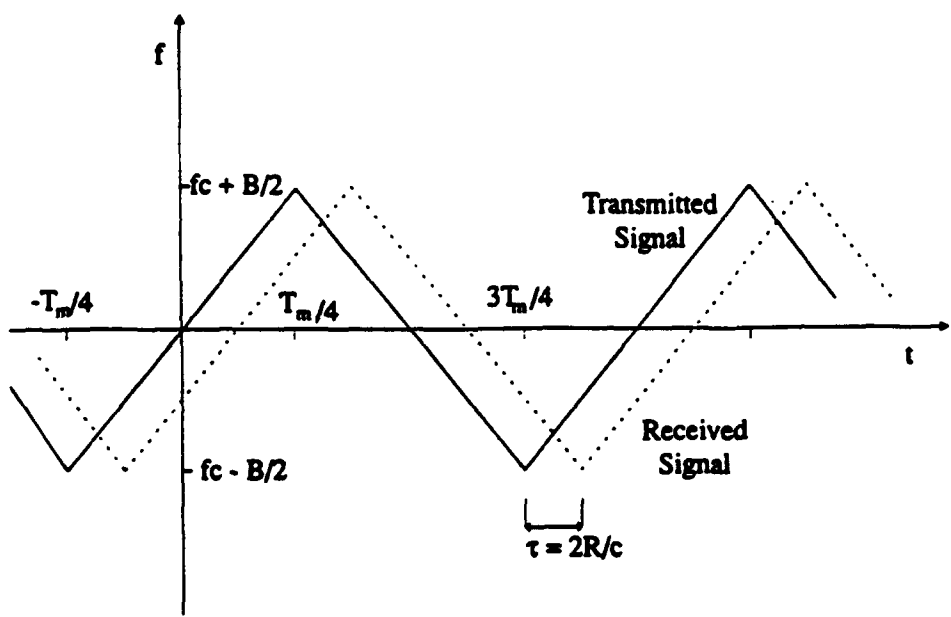


Figure 2.2 Instantaneous RF frequency.

The echo from the target has the form $v_R \cos(\phi_R)$, where ϕ_R is a delayed replica of ϕ_T . At the receiver, the transmitted and received signal are mixed. The phase of the lower-order product is

$$\begin{aligned}\phi_{IF} &= \phi_T(t) - \phi_R(t) \\ &= \phi_T(t) - \phi_T(t - \tau)\end{aligned}\tag{5}$$

At short ranges, the delay τ is small fraction of the modulation period T_m . For example, at 20m the delay is 130 ns while a typical modulation period is in the ms range. Thus, to a good approximation, we have

$$\begin{aligned}\phi_{IF} &= \phi_T(t) - \phi_T(t - \tau) \\ &\approx \tau \frac{d}{dt} \phi_T(t)\end{aligned}\tag{6}$$

This is the important property of the receiving process that results in an IF phase modulation that is proportional to the derivative of the transmitting phase. For the periodic triangular modulation of Figure 2.2, the IF phase modulation is a periodic square wave. Sinusoidal phase modulation of the transmitted signal produces an IF phase that is also sinusoidally modulated. Substituting (4) into (6), we obtain

$$\begin{aligned}\phi_{IF} &= C_1 + 2\alpha t \tau & -T_m/4 \leq t \leq T_m/4 \\ \phi_{IF} &= C_2 - 2\alpha t \tau & T_m/4 \leq t \leq 3T_m/4\end{aligned}\tag{7}$$

where $C_1 = \omega_o \tau$ and $C_2 = \omega_o \tau + \alpha \tau T_m$ are constants.

The IF spectrum for one modulation period is

$$F_{IF}(\omega) = \int e^{j\theta_m} e^{-j\omega t} dt \quad (8)$$

or

$$\begin{aligned} F_{IF}(\omega) &= \int_{-T_m/4}^{T_m/4} e^{j(C_1 + 2\alpha\tau)} e^{-j\omega t} dt \\ &\quad + \int_{T_m/4}^{3T_m/4} e^{j(C_2 - 2\alpha\tau)} e^{-j\omega t} dt \end{aligned} \quad (9)$$

Carrying out the integration, we obtain

$$\begin{aligned} F(\omega) &= e^{jC_1} \frac{T_m \sin[(2\alpha\tau - \omega)T_m/4]}{2(2\alpha\tau - \omega)T_m/4} \\ &\quad + e^{jC_2} e^{-j(\omega - 2\alpha\tau)T_m/2} \frac{T_m \sin[(2\alpha\tau + \omega)T_m/4]}{2(2\alpha\tau + \omega)T_m/4} \end{aligned} \quad (10)$$

The above equation is the Fourier transform of the IF signal over one period. The IF signal is a periodic waveform with a period of T_m . The Fourier transform of a periodic signal is also periodic and consists of a set of equally spaced impulses located at the harmonic frequencies of the signal. Mathematically, this is expressed as

$$\hat{F}(\omega) = \frac{2\pi}{T_m} F(\omega) \sum_{n=-\infty}^{\infty} \delta(\omega - \frac{2\pi n}{T_m}) \quad (11)$$

where $F(\omega)$ is the Fourier transform of the signal over one period, T_m is the period, and $\hat{F}(\omega)$ is the Fourier transform of the periodic signal.

From (10) and (11), the power spectrum of the IF signal for positive

frequencies is given by

$$G_{IF}(\omega) \triangleq 2 |\hat{F}(\omega)|^2 \quad \text{for } \omega \geq 0 \quad (12)$$

$$= 2\pi^2 \sum_n \text{sinc}^2 [(\omega - 2\alpha\tau)T_m/4] \delta(\omega - 2\pi n/T_m)$$

where for simplicity we have used the short-hand notation $\text{sinc}(x) = \sin(x)/x$.

The IF spectrum is symmetrical and its center is proportional to the range to the target. The center of the spectrum is at

$$\begin{aligned} \omega_{IF} &= 2\pi f_{IF} \\ &= 2\alpha\tau \\ &= 2\pi \frac{4BR}{cT_m} \end{aligned} \quad (13)$$

We find the width of the main lobe by observing that $G_{IF}(\omega) = 0$, when

$$\frac{(\omega_n - 2\alpha\tau)T_m}{4} = n\pi \quad (14)$$

so that the width of the main lobe is

$$\begin{aligned} \text{null-to-null spacing} &= 2\pi \left(\frac{4}{T_m} \right) \\ &= 2\pi(4f_m) \text{ radians/s} \end{aligned} \quad (15)$$

This indicates that the width of the main lobe depends only on the FM rate and is independent of other system parameters. From (12), the 3-dB IF bandwidth (the half-power width) is approximately

$$B_{IF} \approx 0.88 f_m \quad (16)$$

The IF spectrum in (12) can also be expressed in terms of the target range. Using (12) and noting that (13) relates the IF frequency to the range, we can write

the point-target range response as

$$G(R) = 2\pi^2 \sum_{n=0}^{\infty} \text{sinc}^2 [(R - R_o)2\pi B/c] \delta(R - nc/4B) \quad (17)$$

where R_o is the range to the point target. The null-to-null width of the main lobe is $\frac{c}{B}$. The quantity $\frac{c}{2B}$ is commonly referred to as the range resolution of the FM radar.

The center of the IF spectrum is a direct measure of target range. To extract the range information, one usually employs some type of frequency-to-voltage converter or frequency demodulator. A widely used circuit is the frequency discriminator. In the next section, we will discuss the behavior of this circuit.

2.3) The discriminator

A common circuit for demodulating the FM signal is the frequency discriminator. Figure 2.3 shows the block diagram of an ideal frequency discriminator. An ideal frequency demodulator clearly must have a linear frequency-to-voltage characteristic. The differentiator with the transfer function $H(j\omega) = j\omega$ provides the desired linear amplitude-versus-frequency characteristic. For a single sine wave it is easy to see that the output of the discriminator is proportional to the input frequency. For a single sinusoid $x_{IF}(t) = A \sin(\omega t)$

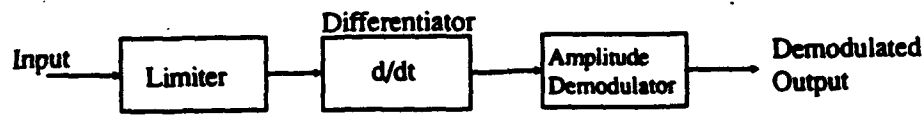


Figure 2.3. An ideal discriminator.

the differentiator output is $A\omega\cos(\omega t)$. The input limiter removes any amplitude variations by setting the amplitude to a constant. The amplitude demodulator, following the differentiator, removes the carrier term. The final output is $A\omega$, and since A is a constant due to the action of the limiter, it is directly proportional to the input-signal frequency.

Most of the existing frequency discriminators are designed to approximate, as closely as possible, the action illustrated by the block diagram. The differentiator can be approximated in either time or frequency domain.

The simplest realization of the frequency-domain differentiator is the resonant RLC circuit. The ideal differentiator is approximated by tuning the RLC circuit such that the input FM signal is centered on the sloping portion of the transfer function. Over a small range of frequencies, the transfer function approximates the desired linearly sloping magnitude. This type of discriminator is commonly referred to as a slope detector or slope demodulator. The single-ended circuit using a single tuned circuit has a limited linear range and, hence, bandwidth. To extend the bandwidth, one uses the difference between two single-ended slope demodulators, with one tuned above and the other below the nominal carrier frequency. This type of configuration provides zero output at the carrier frequency in addition to improved sensitivity and linearity. Amplitude demodulation, following the differentiator, is usually accomplished by a bank of diodes and capacitors. A popular example of this type of frequency demodulator is

the Foster-Seeley discriminator.

Another approach to approximating the action of the ideal differentiator is to directly implement the time-domain definition of the derivative, that is,

$$\frac{dx(t)}{dt} = \frac{x(t) - x(t - t_d)}{t_d} \quad \text{for } t_d \ll 1 \quad (18)$$

Figure 2.4 shows a general block diagram for a discriminator using a time-delay differentiator. Usually, a tuned resonant circuit provides the time delay t_d as well as the phase shift of $-\pi/2$ at the carrier frequency. A tuned circuit near resonance provides an almost constant phase characteristic over a wide bandwidth and, thus, closely approximates an ideal delay line. In Figure 2.4, the last two blocks represent the synchronous detector that performs the required amplitude demodulation. For synchronous detection the differentiated input signal is multiplied by the quadrature reference signal, and the resulting signal is then passed through a low-pass filter. This approach to frequency demodulation provides high sensitivity and linearity, while avoiding the multiple-tuning problems associated with frequency-domain discriminators. An integrated 10.7-MHz differential-pair discriminator based on this method is the RCA-CA3189. Due to its superior performance, this circuit was adapted into the VSG to perform the necessary frequency demodulation. The integrated circuit, in addition to the differentiator and quadrature detector, includes an input limiter and an output amplifying stage.

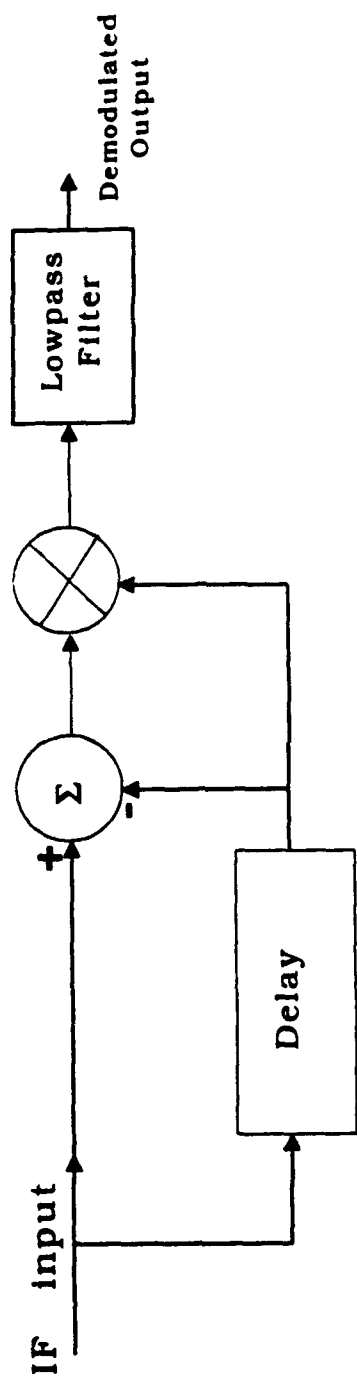


Figure 2.4 Block diagram of time-delay differentiator.

The IF signal of the FM radar consists of the sum of many sinusoidal signals that are present simultaneously at the input of the discriminator. To derive an expression for the discriminator output, we write the IF signal as

$$x_{IF}(t) = \sum_i a_i e^{j\omega_i t} \quad (19)$$

The corresponding IF spectrum is

$$G_{IF}(\omega) = \sum_i a_i^2 \delta(\omega - \omega_i) \quad (20)$$

The output of the discriminator is given by

$$x_d(t) = \left| \frac{dx_{IF}}{dt} \right| \quad (21)$$

Ignoring the high-frequency terms, the above expression simplifies to

$$x_d(t) = \left[\sum_i a_i^2 \omega_i^2 \right]^{1/2} \quad (22)$$

We are interested in expressing the discriminator output in terms of the input spectrum, so we rewrite the above equation as

$$\begin{aligned} x_d(t) &= \left[\sum_i a_i^2 \omega_i^2 \right] \\ &= \left[\sum_i \int \omega^2 a_i^2 \delta(\omega - \omega_i) d\omega \right]^{1/2} \\ &= \left[\int \omega^2 G(\omega) d\omega \right]^{1/2} \end{aligned} \quad (23)$$

The output of the discriminator is therefore proportional to the second moment of the input spectrum. The limiter ahead of the discriminator removes any dependence on the input signal amplitude. To incorporate the action of the

limiter, we write the final discriminator output as

$$x_d = K_D \left[\frac{\int \omega^2 G(\omega) d\omega}{\int G(\omega) d\omega} \right]^{1/2} \quad (24)$$

Where K_D is the discriminator gain. We demonstrated that for FM radar the IF power spectrum for one sweep is continuous and has the form $\sin^2(x)/x^2$. To simplify the notation let $\omega_r \triangleq 2\alpha\tau = \frac{4BR}{cT_m}$, then

$$G_{IF}(\omega) = A^2 \frac{\sin^2[(\omega - \omega_r)T_m/4]}{[(\omega - \omega_r)T_m/4]^2} \quad (25)$$

The discriminator output is given by

$$x_d = K_D \left[\frac{\int_{\omega_r - \Delta\omega/2}^{\omega_r + \Delta\omega/2} \omega^2 G_{IF}(\omega) d\omega}{\int_{\omega_r - \Delta\omega/2}^{\omega_r + \Delta\omega/2} G_{IF}(\omega) d\omega} \right]^{1/2} \quad (26)$$

where $\Delta\omega$ is the IF bandwidth and its value is set by the narrow band-pass filter preceding the discriminator. Evaluating the integrals, and after simplifying we obtain

$$x_d = K_D \left[\frac{2\Delta\omega}{T_m \omega_r^2} \frac{\left[1 - \frac{\sin(\Delta\omega T_m/4)}{\Delta\omega T_m/4} \right]}{\text{si}^2(\Delta\omega T_m/8)} + 1 \right]^{1/2} \omega_r \quad (27)$$

Where $\text{si}^2(z)$ is defined by $\int_{-z}^z \sin^2(z)/z^2 dz$. Note that the square of the

discriminator output is linearly related to ω_r^2 and, hence, to the square of the range to the target. Due to square-root operation, the discriminator output is proportional to ω_r^2 only when the first factor in the large bracket is negligible. For typical design values for the vector slope gauge $\Delta\omega = 2\pi \times 200 \times 10^3$ Hz, $T_m = 0.38$ msec,

and $\omega_r = 2\pi \times 10.7 \times 10^6$ KHz, the multiplying factor $\frac{2\Delta\omega}{T_m \omega_r^2} = 1.5 \times 10^{-6} < 1$.

Therefore, to a very good approximation

$$x_d \approx K_D \omega_r \quad (28)$$

This indicates that the discriminator produces an output that is directly proportional to the frequency at the peak of the IF spectrum. For proper behavior of the discriminator, two conditions must be satisfied: a) the discriminator input signal should be symmetrical, and b) the input spectrum must be narrow-band.

2.4) Range accuracy

Accuracy of the range measurement is clearly an important design consideration. Usually, one expresses the accuracy in terms of the IF signal-to-noise ratio. Our purpose here is to examine the effects of band-limited white noise on the range measurement.

Barton et al. (1984) show that the minimum possible error in time-delay measurement for a signal pulse is

$$(\sigma_t)_{\min} = \frac{\tau_o}{1.63 \sqrt{\mathfrak{R}}} \quad (29)$$

where τ_o is the half-power pulse width, and \mathfrak{R} is the ratio of twice the total single-pulse energy to the input noise power per unit bandwidth. Since $\sigma_R = c\sigma_t/2$, the minimum error in range measurement is

$$\begin{aligned} (\sigma_R)_{\min} &= \frac{c}{2} \frac{\tau_o}{1.63 \sqrt{\mathfrak{R}}} \\ &= \frac{r_R}{1.63 \sqrt{\mathfrak{R}}} \end{aligned} \quad (30)$$

where $r_R = c\tau/2$ is the range resolution. This is the optimum accuracy of a pulse radar. Due to the duality of FM and pulse radars, we expect that an FM radar using an optimum IF processor will provide the same level of performance.

An optimum processor normally involves a matched filter or a cross-correlator for extracting the range information. The VSG is clearly not optimum since it uses an open-loop discriminator for measuring the range.

To derive an expression for the range accuracy of the VSG we assume that the discriminator is ideal and that the noise at the discriminator input is ideal bandpass with spectrum

$$G_n(\omega) = \begin{cases} S_n/2 & \text{for } \omega_r - \Delta\omega/2 \leq |\omega| \leq \omega_r + \Delta\omega/2 \\ 0 & \text{otherwise} \end{cases} \quad (31)$$

where ω_r is the nominal IF frequency and $\Delta\omega$ is the IF bandwidth. The factor of one-half in the above equation indicates that we will deal with the two-sided power spectrum density. This means that, for positive frequencies, the power spectral density of noise is S_n watts per Hz.

The discriminator output is given by

$$x_d = \left[\frac{\int \omega^2 [G_{IF}(\omega) + G_n(\omega)] d\omega}{\int [G_{IF}(\omega) + G_n(\omega)] d\omega} \right]^{1/2} \quad (32)$$

Evaluating the integrals and using the result in (30) and (31), we obtain

$$x_d = \left[\frac{S_o \omega_r^2 + \frac{S_n \Delta\omega}{6} \left(\frac{\Delta\omega^2}{4\omega_r^2} + 3 \right) \omega_r^2}{S_o + S_n \Delta\omega} \right]^{1/2} \quad (33)$$

where S_o is the total IF signal power. Assuming that the noise is small, i.e., IF signal-to-noise ratio is much greater than 1, and applying the narrow-band approximation, we have

$$x_d = \left[\frac{S_o \omega_r^2 + \frac{S_n}{2} \Delta\omega \omega_r^2}{S_o} \right]^{1/2} \quad (34)$$

The second term in the numerator is the error due to the noise. In terms of signal-to-noise ratio \mathfrak{R} , we have

$$\sigma_w = \frac{\Delta\omega}{\sqrt{\mathfrak{R}}} \quad (35)$$

The error in frequency measurement is related to the range error by

$$\sigma_r = \frac{c T_m}{(2\pi)4B} \sigma_w \quad (36)$$

Substituting (35) into (36), and substituting the expression for the IF bandwidth from (16), after simplifying we obtain

$$\begin{aligned} \sigma_r &= \frac{0.88 c}{2B \sqrt{\mathfrak{R}}} \\ &= \frac{r_r}{1.14 \sqrt{\mathfrak{R}}} \end{aligned} \quad (37)$$

Comparing the above equation with (30), we note that there is little degradation in performance compared with the optimum. The above equation is valid only for high signal-to-noise (S/N) ratio, and assumes that we are operating over a narrow IF bandwidth. Furthermore, we have expressed the results in terms of the S/N ratio at the input of the discriminator. The discriminator is preceded by the limiter. Gardner (1967) shows that S/N is reduced by a factor of $\pi/4$ when the signal passes through the limiter. Considering all these factors, we conclude that the loss due to sub-optimal processing is of the order of 3 dB in terms of signal-to-noise ratio.

The sensitivity of our range measurement is also an important design

parameter. We define the sensitivity as the change at the discriminator output for an incremental change in range, or

$$\begin{aligned} S_r &= \frac{\Delta x_d}{\Delta R} \\ &= K_D \frac{\Delta \omega_r}{\Delta R} \\ &= 2\pi K_D \frac{4Bf_m}{c} \end{aligned} \tag{38}$$

Note the S_r is independent of range, and is directly proportional to the RF bandwidth, FM rate, and the discriminator gain K_D .

2.5) Other approaches to IF processing

In addition to the open-loop tracking that we have discussed so far, there are a number of other approaches to extracting the range information. In this section, we briefly discuss some of these methods.

A popular approach is a closed-loop system commonly referred to as the *range tracker*. The range tracker has been implemented in many of the FM radars built at the Remote Sensing Laboratory of The University of Kansas. Examples include TRAMAS and the HEOSCAT radars. Milberger (1973) describes the original design of the range tracker.

Figure 2.5 show a block diagram of the range tracker. The circuit operates as follows. As the range to the target changes, the IF spectrum attempts to drift from its steady-state value. The discriminator detects this change and outputs an

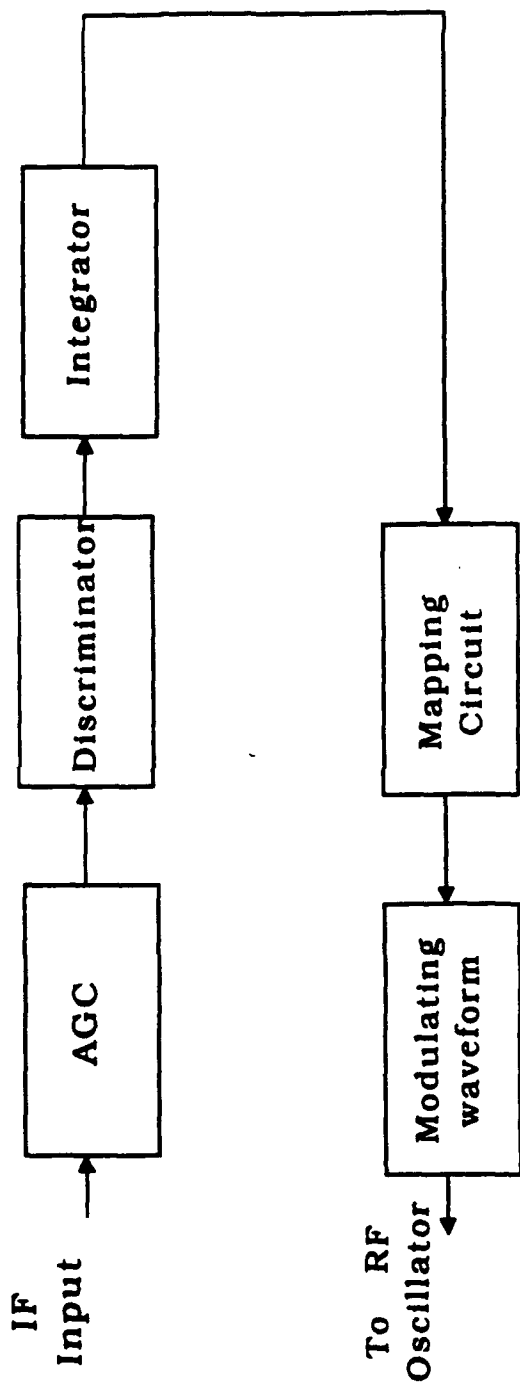


Figure 2.5 Range tracker block diagram.

error voltage proportional to the frequency drift. The error voltage feeds the VCO, which varies accordingly the FM rate of the modulating signal, which in turn forces the centroid of the IF spectrum to its steady-state constant value. The frequency excursions of the modulating triangular wave are then a measure of the target range. A frequency-to-voltage (f/v) converter is then used to convert the frequency excursions to voltages. Usually, an A/D digitizes the f/v output and a computer records the samples for further processing.

From (11), the centroid of the IF frequency is located at $f_{IF} = 4BRf_m/c$. To keep the IF constant, the loop responds to a change in range δR by varying the FM rate by δf_m . Therefore,

$$\begin{aligned}
 f_{IF} &= \frac{4B}{c} R f_m \\
 &= \frac{4B}{c} (R_o + \delta R) (f_{m_0} + \delta f_m) \\
 &= \frac{4B}{c} (R_o f_{m_0} + R_o \delta f_m + \delta R f_{m_0}) \\
 &= f_o + f_R + f_e
 \end{aligned} \tag{39}$$

Where f_o is the nominal or the desired IF, f_R is the frequency shift due to change in range and f_e is the correction term due to the feedback loop. The output of the discriminator is

$$x_D = -K_D (f_R + f_e) \tag{40}$$

where K_D is the conversion gain of the discriminator. The discriminator output then passes through an integrator. For simplicity we assume that the integrator has

enough bandwidth to pass the components at frequencies f_R and f_e . Therefore, the output of the discriminator is

$$(41) \quad x_i = -K_D K_I (f_r + f_e)$$

where K_I is the gain of the integrator. To produce the term f_m at the VCO output, the integrator output must have the value f_m / K_{vco} as well as $-K_D K_I (f_R + f_m)$; therefore

$$(42) \quad \frac{f_e}{K_{vco}} = -K_D K_I (f_R + f_e)$$

or

$$(43) \quad f_e = \frac{-f_m}{1 + \frac{1}{K_D K_I K_{vco}}}$$

Since the gain of the integrator K_I is very large for frequencies near f_e , we get $f_e = -f_R$. From (39), we obtain $f_{IF} = f_o = \text{constant}$, which is the desired result.

The major advantage of the feedback loop is that the range tracker maintains the centroid of the IF spectrum at constant value. This permits the IF to fall within the passband of a narrow-band filter. Therefore, the IF bandwidth needs to be only wide enough to pass the received signal, thus reducing the effects of noise.

For the range tracker, the loop sensitivity is

$$\begin{aligned}\frac{df_m}{dR} &= \frac{-cf_o}{4BR^2} \\ &\approx -\frac{R_o}{R^2}f_m \\ &\approx -\frac{f_m}{R}\end{aligned}\tag{44}$$

The sensitivity depends inversely on the target range and is independent of the RF bandwidth. The sensitivity is directly proportional to FM rate. Therefore, higher sensitivity is achieved at the expense of higher FM rate and therefore higher nominal IF. For example, for a range tracker operating at 50 KHz, with the RF bandwidth of 500 MHz, the sensitivity at 25m is

$$\left| \frac{\Delta f_m}{\Delta R} \right| = \frac{cf_o}{4BR^2} \approx 12 \text{ Hz/m}\tag{45}$$

To achieve an accuracy of 1 cm, the f/v must resolve 0.12 Hz, which requires averaging over a very long period. This certainly limits the achievable range accuracy. To improve the sensitivity, one should operate the loop at a higher IF or FM rate.

Another approach that can improve the sensitivity is to perform the range tracking at the IF level. In this scheme, a local VCO upconverts the IF signal to a higher frequency where it is demodulated by a discriminator. The discriminator

output is the error signal that drives the local VCO. The loop operates by adjusting the local VCO frequency so that the center of the IF spectrum at the discriminator input is maintained at a constant frequency. The error signal at the discriminator output is then proportional to range and can be directly digitized and stored for further processing. The cost of adding an additional local VCO is offset by the fact that an f/v converter is no longer needed to detect the frequency variations in the triangular modulating signal. In addition to improving the sensitivity of the range measurement, this scheme has the advantage that the modulating triangular frequency, the FM rate, is kept constant.

2.6) Range sidelobes

From (12), we note that the IF spectrum has the $(\sin x/x)^2$ form as a result of rectangular phase modulation. The first sidelobe is 13 dB below the peak of the main lobe, and the sidelobes level falls off at a slow rate of 6 dB per octave. This means that the performance of short-range FM radar is seldom if ever limited by thermal noise. Internal reflections within the transmitter, especially the reflection from the antenna port, appear as very strong targets at short ranges. Sidelobes of these interfering signals can easily mask the weak returns from short-range targets. The reflection from the antenna is particularly troublesome due to the relatively high VSWR at the antenna port. The situation can be improved by using separate transmitting and receiving antennas. For the VSG, the use of

separate transmitting and receiving antennas resulted in roughly 25-dB improvement in signal-to-sidelobe ratio.

The range sidelobes can be further reduced by applying proper amplitude tapering. One can apply the weighting in either time or frequency domain. In time-domain weighting, the amplitude of the IF signal is multiplied by an appropriate window function, which is normally derived from the modulating waveform. Frequency-domain weighting can produce identical results. In this approach, the amplitude of the modulating signal (the periodic triangular waveform) is properly weighted to produce the desired sidelobe level. In practice, the frequency-domain weighting is much easier to implement than the time-domain/IF weighting. With IF weighting one must deal with frequencies that are higher by several orders of magnitude than the modulating signal frequencies. This makes the weighting at the IF level more difficult to implement. Furthermore, the frequency-domain approach offers the advantage of combining the actions of amplitude-weighting and linearizing the FM sweep into one circuit.

It is relatively easy to see the principle behind the frequency-domain weighting. From (6), we note that the frequency of the IF signal is proportional to the derivative of the modulating signal. For linear triangular modulation, the resulting phase modulation is a square wave that results in the familiar $(\sin x/x)^2$ sidelobe amplitudes for the IF power spectrum. This suggests a simple method of synthesizing the modulation signal by specifying the sidelobe level. For example,

for Hanning pulses the first sidelobe is 42.8 dB below the peak of the main lobe.

The Hanning pulse is given by

$$W(t) = \frac{1}{2} \left[1 - \cos\left(\frac{2\pi t}{T_m/2}\right) \right] \quad 0 \leq t \leq T_m/2 \quad (46)$$

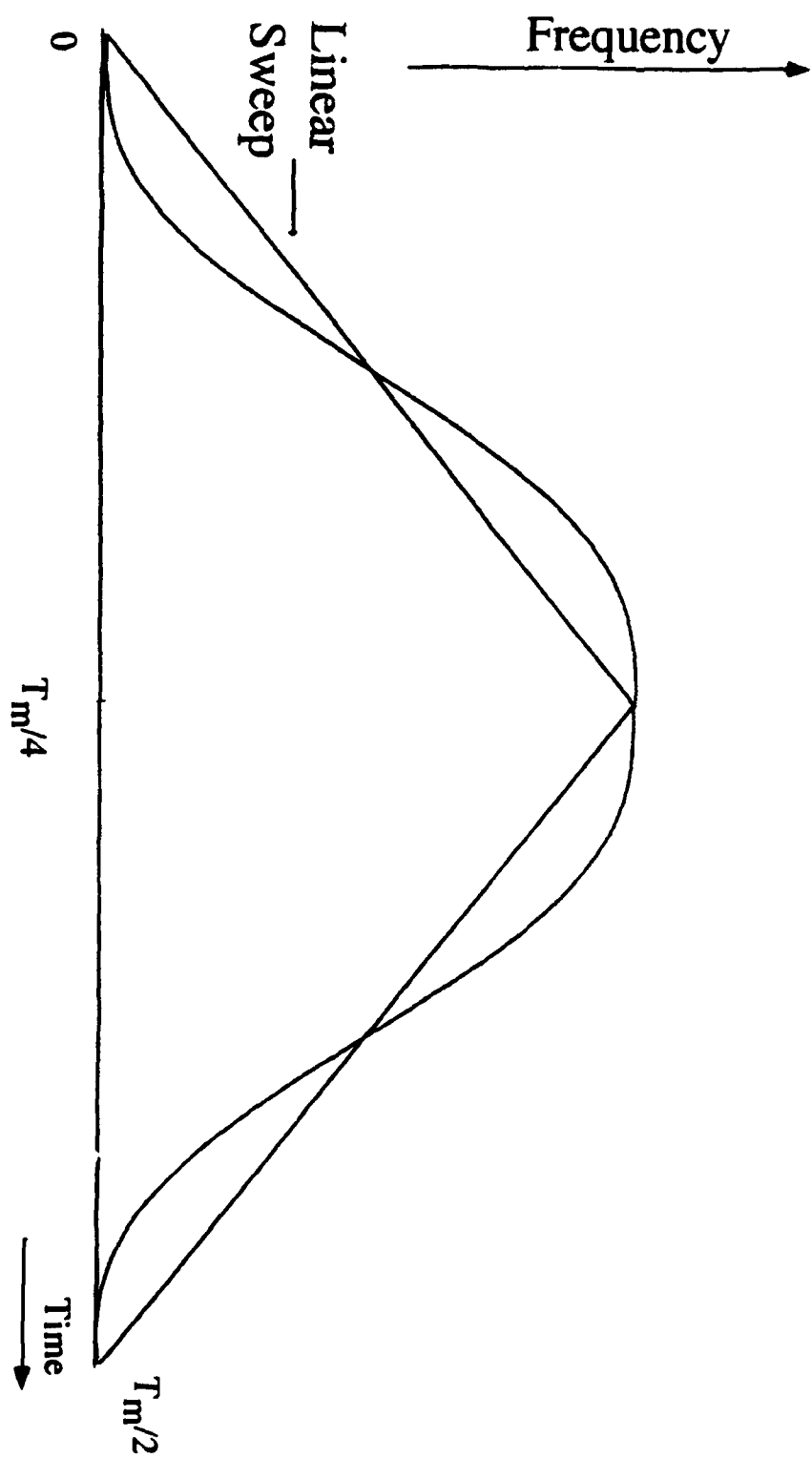
Therefore, from (6) we obtain the modulating waveform as

$$\begin{aligned} f_T(t) &= \int_t W(t) dt \\ &= \frac{t}{2} - \frac{T_m}{2\pi} \sin\left(\frac{2\pi t}{T_m/2}\right) \quad 0 \leq t \leq T_m/2 \end{aligned} \quad (47)$$

where T_m is the modulation period. Figure 2.6 compares the linear triangular sweep with the Hanning sweep given by (47).

Since the modulating signal in (47) has long duration it can be easily generated either digitally or using analog circuitry. The digital approach is probably simpler to implement. The predefined waveform can be stored in memory, and the same configuration can be used to generate other types of waveforms. The digital approach also provides very stable and consistent results under a wide variety of operating conditions.

Figure 2.6 Comparison of linear and Hanning sweeps.



2.7) IF spectrum for an extended target

Up to this point, we have carried out most of the analysis for a single-point target. For an area-extensive target such as the ocean surface, one assumes that the received signal from the surface is due a large number of independent scatterers. The surface illuminated by the radar has a finite area that is determined by the antenna footprint. Since the range to each scatterer within the antenna footprint is different, a spectrum of ranges around the nominal range frequency appears at the radar output. Normally, the assumption is made that the radar measures the range to the centroid of the antenna footprint. This results in a bias error in the measurement of range since the radar measures a weighted average of all ranges within the antenna footprint.

Due to the complexity of the results, a closed-form solution is not possible. We will carry the analysis only far enough to provide some insight into the problem. Of course, one can always obtain a solution by numerical techniques, but that is beyond the scope of this work.

The problem that we are considering here is similar to the problem of calculating the Doppler spectrum for a side-looking radar (Ulaby, et al., 1982). In general, one usually assumes that on the average, the total scattered power from the surface is the sum of the power received from each individual scatterer. This is due to the fact that the phase angle associated with the return from each scatterer is uniformly distributed and it is independent from those of the other

returns (Ulaby, et al., 1982).

We define the range spectrum $F(R)$ as the power obtained from the area between ranges R and $R+dR$.

$$dP_R = F(R) dR \quad (48)$$

The power from an incremental area dA is given by the radar equation.

$$dP_A = \frac{P_t G^2 \sigma^o \lambda^2}{(4\pi)^3 R^4} dA \quad (49)$$

where

P_t is the transmitted power

σ^o is the radar cross section per unit area

G is the antenna gain

λ is the wavelength of the transmitter

Rauch et al. (1971) performed a similar analysis for a high-altitude altimeter with the antenna pointed vertically down. Modifying his derivations, we have

$$F(R) = \frac{P_t \lambda^2 \sigma^o}{(4\pi)^3 R^3} \int_{-\pi}^{\pi} G^2(\theta, \alpha) d\alpha \quad (50)$$

where θ is the elevation angle, and α is the azimuth angle. In general, the above integral cannot be evaluated in closed form. A computer solution can be obtained by evaluating the integral numerically. To gain insight into the behavior of the function $F(R)$, we make the common assumption that the antenna gain can be separated into components in the θ (vertical) and α (azimuth) directions (Ulaby, et

al., 1982), that is

$$G^2(\theta, \alpha) = g_o^2 g_\theta^2(\theta) g_\alpha^2(\alpha) \quad (51)$$

where $g_\theta(\theta)$ and $g_\alpha(\alpha)$ are the normalized patterns and g_o is the maximum gain. From (50) and (51), we obtain

$$\begin{aligned} F(R) &= \frac{P_o \lambda^2 \sigma^o g_o g_\theta^2(\theta)}{(4\pi)^3 R^3} \int_{-\pi}^{\pi} g_\alpha^2(\alpha) d\alpha \\ &= C \frac{g_\theta^2(\theta)}{R^3} \end{aligned} \quad (52)$$

where C includes all the constant terms, and $R = h / \cos(\theta)$ relates the incidence angle θ to R where h is the antenna height.

For simplicity, we assume that the antenna pattern has the form $[\sin(x)/x]^2$. Then, (Ulaby, et al., 1982)

$$g_\theta(\theta) = \left[\frac{\sin(2.784(\theta - \theta_o)/\Delta\theta)}{2.784(\theta - \theta_o)/\Delta\theta} \right]^2 \quad (53)$$

where θ_o is the incidence angle, and $\Delta\theta$ is the 3-dB beamwidth. Figure 2.7 shows a plot of $F(R)$ for a typical VSG antenna configuration, namely, angle of incidence $\theta = 45^\circ$, $\Delta\theta = 2^\circ$, and a height of 20 m. The actual measured range is proportional to the second moment of $F(R)$. For the example in Figure 2.7, this results in a measured value of roughly $R_m = 28.293$ m. The bias in the range measurement is due to the fact the one assumes that all the power is from a point

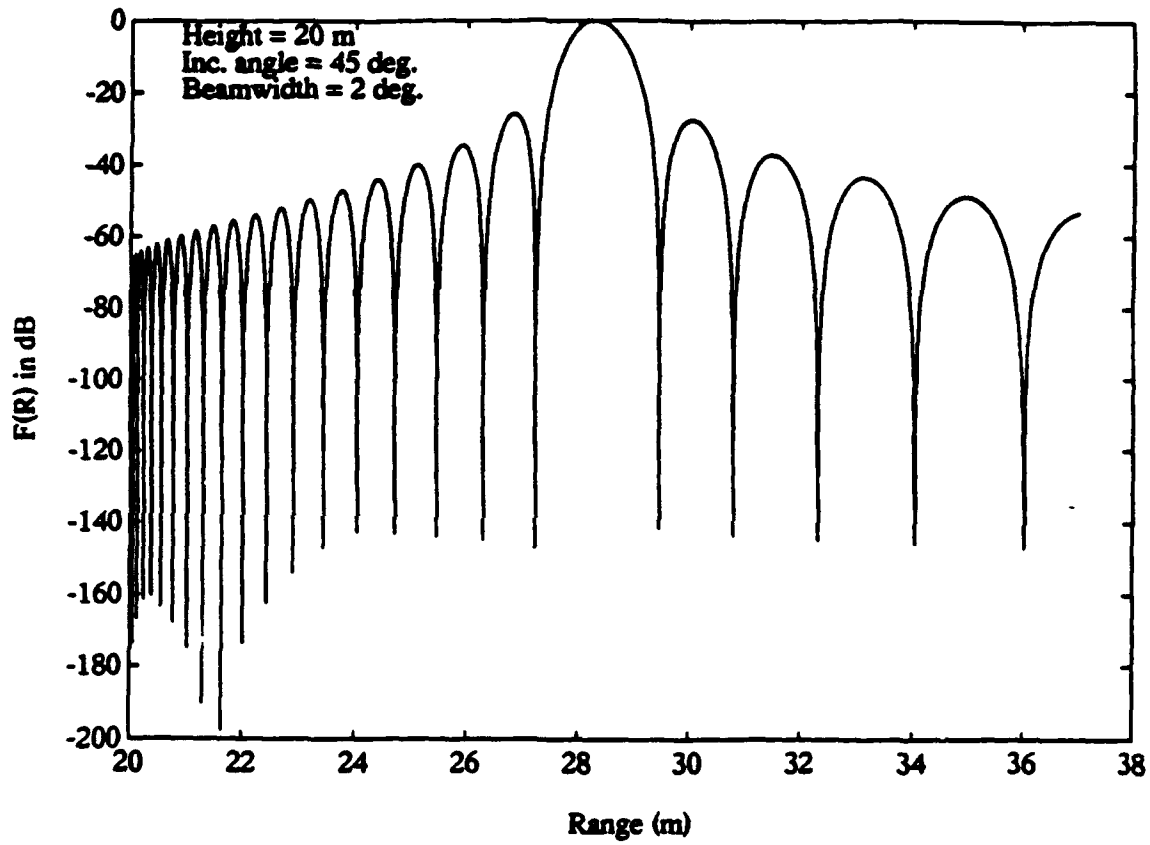


Figure 2.7 Example of the range spectrum $F(R)$.

target located at the center of the beam. The center of the beam is at the range

$$R_o = \frac{20 \text{ m}}{\cos(45^\circ)} = 28.28. \text{ Therefore, the range bias error is } \left(\frac{R_s - R_o}{R_o} \right) \times 100\% \approx 0.1\%.$$

This small error is not totally unexpected, since the VSG antenna is narrow band.

The error increases with increasing the antenna beamwidth, incidence angle, or the antenna height above the mean surface.

The bias error due the averaging effect of the antenna has little effect on the VSG measurements. First, as the example in the previous paragraphs demonstrates, the error is very small due to the VSG narrow antenna beamwidth. Second, we are interested in the variations around the mean range rather than the absolute ranges. By subtracting the mean range, the fixed bias error is effectively calibrated out.

2.8) Summary

FM-CW radars are more suitable for short-range operation than pulsed radar systems. In this chapter, we discussed some of the design methodologies for the FM-CW radar. We showed that for high signal-to-noise ratio the open-loop range tracker provides near optimal performance for measuring the target range.

Closed-loop range trackers are difficult to design. The major shortcoming of the closed-loop range tracker is the loss of track during deep signal fades. For an area-extensive target such as the ocean surface, the return signal can fade by as much as 30 dB. This means that the closed-loop circuits require constant operator attention. Additional circuitry for automatic resetting of the loop comes at the expense of additional cost and complexity.

Chapter 3

A VECTOR SLOPE GAUGE AND SCATTEROMETER FOR OCEAN MEASUREMENTS

3.1) Introduction

Increasing interest in the use of imaging radars to study ocean waves has led to much effort to understand the relation of microwave backscattering from the ocean surface to the ocean-wave parameters. Both real- and synthetic-aperture images of the ocean show wavelike patterns. Consequently, efforts have been underway for more than a decade to explain the modulation of the signal strength. Small-scale ripples, Bragg resonant with the microwave radiation, often dominate the backscattering from the rough ocean surface. Large-scale waves are imaged through modulation of both the amplitudes and (because of changing local angle of incidence) the wavelength of the resonant ripples. In an attempt to describe the modulation, a modulation transfer function (MTF) was introduced to relate the signal variations to the long-ocean-wave spectrum.

The modulation of ocean backscatter is due to tilting of the surface by large-scale waves (tilt modulation) and variations in ripple amplitude caused by the passing of the long waves. To classify the modulation properly, measurement of orthogonal components of the slope of the surface is necessary. This allows separation of effects due to surface tilting from hydrodynamic effects caused by

ripple-amplitude modulation. The VSG was developed to meet the need to measure the orthogonal components of the slope of the ocean surface in real time.

The VSG produced three switchable beams to illuminate three closely spaced surface footprints for the measurements of the surface slope. The VSG beams were formed by a single switched-feed parabolic dish antenna with 3-dB beamwidth of roughly 2° . The beams were switched at 30 Hz, and one measurement of range was obtained at each switching instant. Consequently, the VSG measured two components of the instantaneous slope every 0.1 seconds.

A mean-square detector also measured the instantaneous backscattered power for each beam. The presence of three independent measurements of the scattering for each height measurement provided an opportunity to average the time series to reduce the effects of fading noise and "sea spikes." Alternatively, one could append the time series to achieve more degrees of freedom in estimating the spectrum.

The VSG was housed in a lightweight, portable, weatherproof aluminum box with the antennas extending from one side. External power supplies, control switches, and the data-acquisition systems were also in weatherproof aluminum boxes. Shielded multiconductor cables connected the aluminum boxes to the main system. The data-acquisition system collected and stored samples of both radar outputs, range and scattered power, for later processing. The important specifications of the VSG are given in Table 1.

Table 1
VSG SPECIFICATIONS

TYPE	FM-CW
FREQUENCY	35 GHz
FM SWEEP WIDTH	300 MHz
TRANSMITTED POWER	27 dBm
FIRST INTERMEDIATE FREQUENCY	455 KHz
SECOND IF FREQUENCY	10.7 MHz
ANTENNA:	24" PARABOLIC SWITCHED FEED
POLARIZATION:	VV
BEAMWIDTHS:	2.8°, 1.8°, 2.7°
CALIBRATION:	DELAY LINE METAL SPHERE
INTERNAL	
EXTERNAL	
RECORDED OUTPUTS:	RANGE & SCATTERED POWER FOR EACH BEAM

3.2) Principle of operation

Figure 3.1 shows the intended mode of operation. The VSG beams are formed by a single switched-feed parabolic dish antenna. Frequency of operation is around 35 GHz, to allow closely spaced small-surface footprints with a moderate-size antenna. Each beam has a 3-dB width of roughly 2° . The beams are switched sequentially at a rate of 30 Hz. One measurement of the range, and consequently the ocean waveheight, is obtained for each beam position. Two components of the surface slope are computed from the three height measurements. Figure 1 also shows the footprint of a microwave scatterometer. In this mode of operation the VSG is a non-interfering, co-located instrument capable of measuring two orthogonal components of the instantaneous slope within the scatterometer footprint.

The centers of the three footprints of the antenna form the corners of a right triangle, fixed and oriented to a known reference. To illustrate the slope-measuring principle, assume that one leg of the triangle is along the radar look direction.

The component of slope in the radar look direction, which we arbitrary assign as being along the x-axis, is

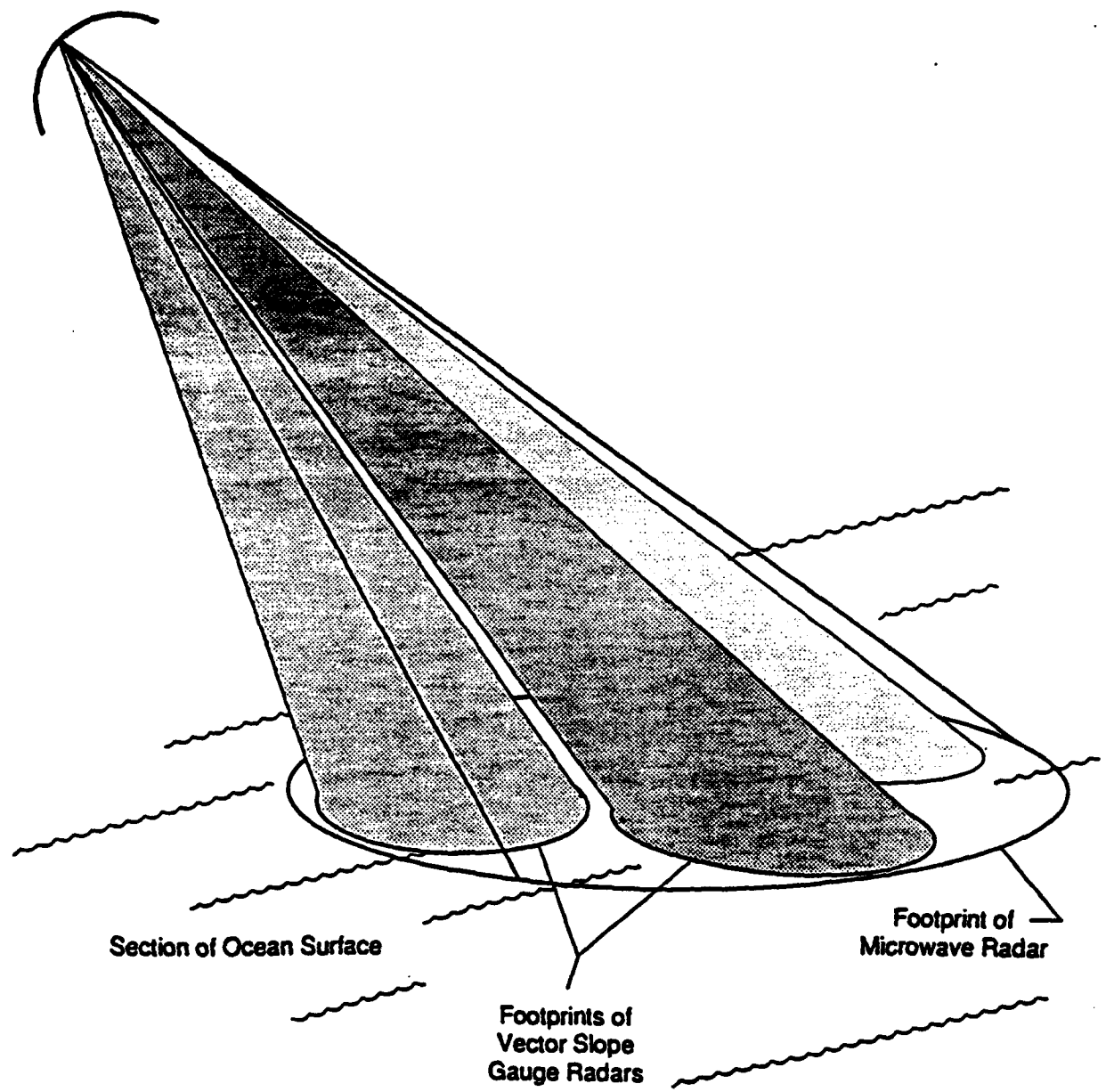


Figure 3.1 Basic principle of the Vector Slope Gauge (VSG).

$$\begin{aligned}
 s_x &= \frac{\partial W}{\partial X} = \frac{\Delta W}{\Delta X} \\
 &= \frac{R_1 \cos(\alpha) - R_2 \cos(\theta + \alpha)}{R_2 \sin(\theta + \alpha) - R_1 \sin(\alpha)}
 \end{aligned} \tag{1}$$

where R_1 and R_2 are the radar ranges. For beams pointed in the x direction, θ is the look angle for beam 1 and α is the increment between beam 1 and beam 2. Similarly, one gets the orthogonal component s_y , using R_1 and R_2 . The actual algorithm for calculating the slopes is more complicated and is discussed in detail in the next chapter. The complication is mainly due to the fact the antenna is 45° polarized. Therefore, the antenna had to be rotated around its axis 45° . An additional 12° of rotation was also introduced to ensure proper alignment of antenna and transmitting waveguides.

3.3) System block diagram

Figure 3.2 shows the overall block diagram. The C-band hyperabrupt varactor-tuned oscillator centered at 6 GHz provides the frequency-modulated signal. It sweeps linearly over a 500-MHz bandwidth with a triangular modulation waveform at the FM rate f_m . The coherent 29-GHz local oscillator supplies the reference signal for up and down conversion of the C-band modulated signal. The triangle-wave-modulated C-band signal is upconverted to 35 GHz by mixing it

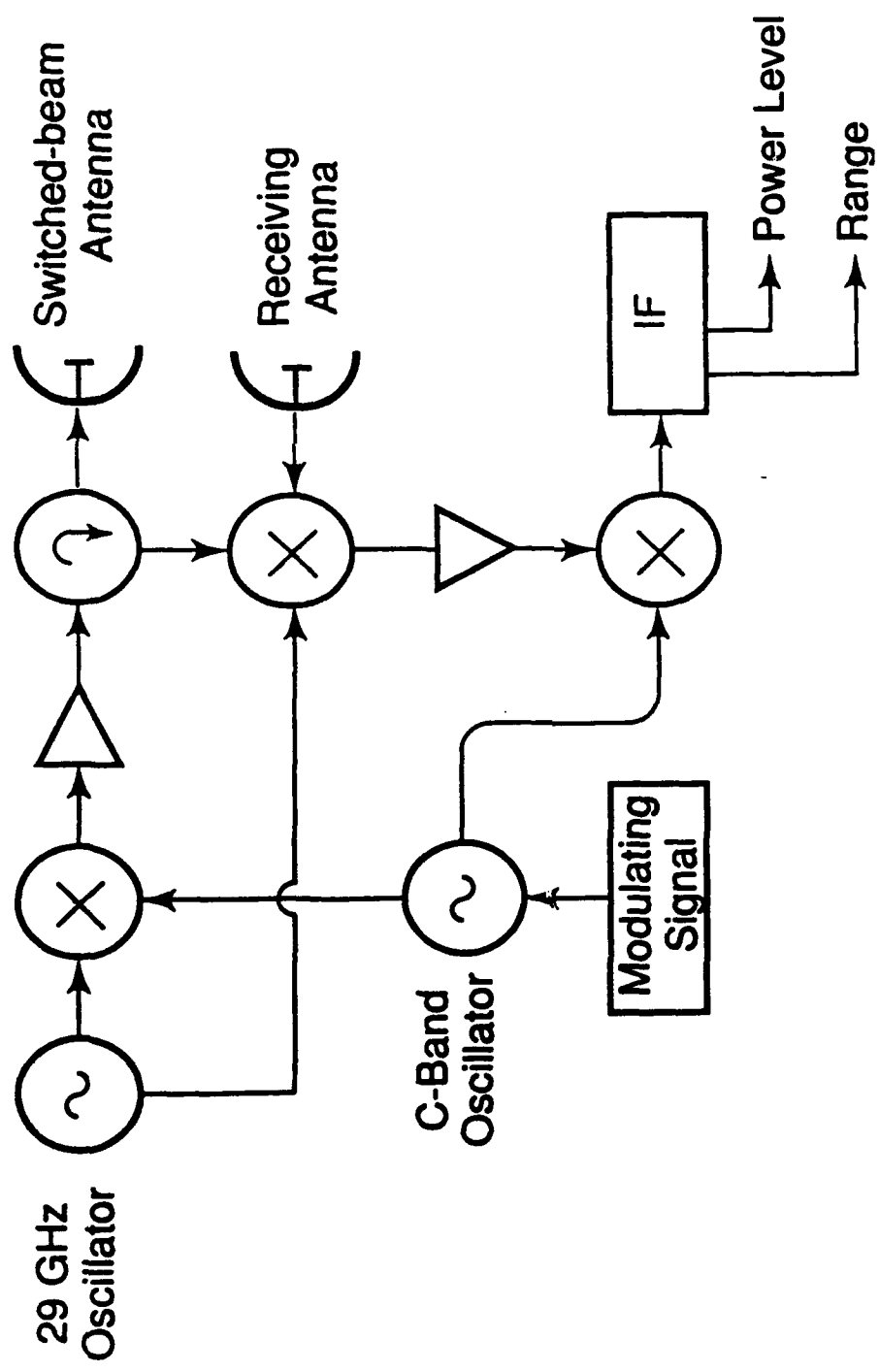


Figure 3.2 Overall block diagram of VSG.

with the 29-GHz local oscillator, amplified and then transmitted. The transmitter signal power at the antenna port is about 25 dBm. The received signal is downconverted, amplified, and then fed to a balanced quadrature mixer where it beats with a sample of the C-band oscillator. The resulting IF signal has a frequency offset proportional to the range to the target. The IF signal passes through a bandpass filter. It is amplified and upconverted to 10.7 MHz where it is demodulated by an FM detector. The output of the detector is a voltage that is proportional to the IF signal frequency and, hence, the range to the surface.

RF Section: Figure 3.3 shows the detailed block diagram of the RF section. Internal calibration results from passing a reference signal through the delay line. The delay-line power level is recorded at appropriate intervals and later is used to remove the variations in transmitted power and receiver gain. A sample of the transmitted signal provided by the 10-dB directional couplers produces the calibration signal. This signal is attenuated, and then it passes to the receiver via a directional coupler as shown in Figure 3.3. The signal is then downconverted to C band where the LO reference signal for the downconversion is a sample of the coherent local oscillator. The calibration signal is then amplified and passed through the delay line. The delay line is long enough so the signal appears at a range about equivalent to the range to the target. By using this scheme, calibration at appropriate intervals accounts for the drift of the system. During the measurement phase the delay line is short circuited, and the reflected calibration

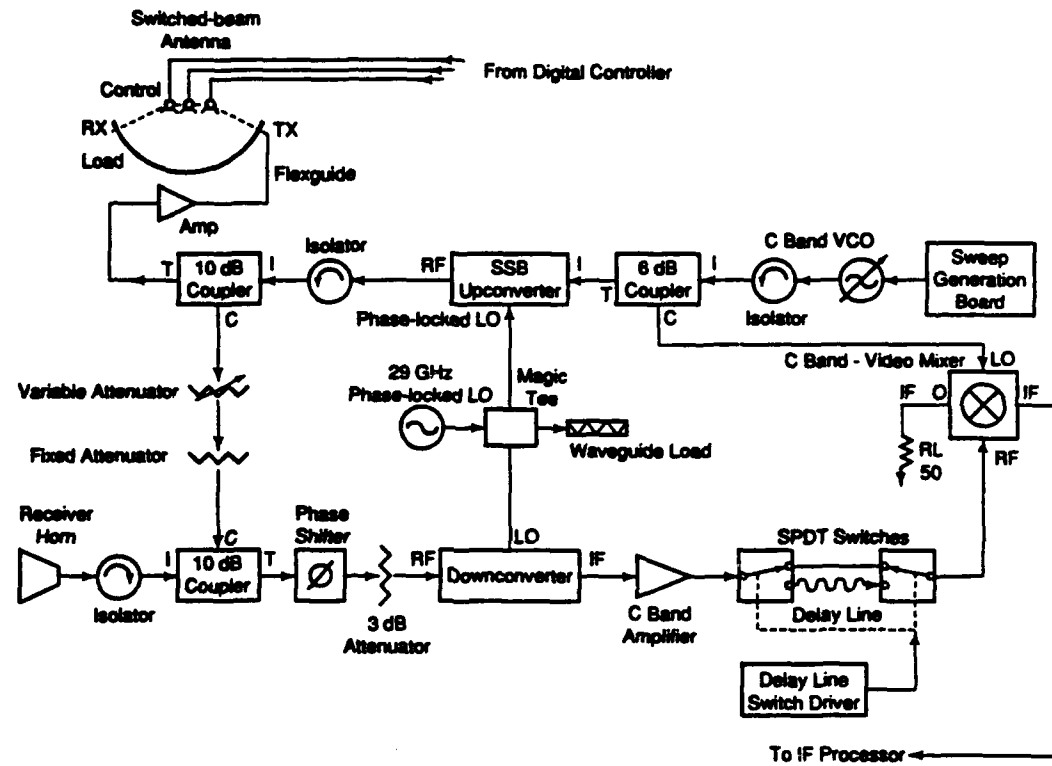


Figure 3.3 Block diagram of VSG, RF section.

signal appears as a strong target at very close range and, thus, at low IF. It is removed with a high-pass filter when making measurements, so it does not interfere with the target signal that occurs at much higher IF.

Transmitting antenna: The transmitting antenna is a 24-inch parabolic switched-feed antenna. Three discrete feed horns placed at the focal plane of the antenna dish produce the three beams. Figure 3.4 shows a close-up view of the three feeds. Each feed generates an independent beam. The position of each feed with respect to the focal point of the parabolic reflector determines the direction of the beams. The feeds are positioned such that the beams form the vertices of a right-angled triangle. The feed positioned at the focal point of the dish provides the on-axis beam along the focal axis of the parabolic dish. The off-axis beams are generated by two feeds that are displaced transversely from the focal point.

Switching between the beams is provided by three latching circulator switches. The switching circulators allow energy flow in either clockwise (CW) or counter-clockwise (CCW) direction. Figure 3.5 shows the block diagram of the antenna drive circuitry. The circuits to the right of figure are housed in a small box placed directly behind the antenna feeds. A 15-pin connector provides the interface for powering and controlling the switches. Tables 2 and 3 give a summary of the antenna characteristic and the beam-switching logic.

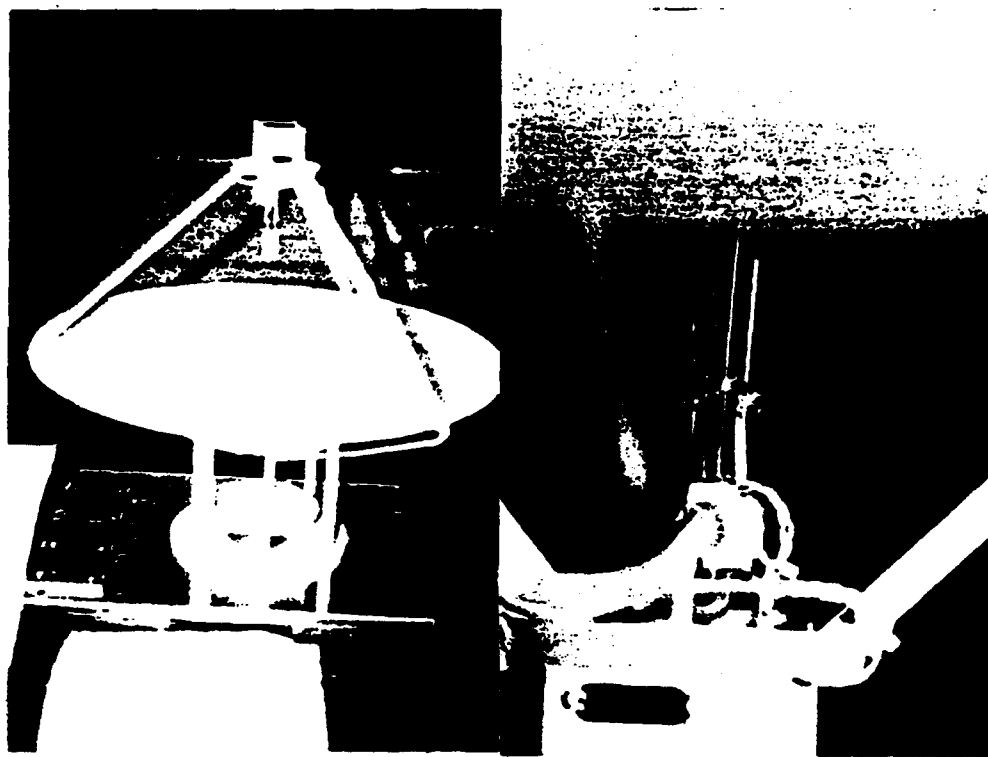


Figure 3.4 The VSG transmitting antenna

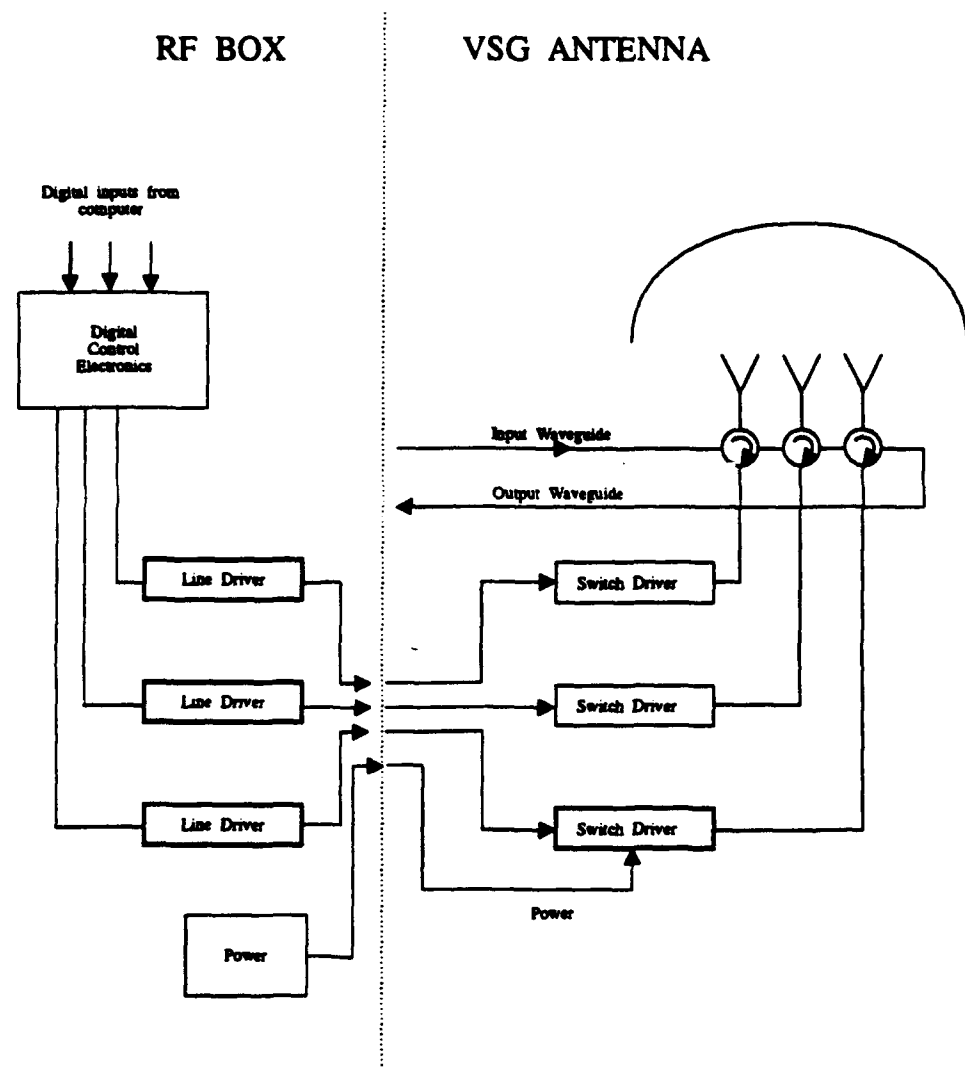


Figure 3.5 VSG antenna block diagram.

Table 2. VSG Antenna Characteristics

Sidelobes	< -13 dB		
Insertion Loss	< 0.2 dB (34.5 Ghz to 35.5 GHz)		
Switching rate	< 1 MHz		
Beam-to-Beam Variations	< 1 dB		
	Beamwidth (3 dB)	Offset (Deg)	Gain (dB)
Beam 1	1.88	3.14	29.79
Beam 2	2.81	0.06	29.31
Beam 3	2.77	-3.19	29.0

Table 3. Beam-switching logic

	RF Switch 1	RF Switch 2	RF Switch 3
Beam 1	CW	CW	CCW
Beam 2	CCW	CCW	CCW
Beam 3	CCW	CW	CW

The data-acquisition computer switches the beams sequentially at a rate of 30 Hz. It is also responsible for sampling and recording the various radar outputs. The sampling of the radar outputs occurs about 20 ms after the beam switching. This allows sufficient time for the transients due to beam switching to die out.

The receiving antenna is a 3-inch collimating horn lens. The problem of reflections from the transmit port of the antenna is much less when using a separate receiving antenna.

IF Section: Figure 3.6 shows the block diagram of the IF section. The nominal input frequency is around 455 kHz. The isolation transformer in the first stage prevents undesirable ground loops. The IF signal then passes through the bandpass filter, is amplified and upconverted to 10.7 MHz. The automatic-gain-control (AGC) circuit, ahead of the upconvertor, keeps the input level within the dynamic range of the upconvertor. The 10.7-MHz IF signal passes through a narrow-band ceramic bandpass filter, and it is demodulated by an FM detector. The output of the detector is a voltage that is proportional to the IF frequency and, hence, the range to the target.

The FM detector uses the RCA-CA3181 FM-demodulator chip that provides excellent performance at low cost. This integrated circuit provides IF amplification, limiting, and balanced FM detection. A balanced tuned quadrature detector, with distortion less than 0.1% at full modulation, performs the FM demodulation. The detector has an input-limiting sensitivity of 10 μ volts and an

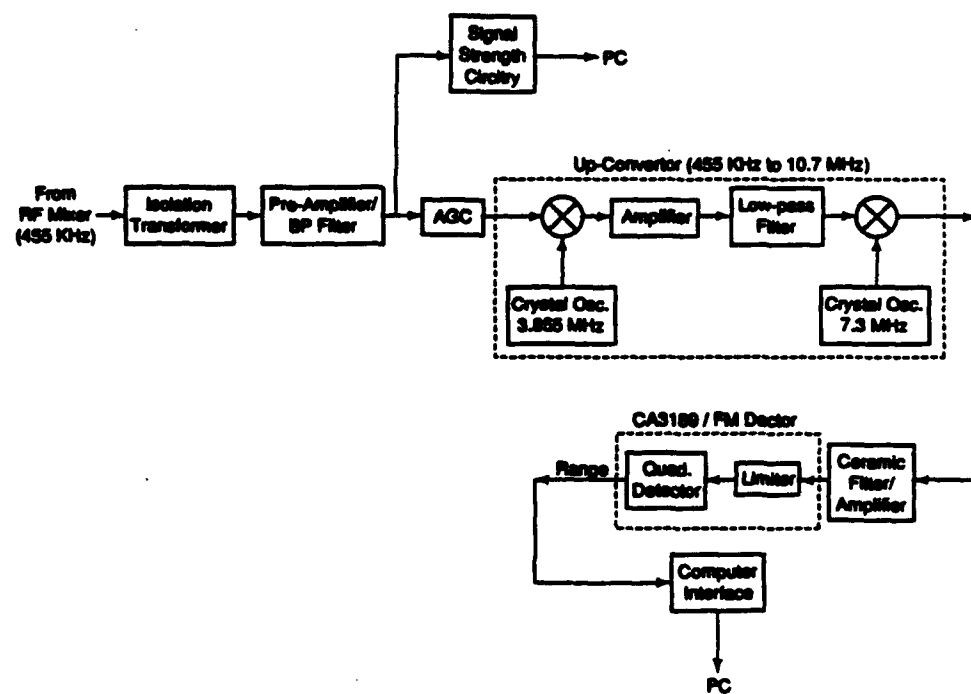


Figure 3.6 Block diagram of VSG, IF section.

AM rejection of 60 dB. The chip has an excellent signal-to-noise ratio. The (S+N)/N ratio levels off at over 70 dB with more than 300- μ volt inputs to the chip. Since the RCA-CA3181 has very high gain, one should carefully design the ground-plane layout to prevent coupling of the output terminal to the input grounds. Figure 3.7 shows the response of the FM detector block.

The amplitude of the IF signal is proportional to the received voltage from the target. For cross-section measurement, a portion of the IF signal goes to the signal-strength circuitry as shown in Figure 3. 6. Since the return power from targets such as the ocean surface can easily vary over several orders of magnitude, three separate detectors with overlapping responses provide the required dynamic range. Each detector produces an output proportional to the RMS of its input signal. Figure 3.8 shows the characteristics of the RMS-to-DC detectors.

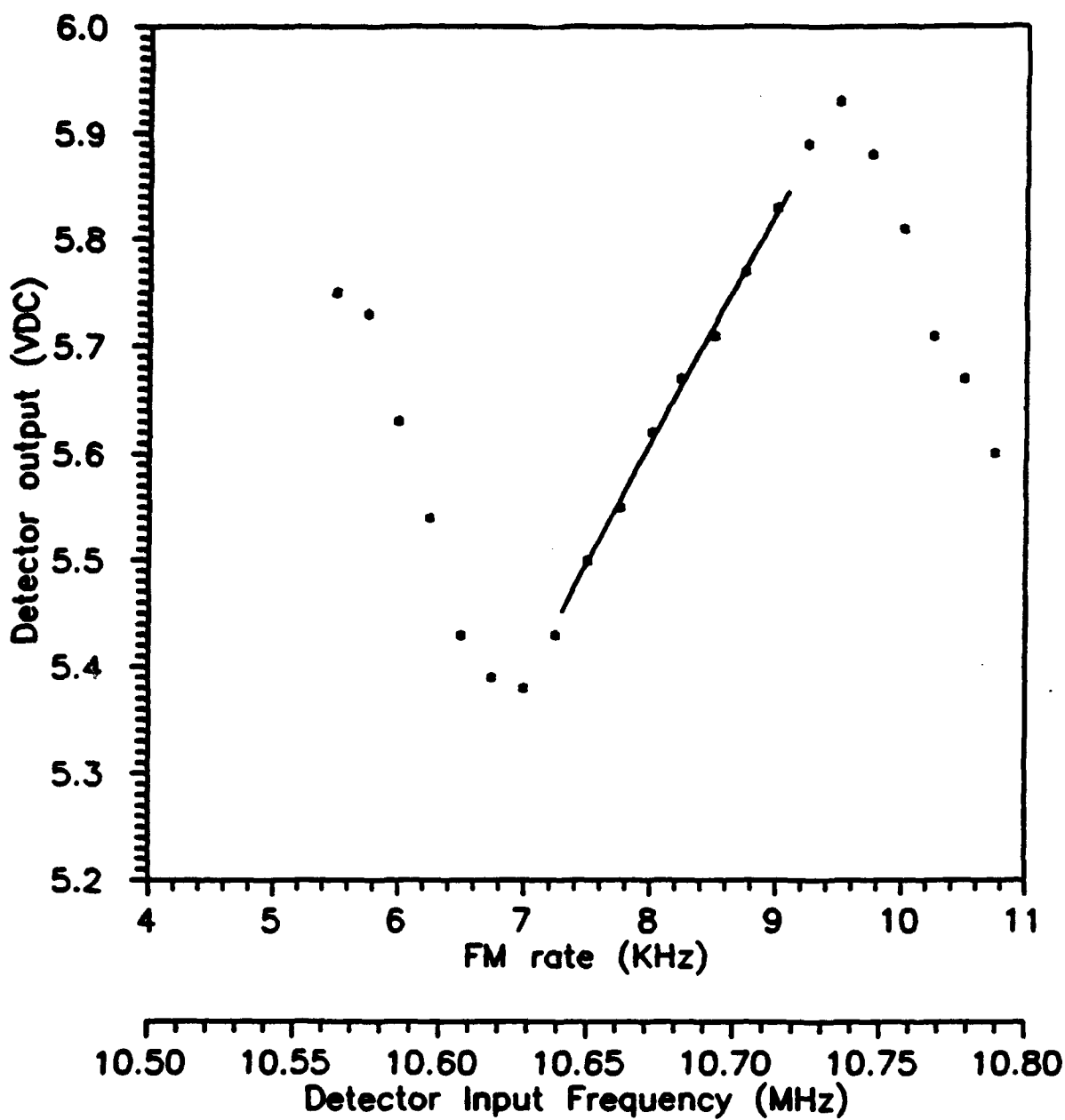


Figure 3.7 Frequency response of the FM detector.

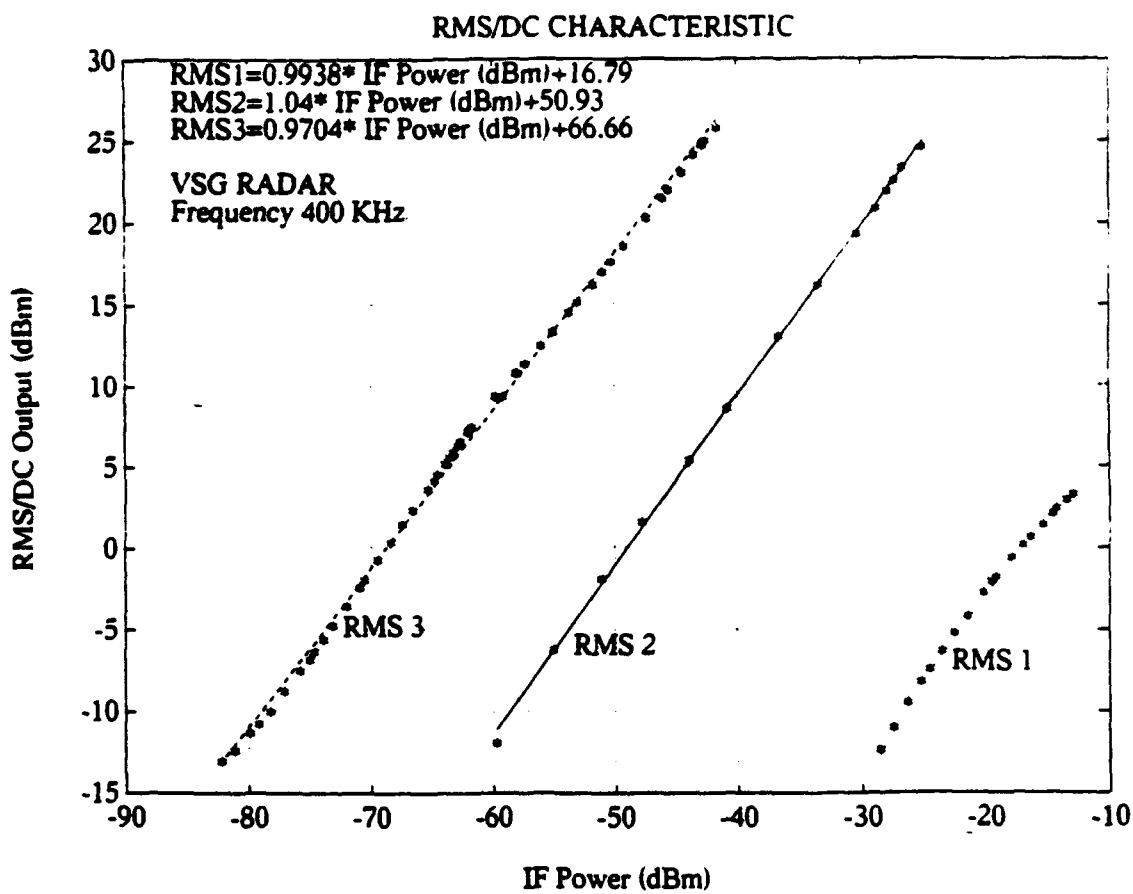


Figure 3.8 Channel characteristics of the IF level detectors.

3.4) Summary

This chapter describes the vector slope gauge/scatterometer and its potential as a unique oceanographic instrument. The system uses a switched-beam antenna to measure two orthogonal components of the surface slope. To obtain slopes, many investigators have depended on wave gauges located some distance from the radar footprint or on integration of the velocity, obtained from Doppler measurements. Direct measurements of orthogonal components of the slopes of the surface permits the removal of effects due to surface tilting (tilt modulation) from the radar cross section, which was not previously possible.

Chapter 4

SAXON-FPN EXPERIMENT AND DATA ANALYSIS

4.1) Introduction

In this chapter we present some of the measurements obtained by the vector slope gauge (VSG) during the SAXON-FPN experiment in November, 1990. We discuss the potential of the vector slope gauge for providing some of the important measurements needed to properly characterize the ocean surface profile. The VSG can provide simultaneous measurements of the surface slopes and the microwave scattering from the surface, allowing separation of tilt and hydrodynamic modulation.

In principle, the VSG can measure the same surface qualities as a free-floating pitch-and-roll buoy. A buoy typically measures the slope (tilt) in two orthogonal directions (pitch and roll) and the vertical acceleration. The acceleration is integrated twice to obtain the surface height. Longuet-Higgins et al. (1961) describe a procedure for extracting the directional spectrum of the ocean waves from measurements of surface height and orthogonal components of slope. With this technique, one can compute the first five coefficients of the Fourier series expansion of the directional spectrum from the height and slope measurements. Other methods of estimating the directional spectrum from a pitch-and-roll buoy have been developed in recent years. Examples include the

maximum likelihood method (Oltman-Shay, et al. 1984) and the eigenvector method (Madsen, et al., 1987). These techniques depend on the linear wave theory to calculate the directional spectrum. Since the VSG measures the same quantities as a pitch-and-roll buoy, its output can be processed in the same manner to obtain wave direction. For sea-based tower measurements, the VSG has the advantage of measuring the components of surface slope within a scatterometer footprint. This makes possible the direct correlation of the surface slopes with the scatterometer output.

As a scatterometer, the VSG offers some unique features. Each antenna beam provides an independent sample of the microwave scattering. This provides the opportunity to average the time series to reduce the effects of fading noise and "sea spikes" or, alternatively, to append the time series to achieve more degrees of freedom in the spectral estimates.

The VSG was operated during the SAXON-FPN experiment. Next, we briefly describe the experiment and the type of data collected.

4.2) The SAXON-FPN experiment

The Synthetic-Aperture Radar and X-band ocean nonlinearities (SAXON) experiment was conducted on the German Forschungsplattform Nordsee (FPN) during November, 1990. The platform was located in 30 meters of water in the German Bight. Figure 4. 1 shows the tower and the range of instruments that operated during the experiment. In addition, six aircraft and one research ship participated in the experiment. The aircraft carried a wide variety of imaging radars, scatterometers, microwave and infrared radiometers, and other types of oceanographic instruments.

The University of Kansas operated two instruments during the SAXON-FPN experiment: the radar vector slope gauge (VSG), and the C- and X-band scatterometers. The VSG measured three ranges to the surface, from which two orthogonal components of the surface slopes were determined. The radar also measured simultaneously the scattered microwave power from the three different spots. The system was described in detail in the previous chapter. The VSG worked well throughout most of the experiment. However, On November 27, after a power failure on the tower, the low-noise C-band amplifier failed. It was replaced with a lower-gain amplifier that made low-wind-speed data questionable after that date.

The main emphasis of the VSG measurements was on long data sets (55 minutes) at a few fixed azimuth angles(generally upwind or crosswind) and

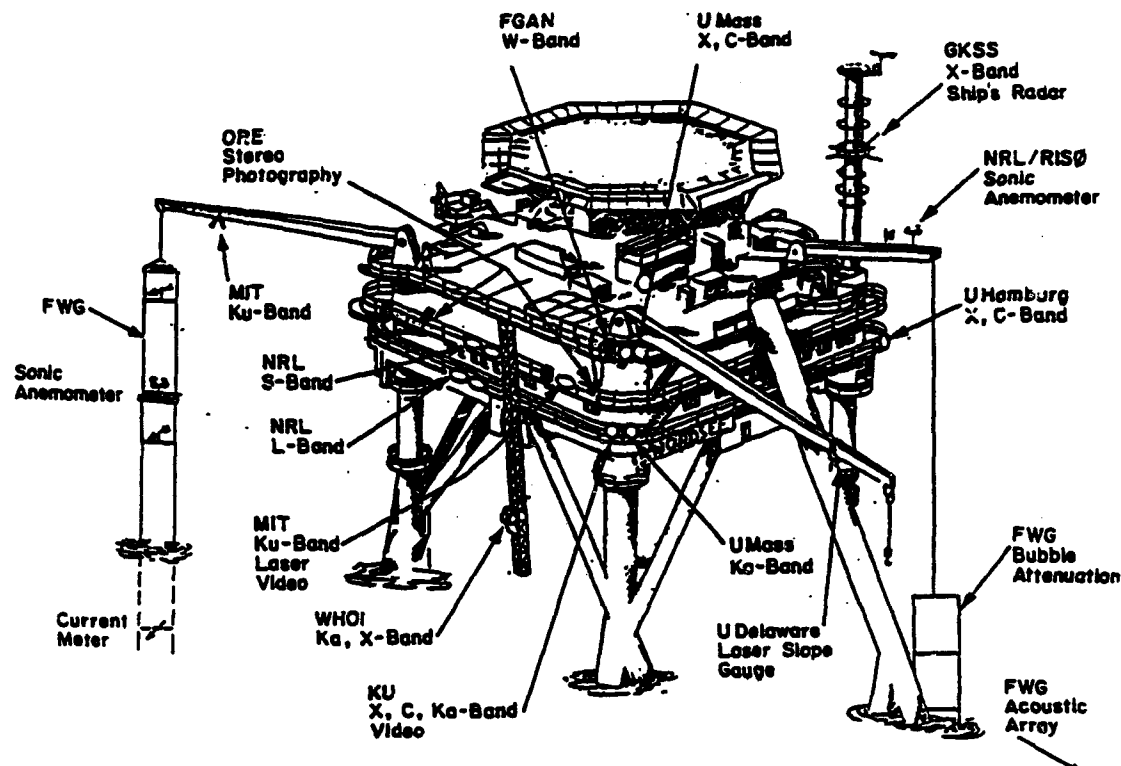


Figure 4.1. The German Forschungsplattform Nordsee during the SAXON-FPN experiment. (reproduced from Plant and Alpers, 1991).

incidence angles of 45° to 55° . The wind speed during the measurements ranged from 2 to 18 m/s. A summary of the environmental conditions during VSG measurements is given by Youssefi (1992).

The C- and X-band scatterometers were to measure the scattered power within the combined footprint of the VSG. The X-band system did not produce any good data. The range tracker in C-band system also did not work properly. After considerable effort, the closed-loop tracker was disabled and the system was modified to measure only the scattering. The compromise was to use the VSG to provide the surface height data.

The VSG was mounted at the northwest corner of the tower (see Figure 4.1). Figure 4.2 shows the system during operation. The system could be rotated manually in azimuth over a 50° range. The elevation was controlled with an electric actuator. The receiving horns were added in the field to improve the sensitivity of the C- and X-band radars. The system on the left, wrapped in a nylon cover, was the Ka-band system operated by The University of Massachusetts.

The data acquisition system consisted of two remote computers and a host computer (Khan, et al. 1992). This system replaced the system used in the SAXON-CLT experiment in fall 1988. The SAXON-CLT system transmitted analog signals over 30-m-long single-ended wires. This cable was bulky and difficult to deploy. In addition, substantial electrical noise was picked up on the

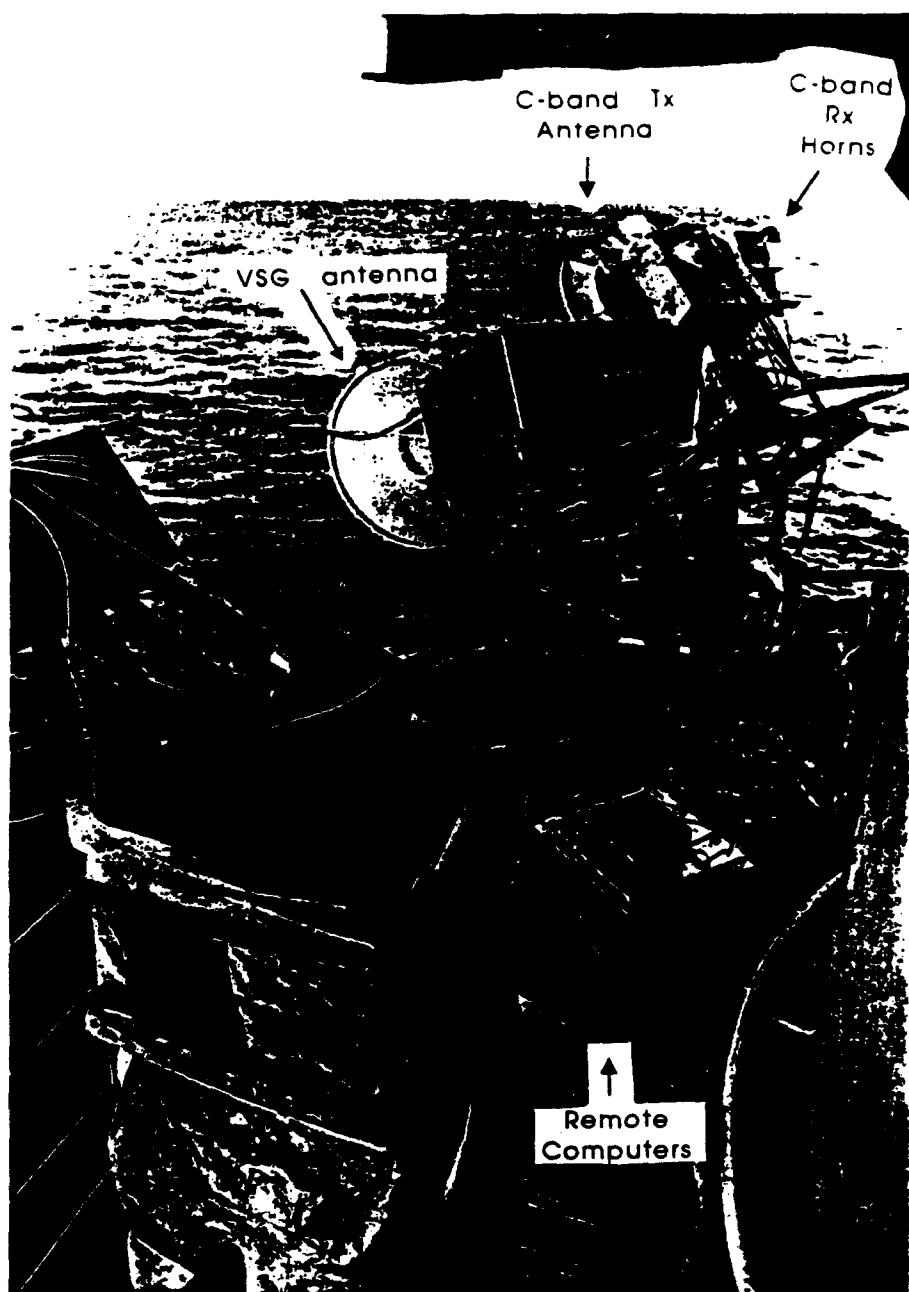


Figure 4.2. The VSG during operation

long analog signal lines. The new data-acquisition system, employed at SAXON-FPN, consisted of two environmentally sealed PC-compatible-based computers mounted next to the radars. The *analog outputs of the radar* were digitized by the remote computers and traveled over a asynchronous serial communication link to the 386 host computer system. The host computer was located in a laboratory 30 m from the remote site. By digitizing the low-level analog signals directly at their source, the danger of EMI was greatly reduced. This scheme also decreased the number of wires between the remote side and the operator side. The host computer stored the digital data on Bernoulli cartridges for further processing. The host computer also controlled the switching of the VSG antenna beams.

4.3) Slope measuring principle and accuracy

The three footprints of the antenna form the corners of a right triangle, fixed and oriented to a known reference. Figure 4.3 shows the antenna footprints on a flat surface. The radar measures the surface height at the center of each footprint.

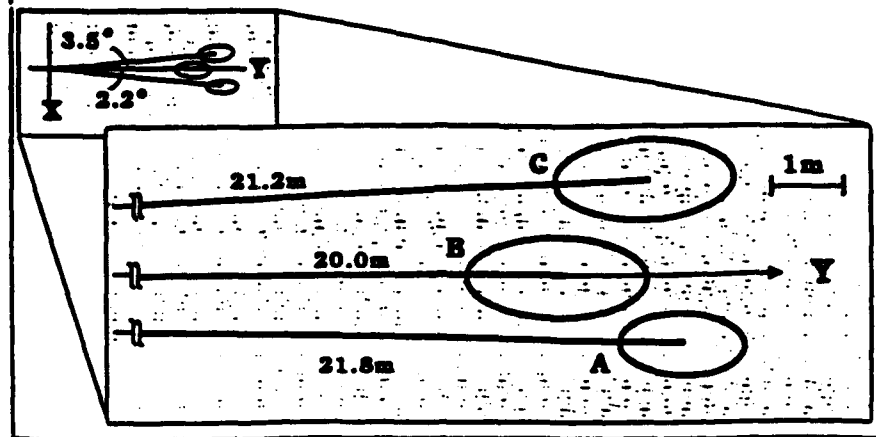
The VSG samples the complicated surface of the ocean at discrete points in both space and time. It measures the range, and hence the waveheight, at three different positions on the surface. The sampling frequency for each beam is 10 Hz. This means that surface waves with frequencies up to 5 Hz are detected by the radar. The distance between the antenna footprints is the sampling interval in the spatial domain. Referring to Figure 4.3, this distance is of the order of $L=2$ m. This implies that $L/2=1$ m is the wavelength of the shortest wave that the radar can detect. Ocean waves of this wavelength have a temporal frequency of about 1.2Hz.

To avoid aliasing, the sampling frequency must be greater than twice the highest frequency present. This principle applies to sampling in both the space and time domains. For the ocean waves, the temporal and spatial frequencies are related by the dispersion relation. We avoid aliasing in the spatial domain by filtering high frequency waves in the temporal domain. With 10-point decimation, the effective temporal sampling rate is 1 Hz, so that waves with frequencies greater than 0.5 Hz are removed from the data records. Ocean waves of this frequency are

BEAM GEOMETRY FOR VSG RADAR
PLANE OF OCEAN

BEAM CHARACTERISTICS

- A. Range: 29.6m, Beamwidth: 1.8° , Footprint Area 1.0m^2
- B. Range: 28.3m, Beamwidth: 2.8° , Footprint Area 2.1m^2
- C. Range: 29.2m, Beamwidth: 2.8° , Footprint Area 2.3m^2



BEAM GEOMETRY FOR VSG RADAR
PERSPECTIVE VIEW

BEAM CHARACTERISTICS

- A. Range: 29.6m, Inc Ang: 48°
- B. Range: 28.3m, Inc Ang: 45°
- C. Range: 29.2m, Inc Ang: 47°

Antenna Height: 22m

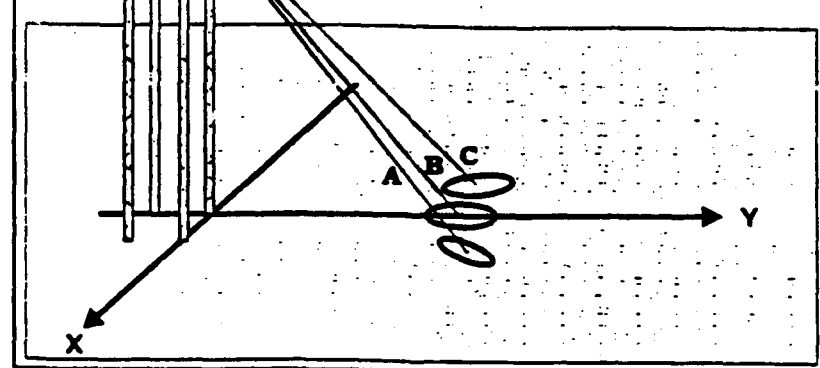


Figure 4.3. VSG beam geometry.

about 6 meters long. Since the spacial sampling interval is about 2 meters, the sampling theorem is satisfied in both the space and time domains.

The estimate of slope in an arbitrary direction is

$$\hat{s}(t, x) = \frac{\Delta w(t, x)}{\Delta X} \quad (1)$$

where $\hat{s}(t, x)$ is the first-order approximation of the true slope $s(t, x)$. The factor ΔX is the distance between the antenna beams and we assume it is a constant. For a single component of the wave traveling along the x -axis with frequency F and wave number K , the surface height is

$$w(t, x) = A e^{j(2\pi f t + Kx)} \quad (2)$$

The true slope is spatial derivative of the above equation:

$$s(t, x) = j A K e^{j(2\pi f t + Kx)} \quad (3)$$

The VSG estimate of slope is:

$$\hat{s}(t, x_o) = \frac{w(t, x_o - \Delta X/2) - w(t, x_o + \Delta X/2)}{\Delta X} \quad (4)$$

Substituting (2) in the above equation and simplifying, we obtain

$$\hat{s}(t, x_o) = j A K e^{j(2\pi f t + Kx_o)} \frac{\sin(K \Delta X/2)}{(K \Delta X/2)} \quad (5)$$

or

$$\hat{s}(t, x) = s(t, x) \left[\frac{\sin(K \Delta X/2)}{(K \Delta X/2)} \right] \quad (6)$$

The term in the bracket is the error. It depends on the wave number K and the

distance between the beams ΔX . The errors are small up to a long-wave frequency of roughly 0.4 Hz. Note that (4) is a central difference; that is, our computed slopes are samples of the surface slope at points midway between the antenna footprints. The waveheight measurements, on the other hand, are referred to a point at the center of the triangle formed by the three footprints of the antenna. The phase error, due to measuring the slope and waveheight at different points on the surface, is small. The maximum error is less than 5° at 0.15 Hz, and is about 15° at 0.5 Hz.

4.4) Evaluation of orthogonal components of slope surface

Figure 4.4 shows the antenna geometry. The antenna is at the origin of xyz coordinate and is located at a height of H above the mean surface. The three lines originating from the antenna indicate the direction that the beams are pointing. In the figure, α_{12} is the angle between beams 1 and 2, and α_{23} is angle between beams 2 and 3. Beam 2 is the on-axis beam; that is, it is perpendicular to the plane of the antenna and is generated from the feed placed at focal point of the parabolic dish.

The beams strike the water surface at points q_1 , q_2 , and q_3 , which uniquely define the plane **Q**. The distances between these points and the origin (d_1 , d_2 , and d_3) are measured by the VSG. Our aim is to find the equation of the plane **Q** in terms of these measured ranges and the antenna calibration angles α_{12} , α_{23} , ϕ , and β . The angle β is the angle between the planes formed by beams 1 and 2, and

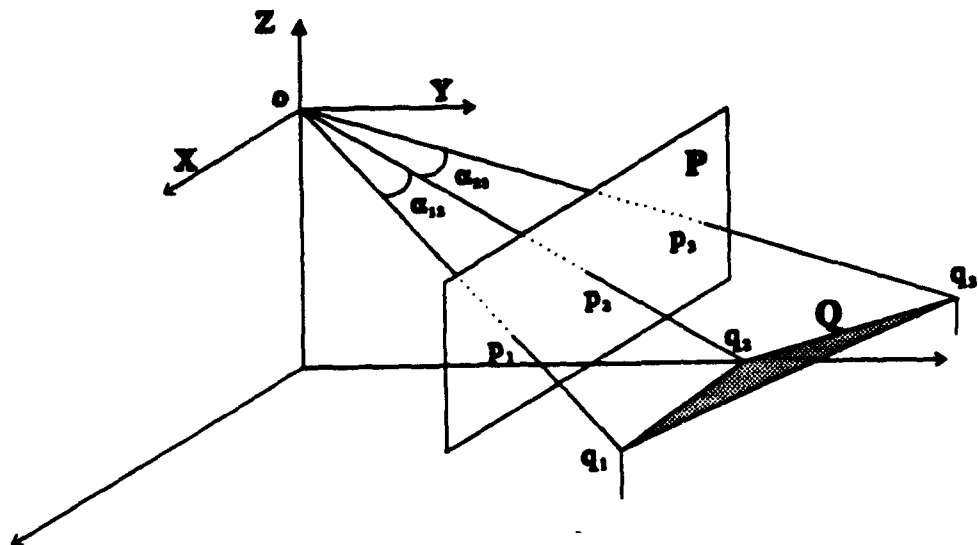


Figure 4.4 The VSG antenna configuration and its slope measuring principle.

beams 2 and 3. The angle ϕ refers to the amount that the antenna was rotated around its axis during installation. This angle was measured in the field, and was around 12° .

Let plane **Q** be defined as

$$\text{plane } \mathbf{Q} : Lx + My + Nz + P = 0 \quad (7)$$

The orthogonal components of slope s_x and s_y are the derivatives of the surface elevation in the x and y directions. Therefore, from (7) we have

$$\begin{aligned} s_x &= \frac{L}{N} \\ s_y &= \frac{M}{N} \end{aligned} \quad (8)$$

The unit vector normal to the plane **Q** is given by

$$\hat{n} = \frac{\frac{L}{N}\hat{x} + \frac{M}{N}\hat{y} + \hat{z}}{\sqrt{1 + \left(\frac{L}{N}\right)^2 + \left(\frac{M}{N}\right)^2}} \quad (9)$$

In Figure 4.4 we define **P** as a plane parallel to **yz** plane at some arbitrary distance. The antenna beams penetrate the plane **P** at points $p_1(p_{1x}, p_{1y}, p_{1z})$, $p_2(p_{2x}, p_{2y}, p_{2z})$, and $p_3(p_{3x}, p_{3y}, p_{3z})$. The coordinates of these points, in terms of the antenna parameters, are given by

$$\begin{aligned}
 p_{1x} &= -d \tan(\alpha_{12}) [\sin(\beta/2) \cos(\phi) - \\
 &\quad \cos(\beta/2) \sin(\phi)] \\
 p_{1y} &= d \cos(\theta) + d \tan(\alpha_{12}) [\sin(\beta/2) \sin(\phi) + \\
 &\quad \cos(\beta/2) \cos(\phi)] \sin(\theta)
 \end{aligned} \tag{10}$$

$$\begin{aligned}
 p_{1z} &= d \tan(\alpha_{12}) [\sin(\beta/2) \sin(\phi) + \\
 &\quad \cos(\beta/2) \cos(\phi)] \cos(\theta) - d \sin(\theta) \\
 p_{2x} &= 0 \\
 p_{2y} &= d \cos(\theta) \\
 p_{2z} &= -d \sin(\theta)
 \end{aligned} \tag{11}$$

$$\begin{aligned}
 p_{3x} &= -d \tan(\alpha_{23}) [\sin(\beta/2) \cos(\phi) + \cos(\beta/2) \sin(\phi)] \\
 p_{3y} &= d \cos(\theta) + d \tan(\alpha_{23}) [-\sin(\beta/2) \sin(\phi) + \cos(\beta/2) \cos(\phi)] \sin(\theta) \\
 p_{3z} &= d \tan(\alpha_{23}) [-\sin(\beta/2) \sin(\phi) + \cos(\beta/2) \cos(\phi)] \cos(\theta) - d \sin(\theta)
 \end{aligned} \tag{12}$$

In the above equations d is an arbitrary distance from the origin to the point p_2 .

The coordinates of the three points on the surface $q_1(q_{1x}, q_{1y}, q_{1z})$, $q_2(q_{2x}, q_{2y}, q_{2z})$, and $q_3(q_{3x}, q_{3y}, q_{3z})$, are given by

$$q_{il} = \frac{p_{il} d_i}{\sqrt{p_{il}^2 + p_{il}^2 + p_{il}^2}} \quad i = 1, 2, 3 \text{ and } l = \{x, y, z\} \tag{13}$$

where d_1 , d_2 , and d_3 are the three ranges measured by the radar. Substituting (10) and (11), into the above equation, we find the coordinates where the beams strike the surface. We then find the equation of the plane \mathbf{Q} and the two orthogonal components of slope from (7) and (8). Although the procedure is

simple, the equations are rather long . For the sake of simplicity, we present only the final results. After considerable simplification, the orthogonal components of slope are

$$S_x = \frac{L_1 d_1 d_2 + L_2 d_2 d_3 + L_3 d_1 d_3}{N_1 d_1 d_2 + N_2 d_2 d_3 + N_3 d_1 d_3} \quad (14)$$

$$S_y = \frac{M_1 d_1 d_2 + M_2 d_2 d_3 + M_3 d_1 d_3}{N_1 d_1 d_2 + N_2 d_2 d_3 + N_3 d_1 d_3} \quad (15)$$

where

$$\begin{aligned} L_1 &= \sin\alpha_{12} \sin\phi \sin\beta - \cos\phi \sin\alpha_{12} \cos\beta \\ L_2 &= \sin\alpha_{23} \cos\phi \\ L_3 &= \cos\alpha_{12} \cos\phi \sin\alpha_{12} \cos\beta - \cos\alpha_{12} \sin\alpha_{23} \cos\phi \\ &\quad - \sin\alpha_{12} \cos\alpha_{23} \sin\phi \sin\beta \end{aligned} \quad (16)$$

$$\begin{aligned} M_1 &= \sin\alpha_{12} \cos\phi \cos\theta \sin\beta + \sin\phi \sin\alpha_{12} \cos\beta \cos\theta \\ M_2 &= - \sin\alpha_{23} \sin\phi \cos\theta \\ M_3 &= \cos\alpha_{12} \sin\phi \sin\alpha_{23} \cos\theta - \sin\alpha_{12} \cos\alpha_{23} \cos\phi \cos\theta \sin\beta \\ &\quad - \sin\alpha_{12} \sin\alpha_{23} \sin\theta \sin\beta - \cos\theta \cos\alpha_{23} \sin\alpha_{12} \sin\phi \cos\beta \end{aligned} \quad (17)$$

$$\begin{aligned} N_1 &= - \sin\alpha_{12} \cos\phi \sin\theta \sin\beta - \sin\phi \sin\alpha_{12} \cos\beta \sin\theta \\ N_2 &= \sin\alpha_{23} \sin\phi \sin\theta \\ N_3 &= \sin\alpha_{12} \sin\phi \cos\alpha_{23} \sin\theta \sin\beta - \cos\alpha_{12} \sin\alpha_{23} \sin\phi \sin\theta \\ &\quad + \sin\alpha_{12} \sin\alpha_{23} \cos\theta \sin\beta + \sin\theta \cos\alpha_{23} \sin\alpha_{12} \sin\phi \cos\beta \end{aligned} \quad (18)$$

4.5) Estimating the dominant wave direction

Each vector slope is defined uniquely by its orthogonal components s_x and s_y , at each sampling instant. The data can be plotted many ways. A useful form is the scatter plot of the slope vectors. We represent each vector by an arrow emitting from the origin. Figure 4.5 shows a sample plot. The tip of the arrows trace an elliptical pattern with the longest dimension along the wave direction. The solid line through the ellipse is a best-fit line that shows the direction of the wave travel. It is clear from the figure that the front face of the wave has sharper slopes than the back face. Note that the elliptical pattern is not centered at the origin, rather it is displaced in the direction of wave travel. The displacement is a measure of the skewedness of the waves. The fact that a minimum, not a null, appears orthogonal to the principal wave direction is contrary to some analytical models of the surface.

The asymmetry of the surface waves also reveals itself in the frequency domain. Figure 4.6 compares normalized waveheight and slope-magnitude spectra. The spectrum of the received microwave signal is also shown. The peak of the waveheight spectrum (dominant wave) is at 0.117 Hz. The peak in the slope spectrum corresponding to the dominant wave frequency is slightly shifted to the right and occurs at a frequency of 0.12 Hz. The radar-signal spectrum also shows a peak near the dominant long-wave frequency of 0.12 Hz. For almost every peak in the radar-signal spectrum there is a corresponding peak in the slope spectrum.

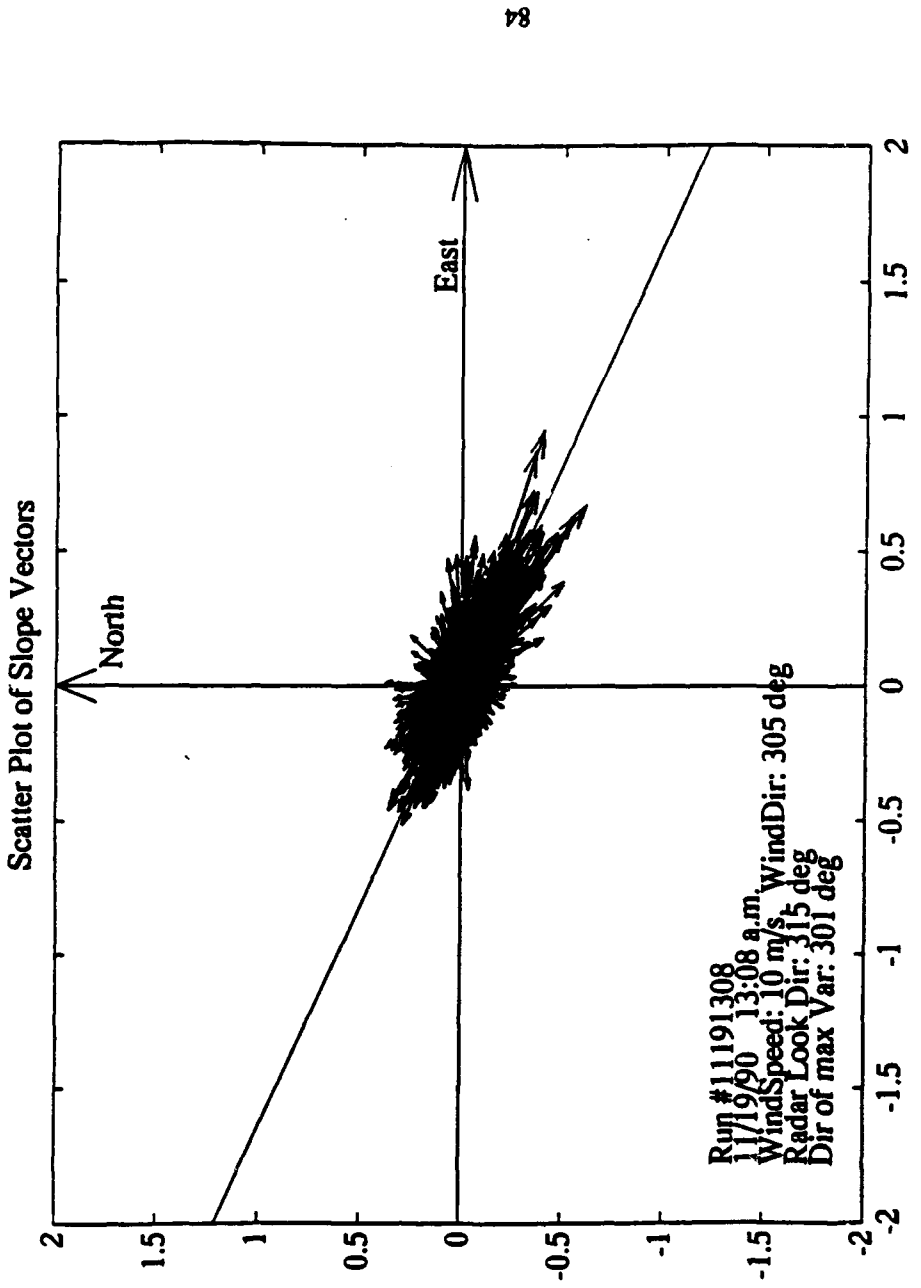


Figure 4.5 Sample scatter plot of vector slopes. Wind speed is at 10 m/s from 305° (360° refers to North, and 90° to East).

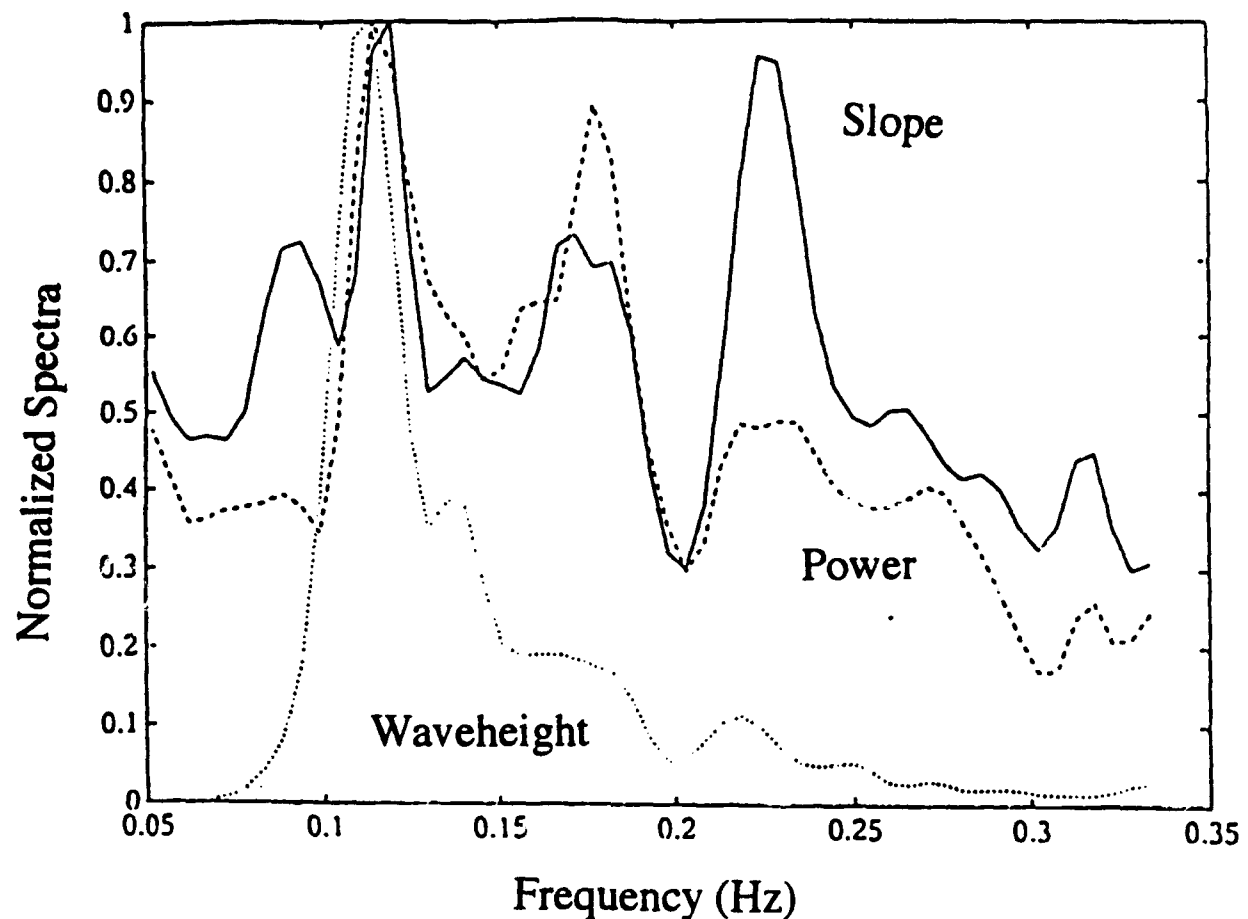


Figure 4.6 Sample upwind/upwave run comparing the long-wave height, slope in the radar look direction and the radar-signal spectra. Wind speed is 10 m/s, and radar incidence angle is 45°.

A close study of the slope spectrum reveals some interesting results. Four distinct peaks appear in the slope spectrum (ignoring the peak at DC). The most striking feature of the frequencies identified in the spectrum is that two of them can be expressed as second harmonics of the other frequencies. The choice of the two "fundamental" frequencies is somewhat arbitrary: one is selected because it is the dominant long-wave frequency, and the second is picked because it is closest to the first frequency.

The last column in Table 1 shows the percentage error defined as the percentage difference between observed and combination frequencies ($(100|observed-combination|/observed)$). The maximum error is less than 6%, which is below the limits set by the frequency resolution of the spectrum. For the example shown the record length for each segment is 128 points with the resulting frequency resolution of 0.078Hz (the resolution is actually even worse since the spectrum is smoothed by a five-point moving-average window).

Table 1
Frequencies associated with peaks in slope spectrum.

Peak Number	Observed Frequencies (Hz)	Combination Frequencies (Hz)	Percentage error
1	0.085	f_1	
2	0.120	f_2	
3	0.175	$2f_1$	3
4	0.224	$2f_2$	6

Given the orthogonal components of slope, it is also possible to compute the directional spectrum of the surface waves. In Figure 4.5, we showed the scatter plot of slope time series and used a best-fit line to find the wave direction. To compute direction as a function of its frequency, we use the same procedure except that we pass the slope time series through a narrow bandpass filter before estimating the direction. To account for the presence of harmonics in the time series, we use a comb filter. Figure 4.7 shows an example of the comb filter for extracting a 0.1-Hz wave. We find direction at other frequencies by sliding the filter up in frequency. Figure 4.8 shows a sample plot of the directional spectrum. For comparison, the directional spectrum measured with a pitch-and-roll buoy is also shown in the figure. We note that the two methods agree well. The squares represent data obtained from the VSG.

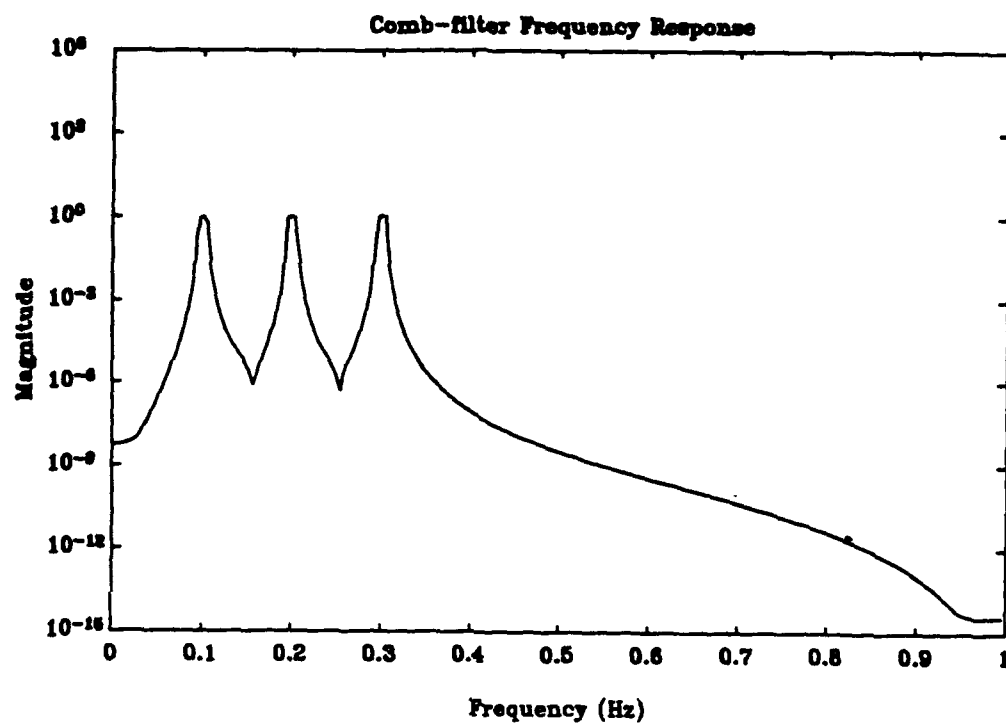


Figure 4.7. A sample comb-filter for extracting the directional spectrum. This filter extracts a wave at 0.1 Hz with its harmonics at 0.2 and 0.3 Hz.

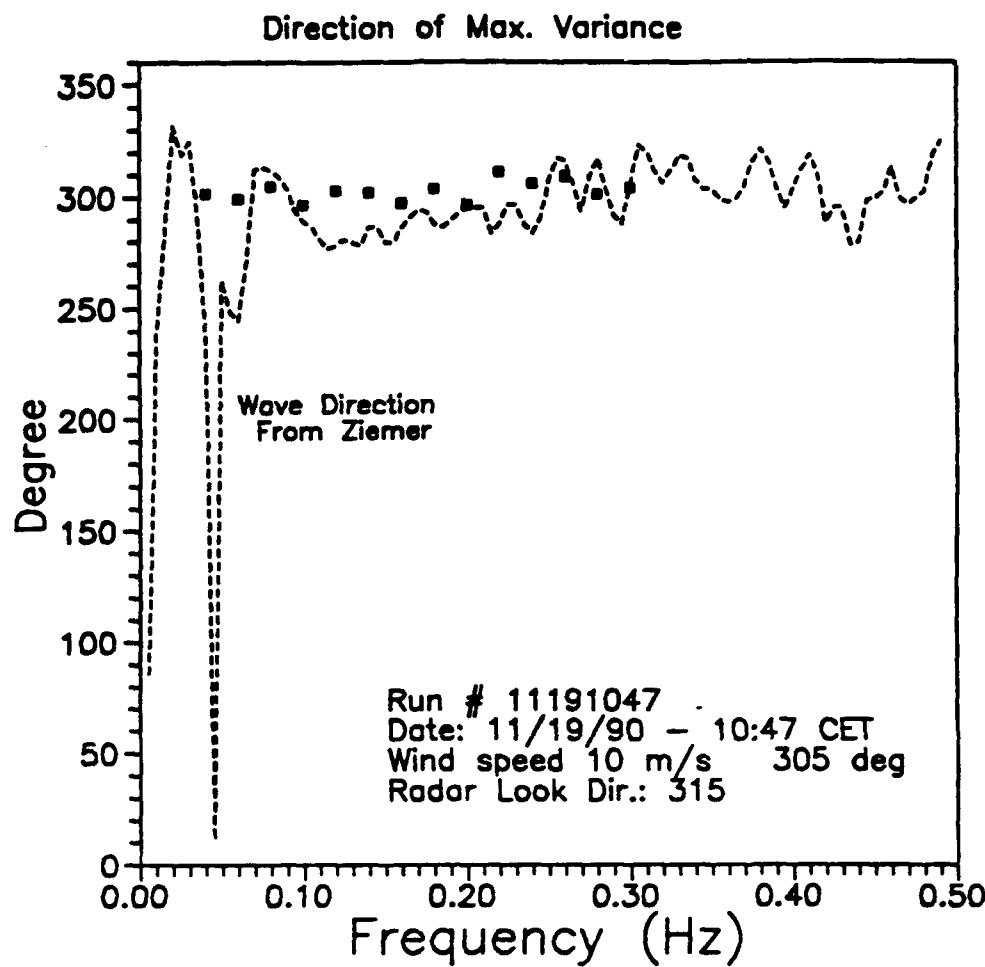


Figure 4.8 Comparison of the directional spectrum measured by the VSG and the pitch-and-roll buoy. The buoy data was provided by F. Ziemer of GKSS of Germany.

4.6) Modulation transfer function at Ka band

In this section we present examples of the Ka-band MTFs measured with the VSG during the SAXON-FPN experiment. The Modulation Transfer Function (MTF) is often used to describe the modulation of the radar signal by the long ocean waves.

The modulation transfer function $M(f)$ and the coherence function γ^2 in terms of long-wave height $w(t)$ and backscattered power $p(t)$ are given by the following equation where $G_{pw}(f)$ represents the cross spectrum of the backscattered power and the long-wave height, $G_{ww}(f)$ is the autospectrum of wave height, and \bar{p} is the mean received power (Plant, et al., 1983).

$$M(f) = \frac{G_{pw}(f)}{\bar{p} K G_{ww}(f)} \quad (19)$$

$$\gamma^2(f) = \frac{|G_{pw}(f)|^2}{G_{pp}(f) G_{ww}(f)} \quad (20)$$

K is the wave number and is given by

$$K = \frac{(2\pi f)^2}{g} ; g = 9.8 \text{ m/s}^2 \quad (21)$$

for gravity waves in deep water. The spectra are computed from 10-min segments of data by averaging 13 spectra obtained from 1-min subsets sampled at 2 Hz. The number of degrees of freedom for the spectral estimates is approximately 35.

The instantaneous backscattered power was detected by a mean-squared detector for each beam. For modulation-effect analysis, the three power measurements were averaged to reduce the effects of fading noise and "sea spikes." The sea spikes are large, discrete bursts of short duration that are not part of the Bragg-resonant scattering (Jessup et al., 1990, and Bush, 1990). Saliam, et al. (1992) describes the procedure used here to remove spikes from the data and replace them by weighted means of the adjacent values. For the upwind cases, most of the spike energy is concentrated at the high frequencies between 0.2 and 0.4 Hz. In general, the spikes have little effect on the spectra at low frequency where the dominant wave is located. Nonetheless, removing the spikes results in higher values of the coherence function at low frequencies around the dominant wave frequency. Near the frequency of the dominant wave spikes have little effect on the magnitude of the MTF, but they cause a slight increase (10° to 15°) in its phase. The general decrease of MTF magnitude with increasing long-wave frequency, coherence values of 0.5 to 0.8 near the dominant-wave frequency, and increased coherence with the removal of spikes are all characteristics of most of the upwind runs.

The number of independent samples for each beam is the number of the resolution cells within the antenna footprint. For small beamwidths, the number of independent samples is (Ulaby, et al., 1982)

$$N = \frac{2 h \alpha B \tan \theta}{c \cos \theta} \quad (22)$$

where h is the antenna height, θ is the pointing angle, B is the sweep bandwidth, and α is the antenna beamwidth. With $h=20\text{m}$, $\theta=45^\circ$, $B=300\text{ MHz}$, and $\alpha=2.5^\circ$, we have $N=2.5$. Since the VSG beams were slightly offset with respect to each other, three independent measurements of the scattering were available for each height measurement. By averaging the returns of the three beams the total number of independent samples is 7.5.

Figure 4.9 shows a sample upwind/upwave Ka-band MTF run. Relatively high values of coherence, around 0.7 at dominant wave frequency, are typical of the upwind runs. In all of the subsequent MTF plots, values corresponding to low coherence points (less than 0.25) are omitted (Plant, et al., 1983). This means that the estimates of the MTF remain within 32% of the actual values 95% of the time. The values of the phase of the MTF describe the location of the maximum radar return relative to the long-wave crest. The phase of MTF is near 90° , indicating that the maxima, due to combined slope and hydrodynamic modulation, is roughly 90° ahead of long-wave crest.

Figure 4.10 shows the dependence, at the dominant wave frequency, of the magnitude and phase of the upwind/upwave MTF on the wind speed. For all of the runs analyzed, the dominant wave frequency was between 0.1 Hz and 0.35 Hz. MTF values within 1-m/s windspeed ranges were averaged to determine the

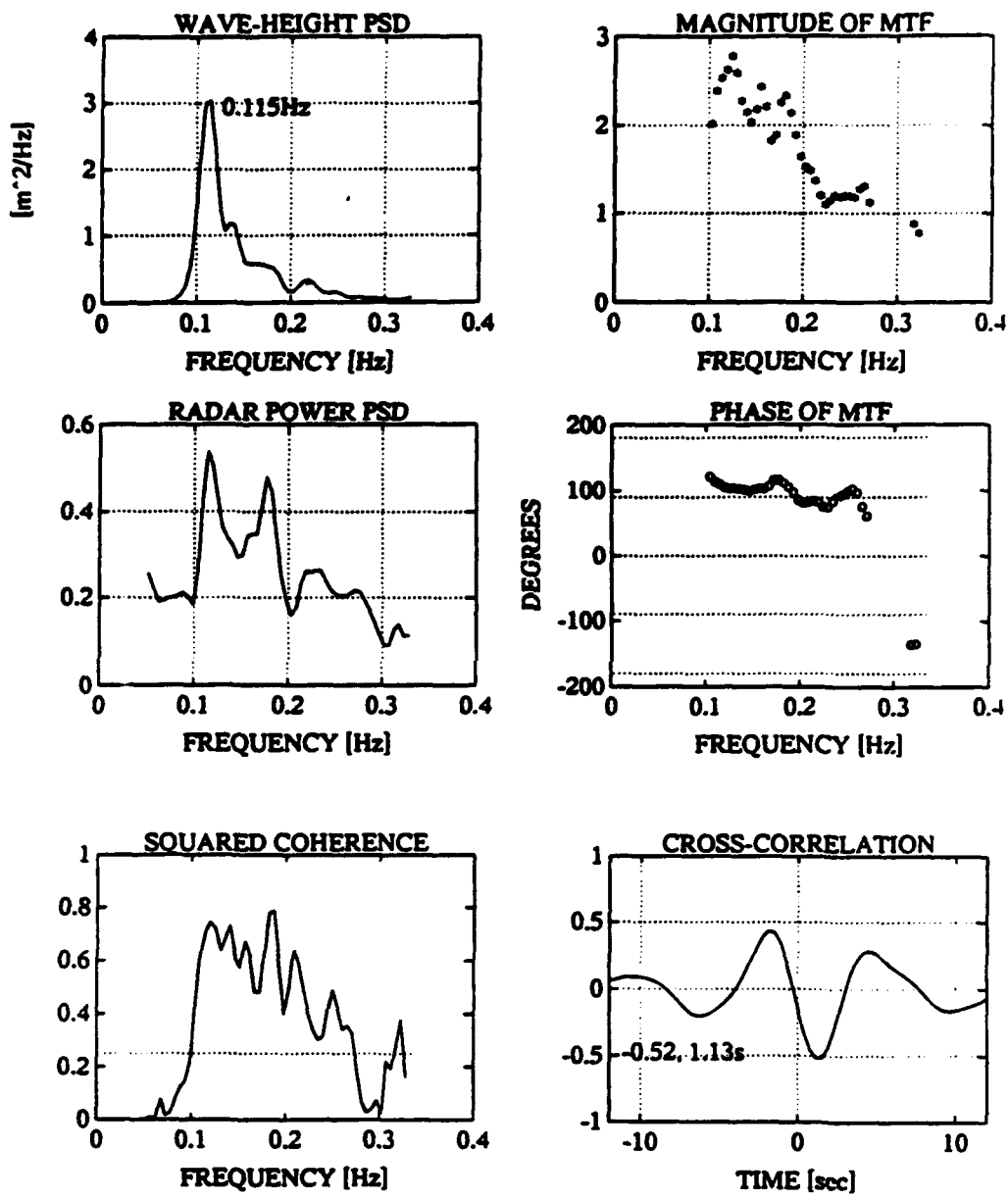


Figure 4.9. Sample Ka-band upwind/upwave MTF. Wind speed is 12 m/s in the upwind direction, and incidence angle is 45°.

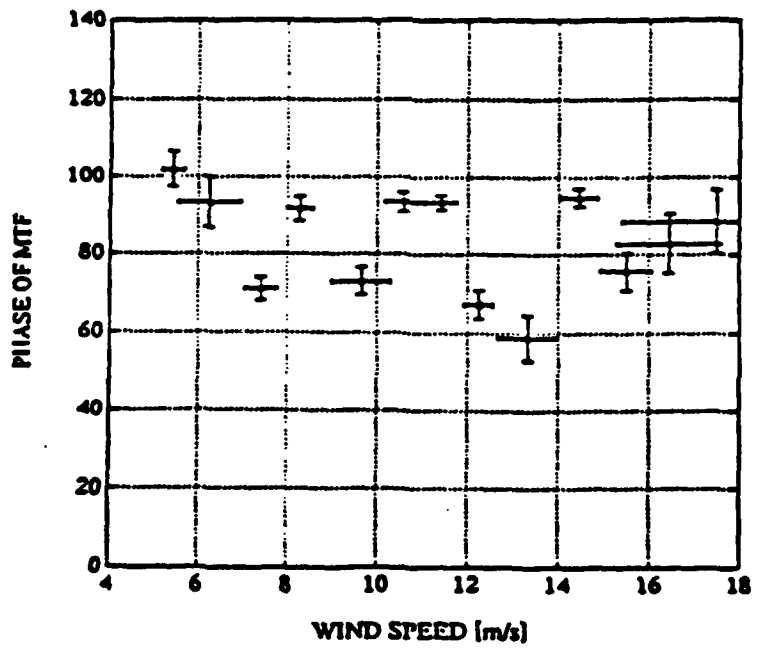
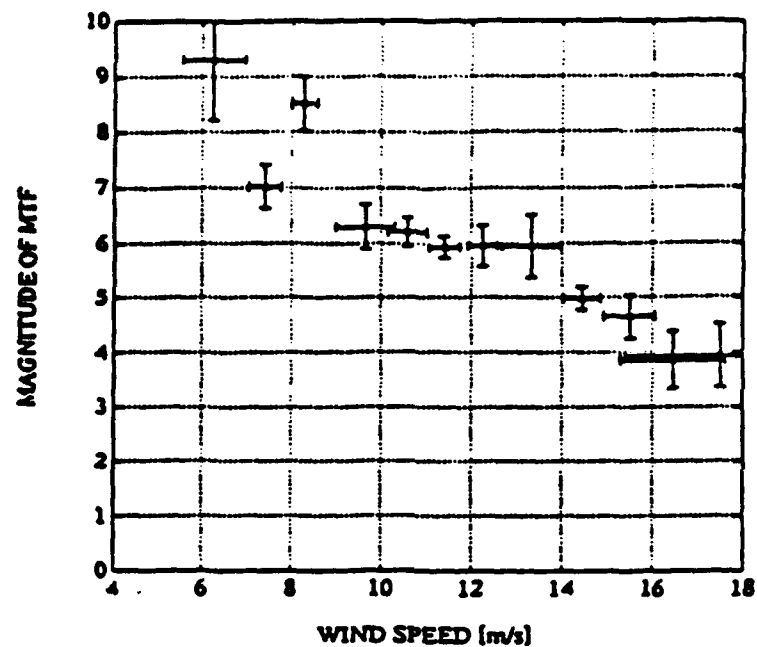


Figure 4.10 Dependence of upwind/upwave Ka-band MTF on the wind speed. Each point represents the average over 1-m/s wind speed interval. The incidence angle is between 45° to 55° . Error bars indicate 95% confidence interval.

average dependence of the MTF on the wind speed. The graphs also show the 95% confidence intervals. All values of the magnitude and phase of the MTF with coherence values greater than 0.4 and within the frequency range of 0.1 to 0.35 Hz were averaged. The magnitude of the MTF decreases monotonically with increasing wind speed.

4.7) Conclusion

We operated the Vector Slope Gauge (VSG) during the SAXON-FPN experiment. We presented an algorithm for calculating the orthogonal components of slope from the VSG range measurements. We also introduced a new algorithm for calculating the direction of the dominant wave travel.

As a Ka-band scatterometer, the VSG made instantaneous measurements of the large-scale wave height and the backscattered power. These measurements were used to calculate the Ka-band MTFs. The magnitudes of the upwind MTF showed a distinct inverse relation to the wind speed. The phases of the upwind MTF were always positive, indicating that the Ka-band scatterers (wavelength about 0.5 cm) were located on the front faces of the large-scale waves.

Chapter 5

MEASUREMENT OF HYDRODYNAMIC MODULATION OF RADAR SCATTER FROM THE SEA

5.1) Introduction:

Many important ocean surface features, including wave direction and spectra, can be determined from radar images. Despite many theoretical and empirical investigations, the modulation of the radar signal by the ocean waves, vital to the understanding of radar imaging, is not well understood. The SAR imaging process itself is well developed, but it can only have maximum value if the signal modulation is understood. The vector slope gauge 3) offers an opportunity to explore this effect without the bulky equipment needed to do so other ways in the open sea.

Backscatter from the ocean surface is often assumed to be entirely due to Bragg scattering. Wright (1968) found that ripples of wave number $K = 2k\sin\theta_L$ (the Bragg-resonance condition) dominate the scattering at middle incidence angles. Here k is the wave number of the radar signal and θ_L is the local angle of incidence. In the two-scale version of the theory, one assumes the scattering cross

section depends on the *local* angle of incidence, which changes with tilting of the ripples by the large-scale wave slopes (tilt modulation), and on variations in ripple amplitude (hydrodynamic modulation).

In previous chapters, we described the operation of the radar vector slope gauge. The VSG provides simultaneous measurements of the orthogonal components of the surface slopes within the radar footprint and the microwave scattered power. This permits the separation of effects due to the surface tilting from hydrodynamic effects; that has not been previously possible. Here we outline a new procedure for determining the hydrodynamic transfer functions, which characterizes the modulation of the short ripples by the large-scale ocean waves. We include results with this approach on data measured by the VSG during the SAXON-FPN experiment in November 1990, on the German NORDSEE platform.

5.2) The radar cross-section modulation

The backscatter from the ocean surface is frequently attributed to Bragg scattering. With Bragg scattering, only ripples of wavenumber $2k \sin \theta_L$ contribute to the scattering. The return for vertical polarization is greater than that for horizontal polarization, and the ratio increases with the angle of incidence and the relative dielectric constant of the water.

The radar returns to a scatterometer viewing the ocean surface are modulated by the passing large-scale waves (Plant and Keller, 1983; Keller, et al., 1985). Many attempts have been made to relate empirically the radar-return signal to the ocean wave parameters. Most of these investigations involve the calculation of a modulation transfer function (MTF), which relates the instantaneous received power to the slope of the large-scale waves.

The MTF is currently the primary descriptor used to explain the radar cross-section modulation. Under this theory, the small-scale Bragg ripples, modulated by the large-scale ocean waves, are the primary source of the electromagnetic scattering. The MTF is used as a tool for understanding the relations between radar backscatter and ocean waves and as an aid in developing simulations of the SAR imaging of the ocean. The MTF also has been used by some investigators to verify the validity of some of the proposed ocean-backscatter models.

The Modulation Transfer Function (MTF): The definition of the MTF for a long-crested wave traveling parallel to the radar beam (in the upwind or downwind direction) based on the waveheight was given in the previous chapter. The slope MTF is given by

$$M(f) = \frac{G_{ps}(f)}{\bar{p} G_{ss}(f)} \quad (1)$$

where $G_{ps}(f)$ represents the cross spectrum of the backscattered power and the long-wave slope and $G_{ss}(f)$ is the autospectrum of the slope. The mean received power \bar{p} normalizes $M(f)$, making it dimensionless. The factor $G_{ps}(f)$ is a complex quantity, and its phase provides the phase of the MTF. The above definition assumes that the relation between the radar backscattered power and the long-wave slope is linear and can be described as a transfer function $M(f)$.

The MTF can be expressed in terms of the long-wave height if one assumes long-crested waves, with no slopes parallel to the crests, and that linearity assumptions are valid. The MTF, in terms of waveheight, is given by

$$M(f) = \frac{G_{pw}(f)}{\bar{p} K G_{ww}(f)} \quad (2)$$

$$K = \frac{(2\pi f)^2}{g}; \quad g = 9.8 \text{ m/s}$$

where $G_{pw}(f)$ is the cross spectrum of power and waveheight, and $G_{ww}(f)$ is the autospectrum of waveheight.

The cross-section modulation by the long waves is due to two effects: (1) the tilt modulation and (2) the hydrodynamic modulation. The tilt modulation is due to a purely geometric effect, since Bragg ripples are seen by the radar at different local angles of incidence depending on their location on the long waves. The hydrodynamic modulation is characterized by the modulation of the short

ripples, both in phase and amplitude, by the long ocean wave.

5.3) Tilt modulation

Based on first-order small-perturbation scattering theory, the radar cross-section per unit area of the ocean is given as (Valenzuela, 1978)

$$\sigma_{vv}^o = 4\pi k^4 \cos^4 \theta_L \left| \left(\frac{\sin(\theta + \psi) \cos \delta}{\sin \theta_L} \right)^2 g_{HH}(\theta_L) + \left(\frac{\sin \delta}{\sin \theta_L} \right)^2 g_{VV}(\theta_L) \right|^2 \times W(2k \sin(\theta + \psi), 2k \cos(\theta + \psi) \sin \delta) \quad (3)$$

$$\sigma_{HH}^o = 4\pi k^4 \cos^4 \theta_L \left| \left(\frac{\sin(\theta + \psi) \cos \delta}{\sin \theta_L} \right)^2 g_{VV}(\theta_L) + \left(\frac{\sin \delta}{\sin \theta_L} \right)^2 g_{HH}(\theta_L) \right|^2 \times W(2k \sin(\theta + \psi), 2k \cos(\theta + \psi) \sin \delta) \quad (4)$$

where θ_L is the local angle of incidence, ψ and δ are the orthogonal components of the surface slope in the range and cross-range directions, θ is the angle of incidence, and k is the radar wavenumber. The wavenumber spectral density of the ocean surface $W(K_x, K_y)$ is evaluated at the Bragg resonant wavenumber

$$K_B = \{2k \sin(\theta + \psi), 2k \cos(\theta + \psi) \sin \delta\} \quad (5)$$

The polarization coefficients are (Valenzuela, 1978; Wright, 1968)

$$g_{HH}(\theta_L) = \frac{\epsilon - 1}{[\cos \theta_L + (\epsilon - \sin^2 \theta_L)^{1/2}]^2} \quad (6)$$

$$g_{VV}(\theta_L) = \frac{(\epsilon - 1)[\epsilon(1 + \sin^2 \theta_L) - \sin^2 \theta_L]}{[\epsilon \cos \theta_L + (\epsilon - \sin^2 \theta_L)^{1/2}]^2} \quad (7)$$

5.4) Short-wave spectra

The first-order Bragg theory relates the microwave scattering to the spectral amplitude of short waves of lengths comparable to the microwave wavelength. In order to apply the Bragg theory, we need a description of the short-wave (ripple) spectrum.

The generation and evolution of ripples on the ocean surface is a complicated process. Input from the wind, the energy transfer among the wave components by nonlinear wave-wave interactions, and dissipation due to wave breaking are the main factors governing the evolution of ripple spectrum (Phillips, 1985).

The most widely used model of ripple spectrum has been the Phillips spectrum. Assuming that the short-wave growth is limited by wave breaking, Phillips proposes the spectral form, $W(K) = A K^{-4}$, where K is the ripple wavenumber, and A is a constant (Phillips, 1958). In the capillary region, wavelengths of about 0.5 to 2 cm, Donelan and Pierson (1987) propose a similar spectral form. However, they predict a cut-off wavelength where the ripple spectrum begins to fall off rapidly. This cut-off wavelength is a strong function of wind speed and the water temperature. Kitaigorodskii (1983), suggests that the exponent of the ripple spectrum is -3.5 for short gravity waves, but in the capillary region the exponent drops to -4 due to the dominance of wave breaking.

There is some experimental evidence indicating that at high wave numbers

a spectral form close to that of Phillips's K^{-4} is appropriate. Most of these measurements extract the short-wave spectra from measured microwave data (Valenzuela, 1976; Lawner et al. 1984; Jackson et al. 1985). Recent optical measurements by Jahane et al. (1990), further support the K^{-4} spectral form for ripples in the capillary region.

Assuming that the short wave-field is isotropic, we use the following expression for the ripple spectrum.

$$S(K) = AK^{-4} \quad (8)$$

where $|K| = \sqrt{K_x^2 + K_y^2} = K$.

We find the ripple spectrum, at the Bragg-resonant wavenumber K_b , by substituting (5) for K .

$$\begin{aligned} S(K_b) &= AK^{-4} \\ &= (2k)^{-4} [\sin^2(\theta + \psi) + \cos^2(\theta + \psi) \sin^2\delta]^{-2} \\ &= (2k)^{-4} [1 - \cos^2\delta \cos^2(\theta + \psi)]^{-2} \end{aligned} \quad (9)$$

The second term in the bracket is the local angle of incidence.

$$\cos\theta_L = \cos\delta \cos(\theta + \psi) \quad (10)$$

Therefore,

$$\begin{aligned}
 S(K_s) &= (2k)^{-4} [1 - \cos^2\delta \cos^2(\theta + \psi)]^{-2} \\
 &= (2k)^{-4} [1 - \cos^2\theta_L]^{-2} \\
 &= [2k \sin\theta_L]^{-4}
 \end{aligned} \tag{11}$$

Substituting (11) into (3), the tilt modulation for VV polarization is given by

$$\sigma_{rr}^o(\psi, \delta) = \frac{\pi}{4} A k^4 \cot^4 \theta_L \times$$

$$\left| \left(\frac{\sin(\theta + \psi) \cos \delta}{\sin \theta_L} \right)^2 g_{HH}(\theta_L) + \left(\frac{\sin \delta}{\sin \theta_L} \right)^2 g_{VV}(\theta_L) \right|^2 \tag{12}$$

The polarization coefficients g_{HH} and g_{VV} , (6) and (7), depend only on θ_L . The local angle of incidence θ_L is a function of the local surface slopes as indicated by (10). The above equation relates the radar cross section to the orthogonal components of surface slopes ψ and δ . Note that the above function depends on time because ψ and δ , and thus θ_L , depend on t. The VSG measures time series of ψ and δ . Therefore, we use (12) to predict cross-section modulation due to the tilting of the surface.

The hydrodynamic modulation is due to modulation of the ripple amplitude by the large-scale waves. The Bragg-resonant condition defines the particular component of the surface ripple that is resonant to the radar signal. The instantaneous radar signal power is directly proportional to the strength of the resonant ripple spectral component. Assuming that the hydrodynamic modulation

is linear in long-wave amplitude, we represent the modulation by m_h in

$$W(K_B) = S(K_B) m_h \quad (13)$$

Therefore, we write the total cross section as

$$\sigma_{total}^o = \sigma_{tilt}^o m_h \quad (14)$$

In terms of microwave received power, we write (14) as

$$p(t) = C_m p_T(t) p_H(t) \quad (15)$$

where C_m is an unknown constant to be determined. It depends on radar calibration constants that relate the radar cross section σ^o to the return power $p(t)$. The constant C_m is also a function of A , the mean amplitude of the ripple spectrum, that is unknown. The factors $p_T(t)$ and $p_H(t)$ account for the tilt and hydrodynamic contributions to total signal modulation. The above equation assumes that $\bar{p}_H = 1$, or $\bar{p} = \bar{p}_T$, where the bar over a variable indicates the time-averaged value.

5.5) A model for cross section modulation

Figure 5.1 shows a general model for the modulation process. It consists of a dual-input/single-output model with parallel linear and nonlinear components. The inputs are the long-wave height and the orthogonal components of slope ψ and δ . The output is the microwave return power. We have expressed the total return power $p(t)$ as the product of the hydrodynamic modulation $p_H(t)$ and tilt

modulation $p_7(t)$ contributions.

The top branch in the block diagram corresponds to the hydrodynamic modulation. It shows the hydrodynamic modulation as being directly correlated with the long-wave heights. We represent the hydrodynamic modulation as a linear transfer function $M_H(f)$. The lower branch of the block diagram represents the tilt modulation of the radar return power. The form of the nonlinearity σ_{til}^o is known, and is given by (12).

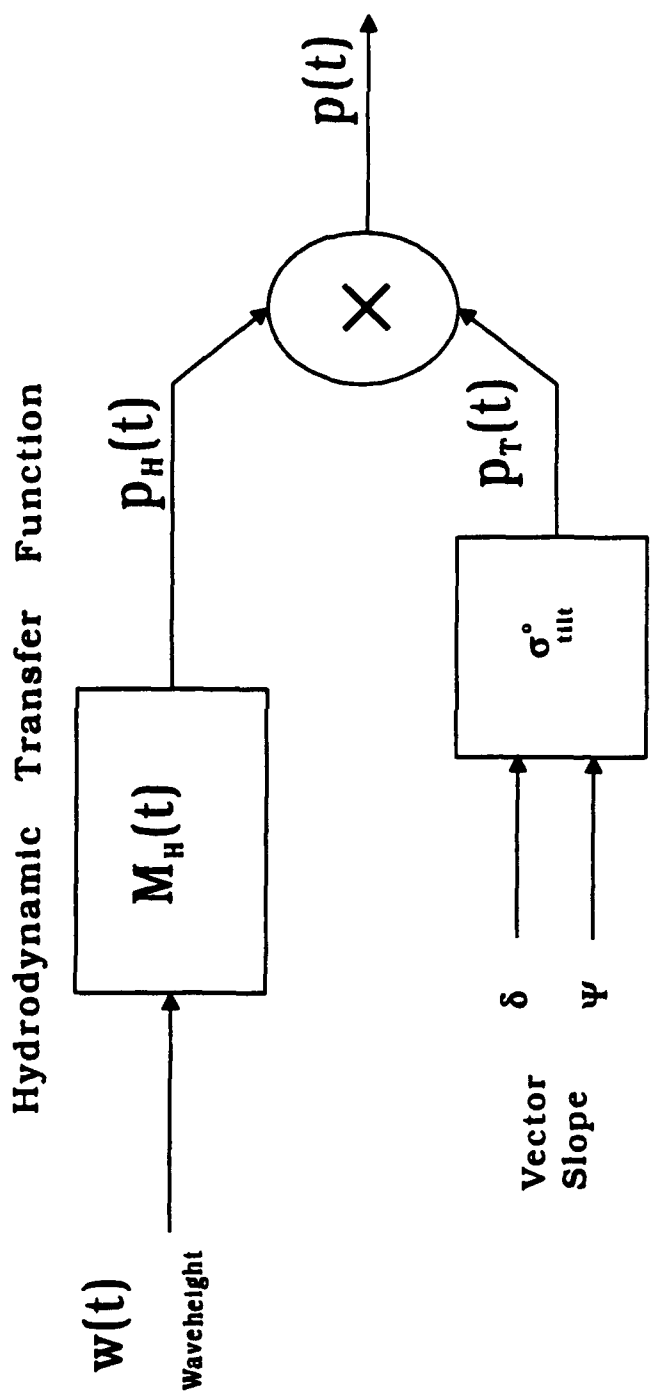


Figure 5.1 A model of the radar signal modulation.

Our procedure for estimating the hydrodynamic modulation is as follows:

- a) we use (6), (7),(10), and (12) to find the tilt modulation contribution using the VSG measurements of δ and ψ . b) since the received power $p(t)$ is measured simultaneously, we estimate the hydrodynamic modulation contribution by inverting (15).

$$p_H(t) = \frac{p(t)}{C_m p_T(t)} \quad (16)$$

- c) finally, we estimate the hydrodynamic modulation transfer function from

$$M_H(f) = \frac{G_{wp_n}(f)}{G_{ww}(f)} \quad (17)$$

We still need to determine the unknown constant C_m . We find C_m by taking the average of both sides from (15). Recalling $\bar{p}_H(t) = 1$, we obtain

$$C_m = \frac{\bar{p}}{\bar{p}_H \bar{p}_T} = \frac{\bar{p}}{\bar{p}_T} \quad (18)$$

Combining (16) and (18), we obtain

$$p_H(t) = \frac{p(t)/\bar{p}}{p_T(t)/\bar{p}_T} \quad (19)$$

It is important to note that, since the VSG provides direct measurement of both $w(t)$ and $s(t)$, no assumption regarding the relationship between waveheight and slope is needed. With point-measuring radars that only measure the height (or orbital velocity) of long waves, one is forced to assume linearity and estimate the slopes from waveheight. Moreover, without the direct measurements of the orthogonal components of slope, one has to linearize (12) to estimate tilt. Next, we

show that the first-order approximations of our procedure reduces to the linear models currently used to obtain the hydrodynamic modulations.

5.6) First-order approximation of the hydrodynamic effects

The linear term is the first term in the Taylor series expansion. The first-order Taylor series approximation of (15) gives

$$p(t) = C_m \left[\bar{p}_T \bar{p}_H + (p_T(t) - \bar{p}_T) \bar{p}_H + (p_H - \bar{p}_H) \bar{p}_T \right] \quad (20)$$

where C_m is defined by (18). Solving for $p_H(t)$, and simplifying we obtain

$$p_H(t) = \frac{p(t)}{C_m p_T} + \frac{\bar{p}}{p_T} - \frac{p_T(t)}{p_T} \quad (21)$$

Substituting (18) for C_m , we have

$$p_H(t) = \frac{p(t)}{p} - \frac{p_T(t)}{p_T} + \frac{\bar{p}}{p_T} \quad (22)$$

The last term is the constant C_m and, without any loss in generality, we can drop it since it simply represents a DC term. Thus, we have

$$p_H(t) = \hat{p}(t) - \hat{p}_T(t) \quad (23)$$

where the hat over a variable name indicates that it is normalized by its mean.

The above equation expresses the total signal modulation as the sum of hydrodynamic and tilt modulation terms.

We model the measurement noise by an additive term $n(t)$. We assume that $n(t)$ is uncorrelated with $\hat{p}_H(t)$ and $\hat{p}_T(t)$. The total normalized output $\hat{p}(t)$ is,

thus, given by

(24)

$$\hat{p}(t) = \hat{p}_H(t) + \hat{p}_T(t) + n(t)$$

We do not put any restrictions on output noise $n(t)$; that is, it can be non-white and non-Gaussian. The input and, therefore, the output data can be either Gaussian or non-Gaussian.

The Fourier Transform of (24) gives

(25)

$$\hat{P}(f) = \hat{P}_H(f) + \hat{P}_T(f) + N(f)$$

where capital letters represent transformed variables and f is the long-wave frequency.

To estimate $M_H(t)$, we find the cross spectrum $G_{sp}(f)$ of $s(t)$ and $\hat{p}(t)$.

Here $s(t)$ is the magnitude of long-wave slope. The cross spectrum is defined as

$$G_{sp}(f) \triangleq \frac{1}{T} \langle S^*(f) \hat{P}(f) \rangle \quad (26)$$

where T , the averaging period, is assumed to be infinitely long. Substituting for $\hat{p}(f)$ from (25), we obtain

$$\begin{aligned} G_{sp}(f) &= \frac{1}{T} \langle S^*(f) \hat{P}_H(f) \rangle + \frac{1}{T} \langle S^*(f) \hat{P}_T(f) \rangle \\ &\quad + \frac{1}{T} \langle S^*(f) N(f) \rangle \end{aligned} \quad (27)$$

The last term is zero, since $N(f)$ and $S(f)$ are uncorrelated. Therefore,

(28)

$$G_{sp}(f) = G_{sp_n}(f) + G_{sp_r}(f)$$

Next, we divide both sides by $G_{ss}(f)$.

$$\frac{G_{sp}(f)}{G_{ss}(f)} = \frac{G_{sp_n}(f)}{G_{ss}(f)} + \frac{G_{sp_r}(f)}{G_{ss}(f)} \quad (29)$$

The tilt and total modulation transfer functions, $M_T(f)$ and $M(f)$, are given by

$$M_T(f) = \frac{G_{sp_r}(f)}{G_{ss}(f)} \quad (30)$$

$$M(f) = \frac{G_{sp_n}(f)}{G_{ss}(f)}$$

Therefore,

$$M(f) = \frac{G_{sp_n}(f)}{G_{ss}(f)} + M_T(f) \quad (31)$$

The first term on the right-hand side represents the hydrodynamic modulation in terms of the slope. However, the hydrodynamic modulation is related to the long-wave height. To proceed, we must resort to the linear wave theory. For long-crested waves, the linear wave theory predicts that the transfer function $A(f)$ relates the long-wave height to its slopes, where

$$A(f) = jK = \frac{j(2\pi f)^2}{g} \quad (32)$$

here, f is the long-wave frequency, K is its wavenumber, $g=9.8$ m/s, and j accounts for the 90° phase difference between waveheight and slope. Then, we have

$$\begin{aligned} G_{ss}(f) &= K^2 G_{ww}(f) \\ G_{sp_n}(f) &= jKG_{wp_n}(f) \end{aligned} \tag{33}$$

Substituting (33) into (32), and recalling that the hydrodynamic transfer function is

$M_H(f) = \frac{G_{wp_n}(f)}{G_{ww}(f)}$, we obtain

$$M(f) = \frac{jM_H(f)}{K} + M_T(f) \tag{34}$$

Solving for the hydrodynamic transfer function, we get

$$M_H(f) = -jK [M(f) - M_T(f)] \tag{35}$$

This is the form that is currently used by investigators to relate the tilt, hydrodynamic, and total modulation transfer functions (Alpers, 1981; Ocampo-Torres, et al., 1990). The above equation agrees with the earlier work of Keller and Wright (1975). However, they used a different approach, based mainly on hydrodynamic considerations, to arrive at the same results.

With point measuring systems, one cannot directly evaluate the tilt transfer function $M_T(f)$. A common approximation is to replace $M_T(f)$ by its first-order linear approximation m_T (Alpers, 1981; Schroter, et al., 1986; Ocampo-Torres, et al., 1990; Plant, 1991). The first-order approximation of the tilt modulation is (Alpers, 1981)

$$m_T = \left[\frac{1}{\sigma_{tilt}^0} \frac{\partial \sigma_{tilt}^0}{\partial \psi} \right]_{\psi=0, \delta=0} \sin\phi_o + \left[\frac{1}{\sigma_{tilt}^0} \frac{\partial \sigma_{tilt}^0}{\partial \delta} \right]_{\psi=0, \delta=0} \cos\phi_o \quad (36)$$

where σ_{tilt}^0 is given by (12), and ϕ_o is the azimuth direction of the long wave. Note that m_T is not a function of frequency and depends only on the incidence angle.

The VSG measurements of vector slopes allow determination of the hydrodynamic modulation without any of the linearity assumptions outlined in this section. We described this procedure in the previous section.

5.7) Effect of the nonlinearity σ_{tilt}^0

To properly characterize the modulation, it is important to account for the nonlinear behavior of the tilt modulation. Next we briefly discuss the effect of the tilt nonlinearities on modulation transfer calculations.

Figure 5.2 shows the normalized tilt cross section versus ψ , the slope in the up-wave direction, for VV polarization. The nonlinearity increases significantly with a decreasing incidence angle. Figure 5.3 shows the dependence of the tilt cross section on the exponent of ripple spectrum γ for an incidence of 40° . As one would expect, the nonlinearities increase with increasing γ . Figure 5.4 and 5.5 show similar plots for HH polarization. Comparing Figures 5.2 and 5.5, we note that the tilt modulation is more nonlinear for HH polarization than VV.

Figure 5.6 and 5.7 show sample simulations, illustrating the effect of nonlinearity on the MTF calculation, for HH and VV polarizations. An actual VSG data set, measured during the SAXON-FPN, is used for the waveheight. For the purpose of this simulation, we assume that only long-crested, unidirectional waves are present and, therefore, the linear wave theory is applicable. Thus, the long-wave slopes are calculated by passing the waveheight time series through the linear transfer function $A(f)$ given by (32). We then generated simulated time

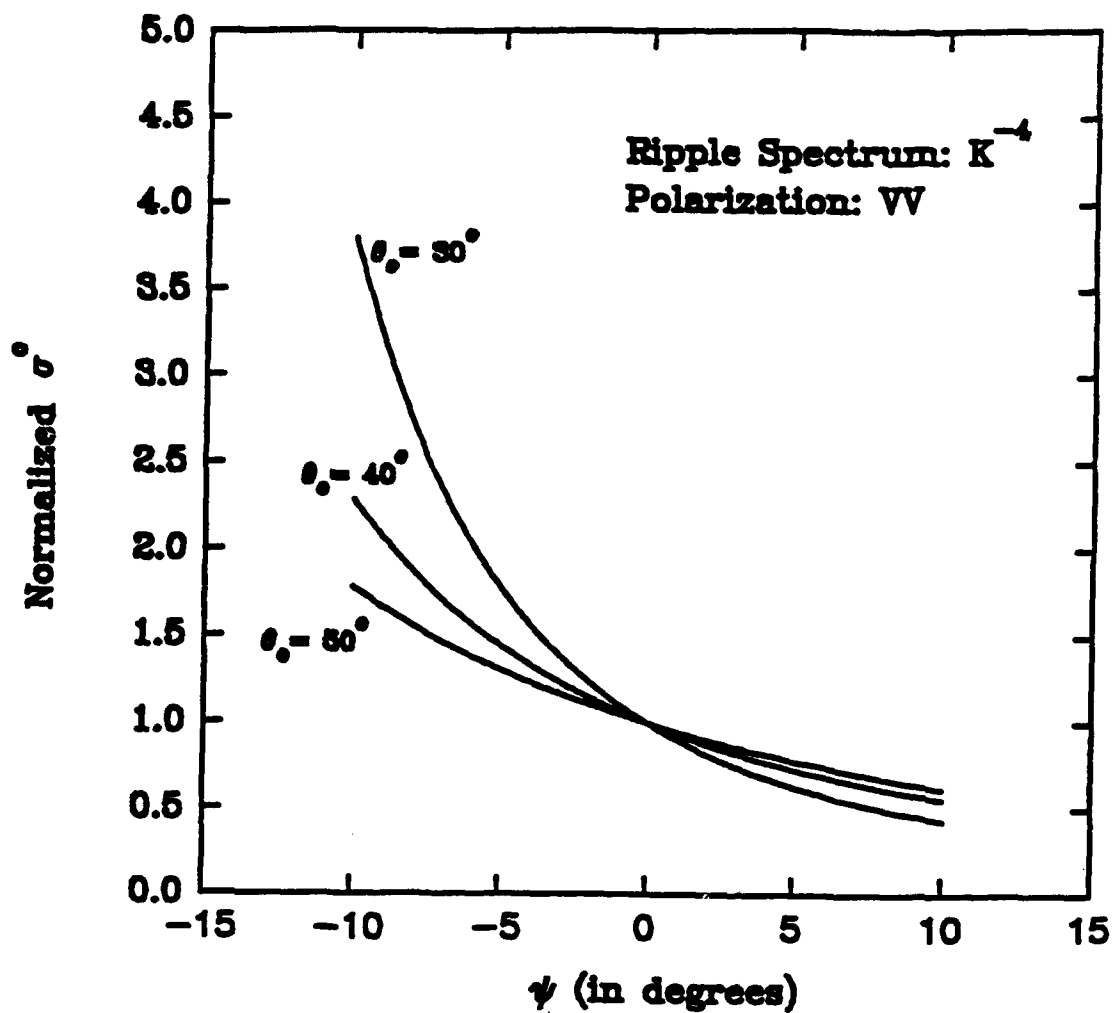


Figure 5.2 $\sigma^{\circ}(\Psi, \delta)/\sigma^{\circ}(0,0)$ versus Ψ , slope in the radar-look direction, for various incidence angles θ_0 for VV polarization.

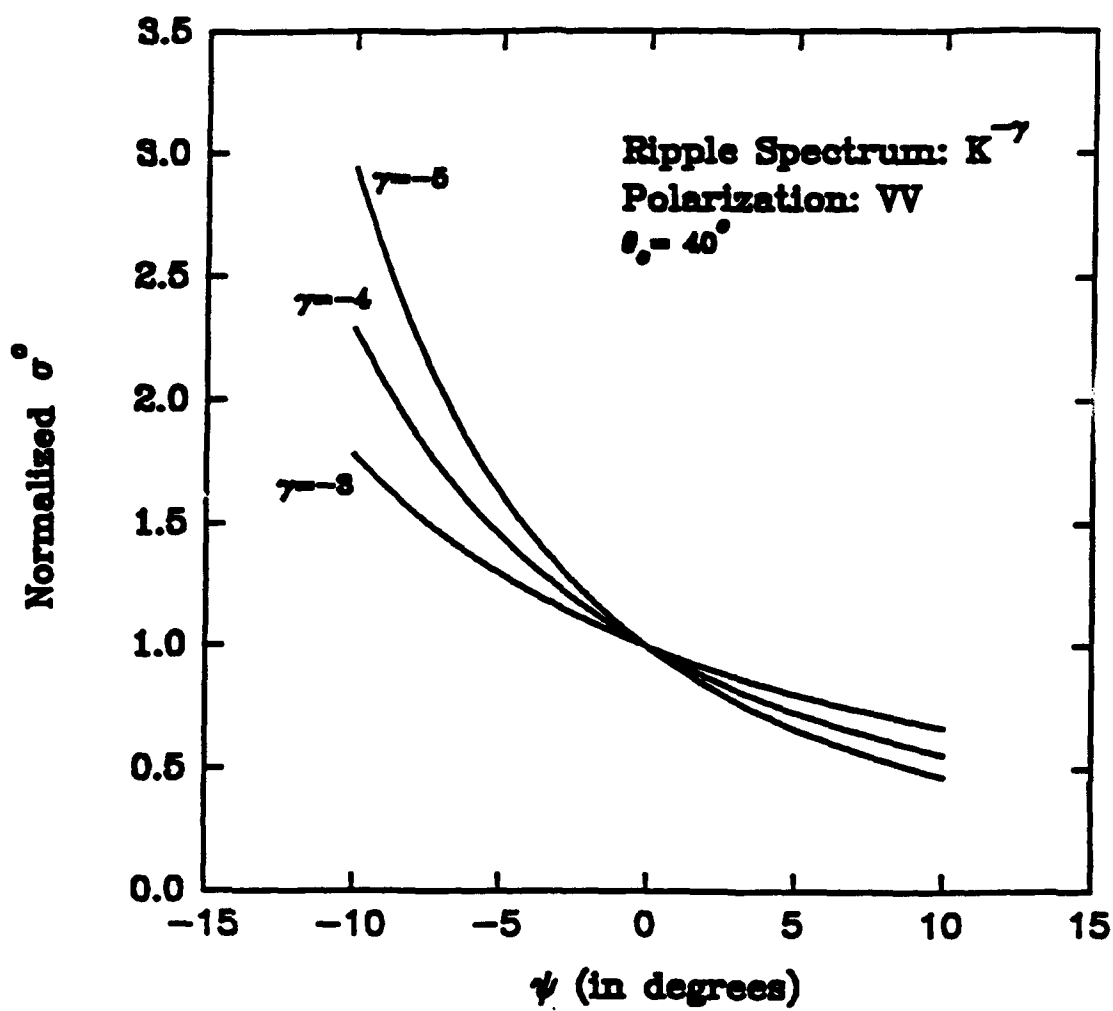


Figure 5.3 Dependence of the normalized radar cross section on the exponent of the ripple spectrum γ at an incidence angle of 40° for VV polarization.

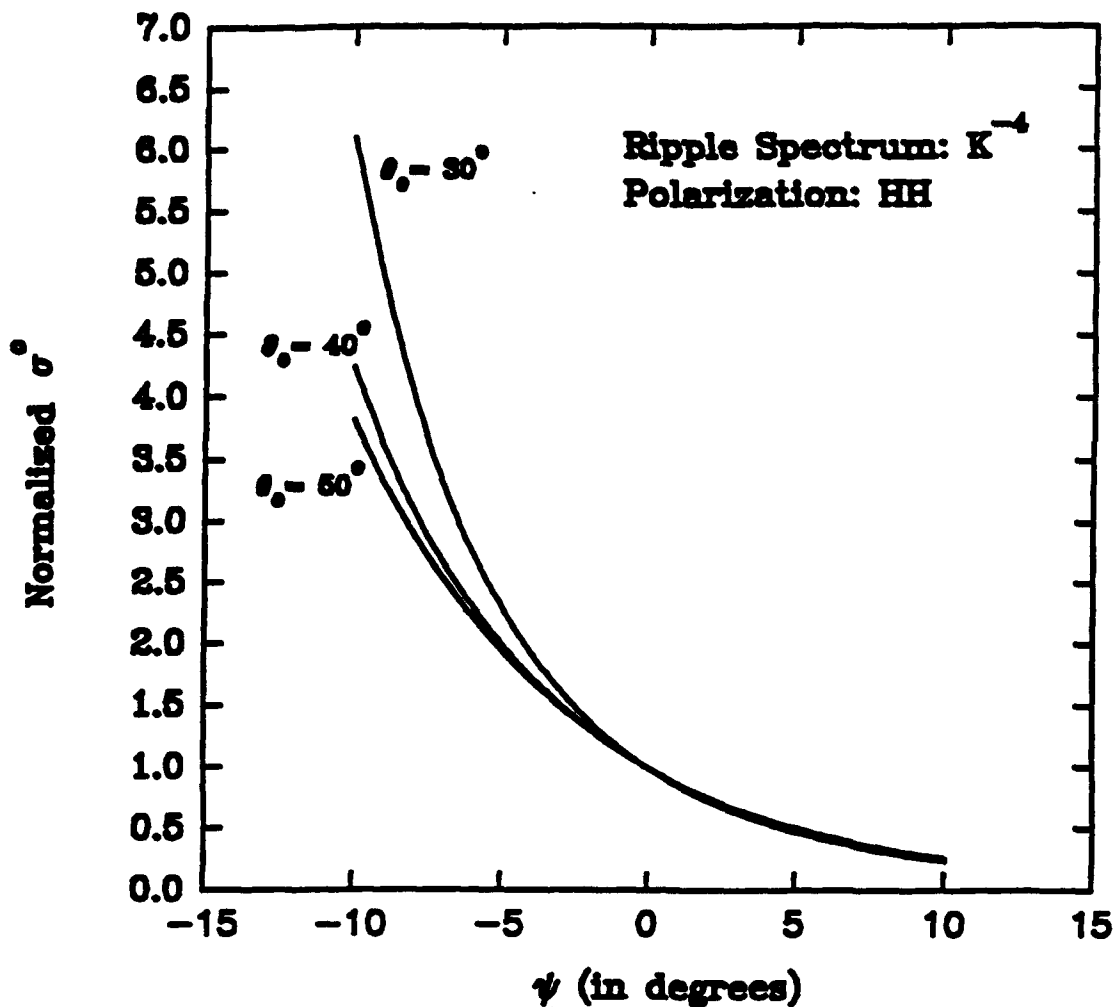


Figure 5.4 $\sigma^\circ(\Psi, \delta)/\sigma^\circ(0,0)$ versus Ψ , slope in the radar-look direction, for various incidence angles θ_0 for HH polarization.

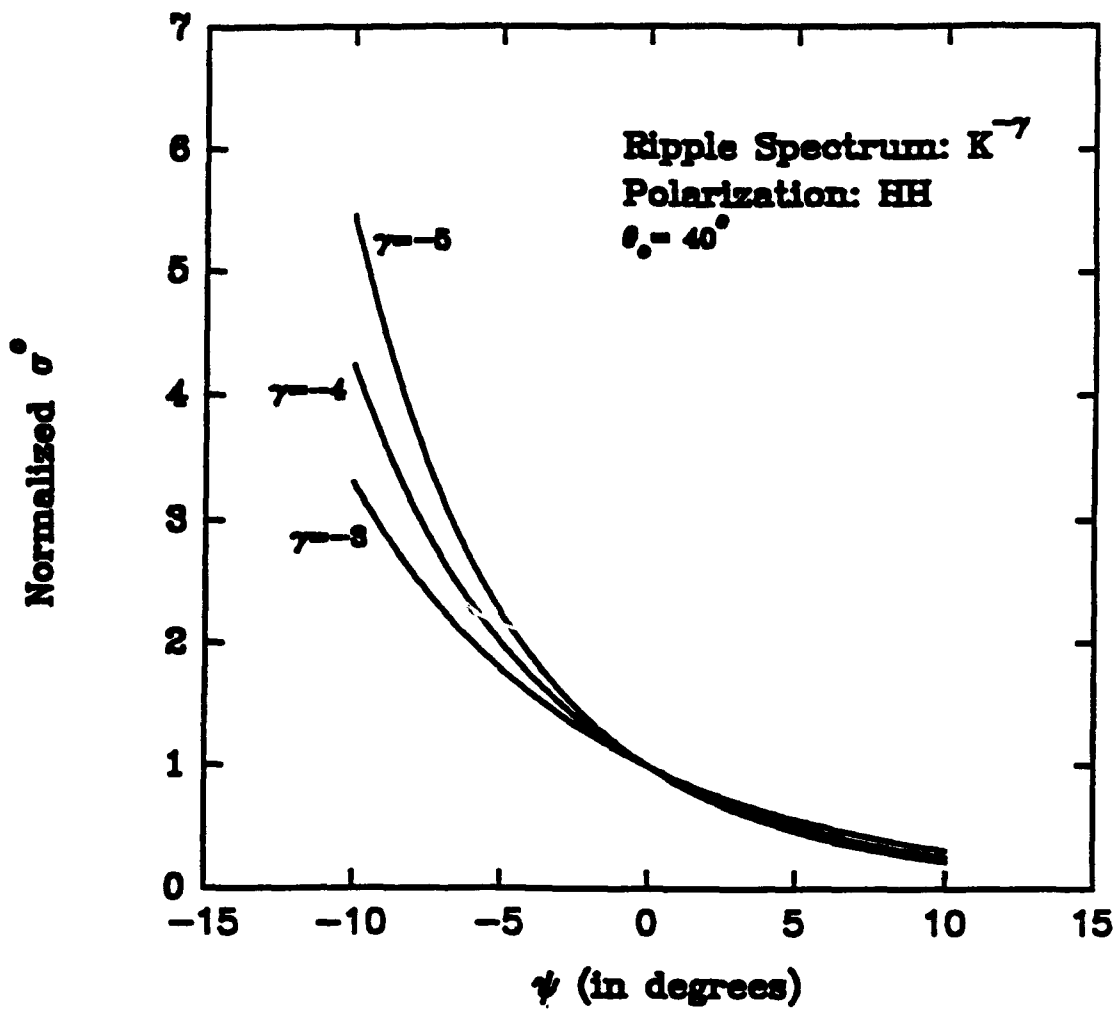


Figure 5.5 Dependence of the normalized radar cross section on the exponent of the ripple spectrum γ at an incidence angle of 40° for HH polarization.

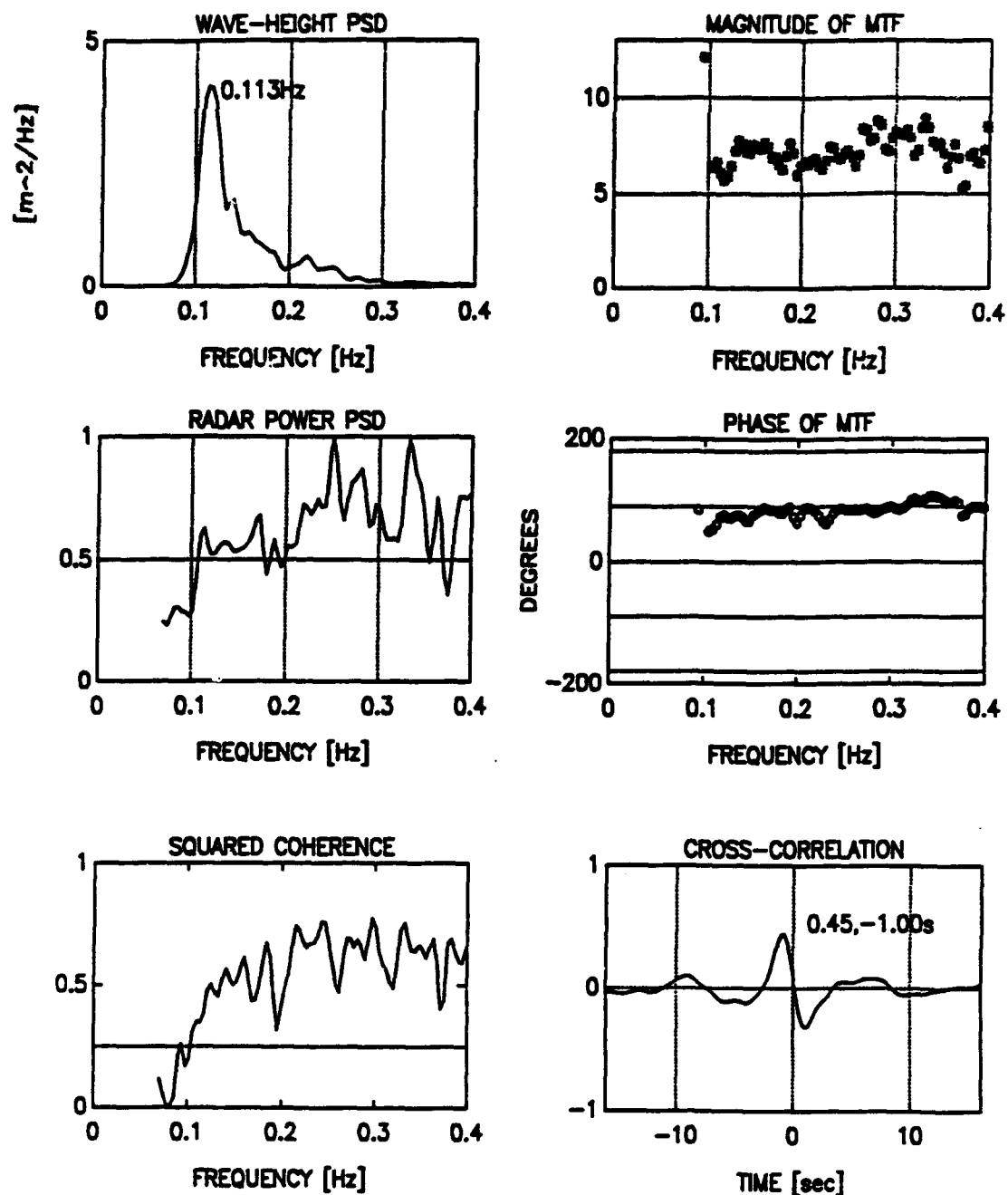


Figure 5.6 Simulated MTF run for HH polarization at incidence angle of 30° . The exponent of ripple spectrum is γ is -4.

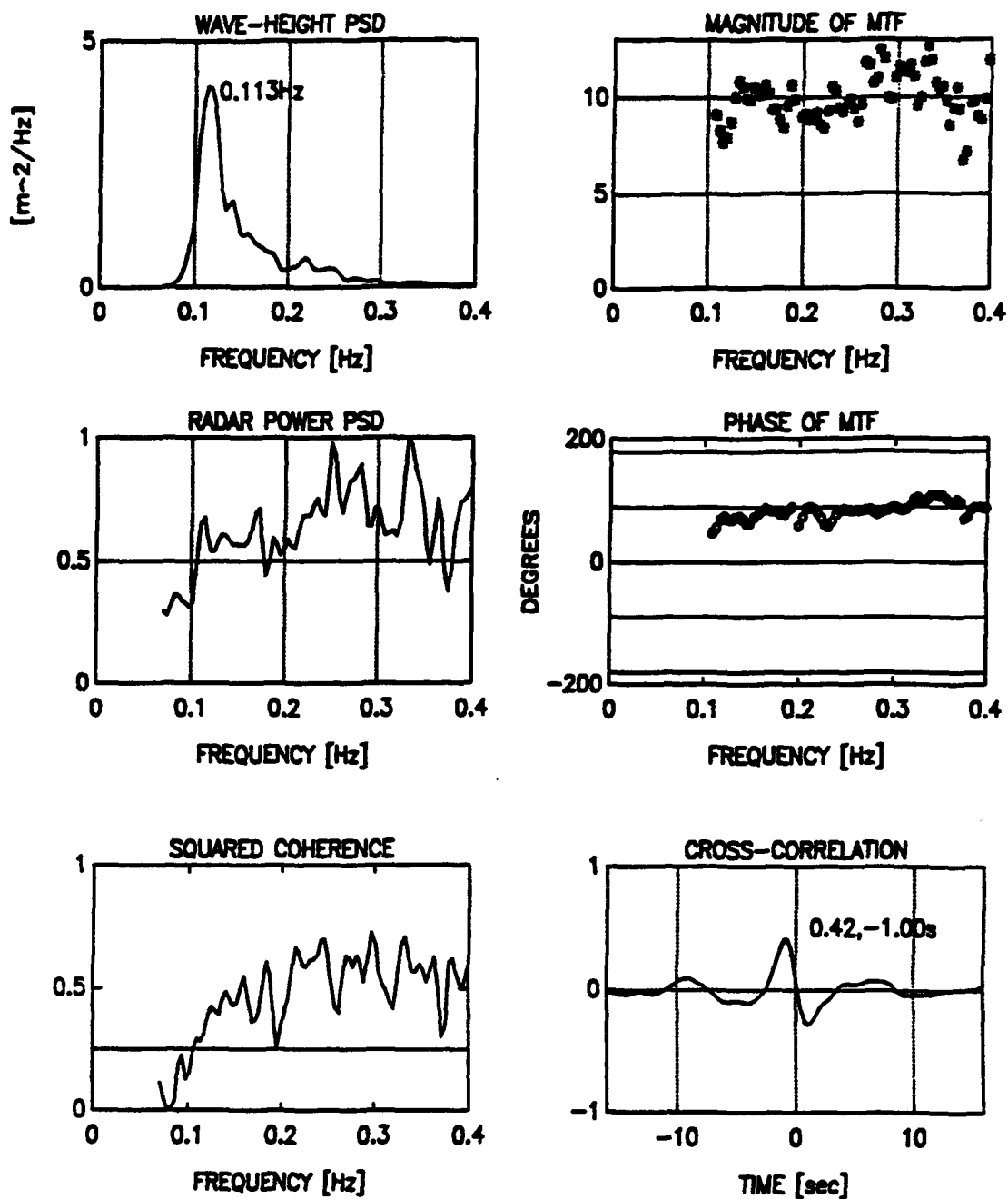


Figure 5.7 Simulated MTF run for VV polarization and at incidence angle of 30° .
The exponent of ripple spectrum is γ is -4.

series of the radar signal power using (12). In the figures, the waveheight spectrum is in the upper left corner. The peak of the waveheight spectrum is at 0.113 Hz. Below the waveheight spectrum is the simulated radar-signal spectrum. The rest of the plots show the result of fitting a linear transfer function to the data. The coherence function is always less than 0.75 and is about 0.5 near the dominant wave frequency. The cross-correlation function has a peak value of 0.45 at a lag of -1 seconds. With the dominant wave frequency of 0.113 Hz, the cross-correlation function predicts that the phase shift between the tilt modulation and waveheight time series is $360^\circ \times 0.113 = 40.7^\circ$. The first-order approximation predicts a phase shift of 90° . This clearly demonstrates the importance of nonlinearities. Note that the low values of cross correlation and coherence functions are entirely due to effects of nonlinearities.

Figures 5.8 and 5.9 show the effects of tilt nonlinearities on the magnitude and phase of the VV-polarized MTF at various incidence angles.. Figures 5.10 and 5.11 show the same set of plots for HH polarization. The peaks and valleys in both the magnitude and phase of MTF correspond to the fine structure of the waveheight spectrum. A direct result of nonlinearities is that the transfer function is a function of the input signal. The figures clearly show that the tilt nonlinearities significantly affect the phase of the modulation transfer function even at relatively high incidence angles.

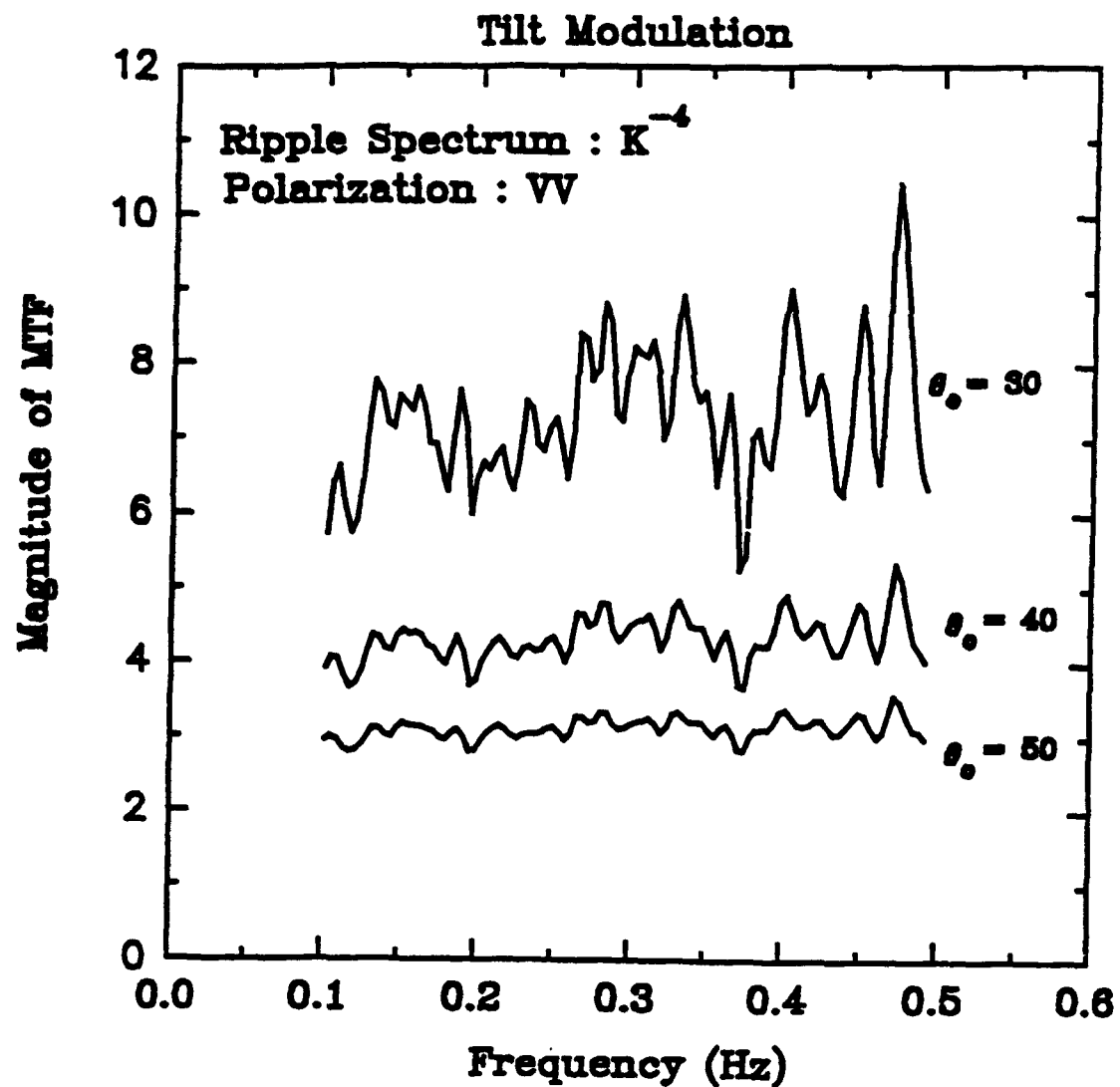


Figure 5.8 Dependence of magnitude of tilt MTF on incidence angle θ_0 for VV polarization and $\gamma = -4$.

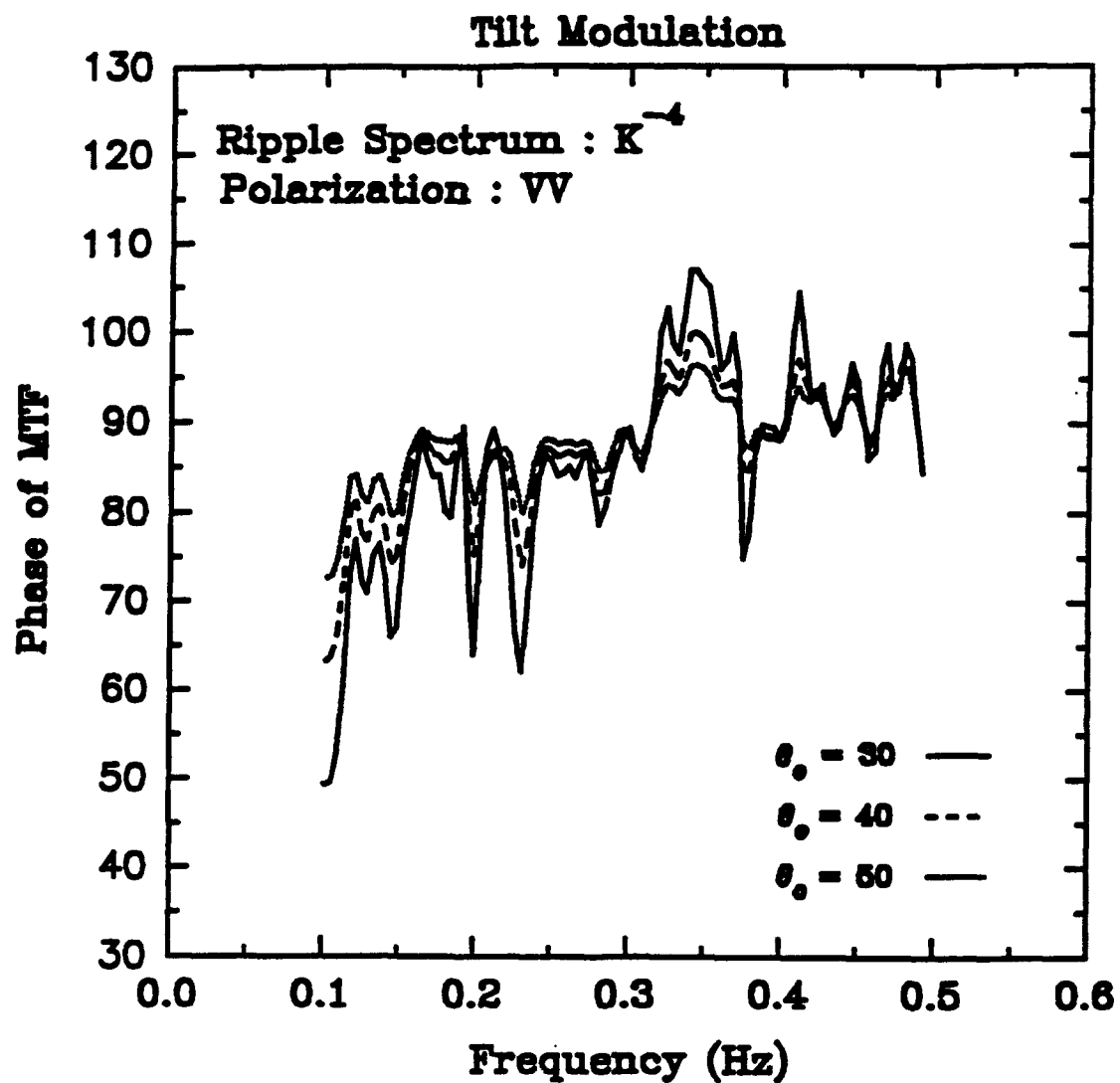


Figure 5.9 Dependence of phase of tilt MTF on incidence angle θ_0 for VV polarization and $\gamma = -4$.

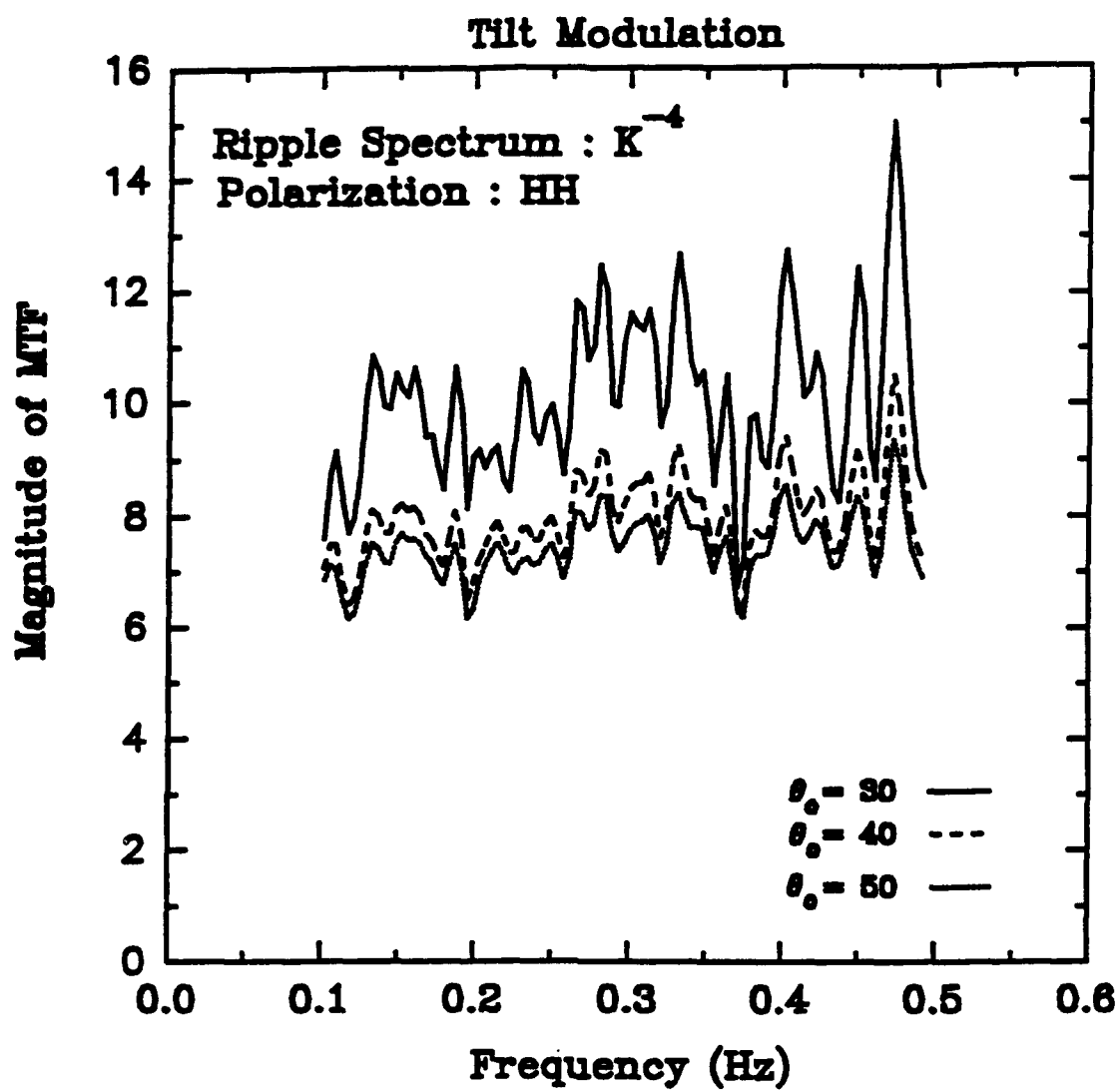


Figure 5.10 Dependence of magnitude of tilt MTF on incidence angle θ_0 for HH polarization and $\gamma = -4$.

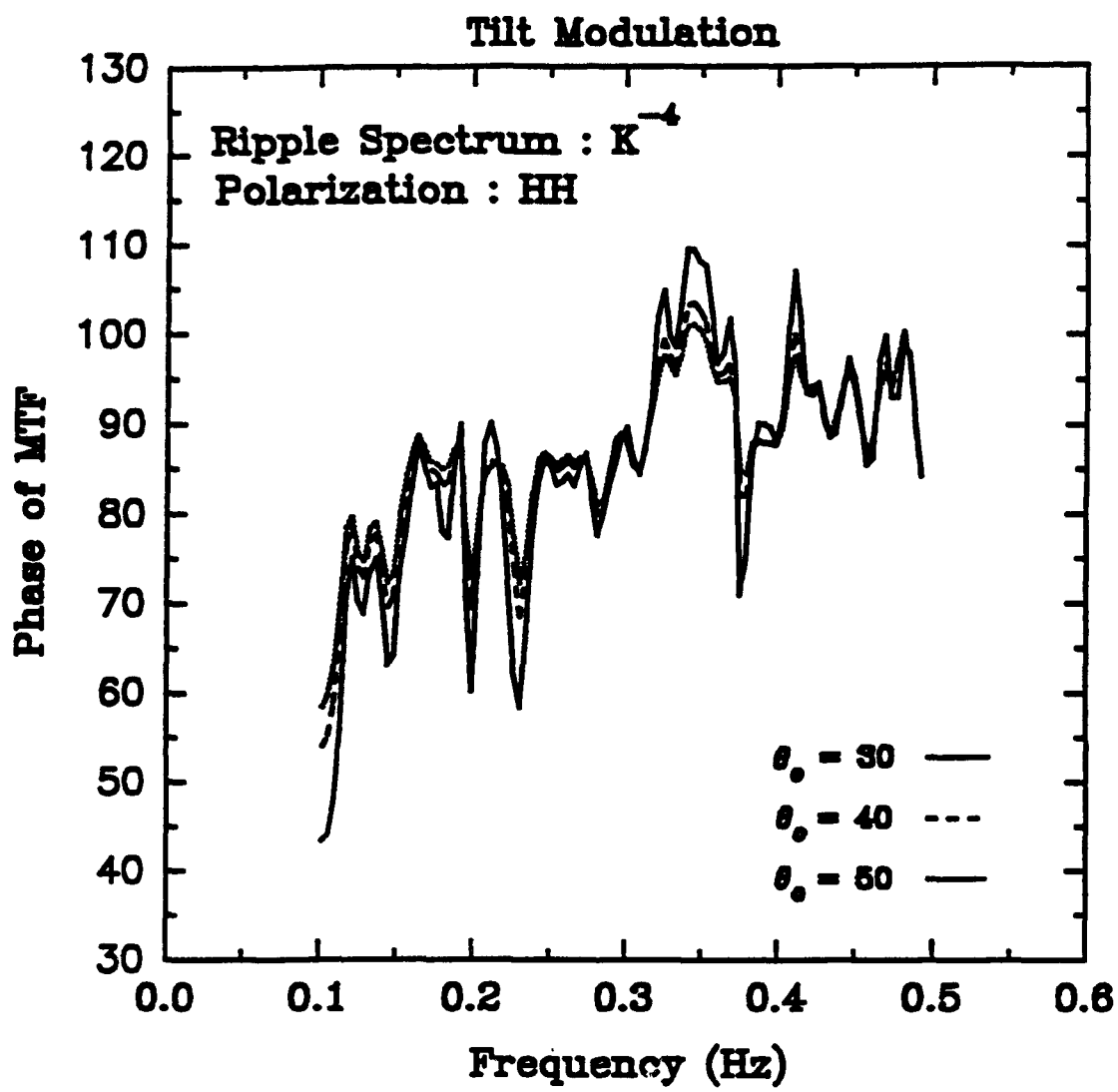


Figure 5.11 Dependence of phase of tilt MTF on incidence angle θ_o for HH polarization and $\gamma = -4$.

Coherence Function: An important quantity in analysis of this type is the coherence function (Bendat and Piersol, 1971). The total coherence between the return power and waveheight is

$$\gamma_{pw}^2(f) = \frac{|G_{pw}(f)|^2}{G_{pp}(f)G_{ww}(f)} \quad (37)$$

The quantity $1 - \gamma^2(f)$ can be thought of as a measure of the mean square value of the scattered power not accounted for by the height variations at frequency f (here we have assumed that the tilt and aero-hydrodynamic modulations are caused by long-wave slope variations). Values of coherence function less than one indicate either that the relation between long-wave heights and the scattered power is nonlinear or that the scattered-power modulation is due to sources other than long-wave slopes.

Referring to Figure 5.1, we find the tilt coherence function as

$$\gamma_t^2(f) = \frac{|G_{ps}(f)|^2}{G_{pp}(f)G_{ss}(f)} \quad (38)$$

Due to the nonlinear relationship between $p_T(t)$ and $s(t)$, the function $\gamma_t^2(f)$ is always less than one. Examples of the tilt coherence function were given in Figures 5.6 and 5.7.

Referring to Figure 5.1, we write the coherence function associated with the hydrodynamic transfer function as

$$\gamma_H^2(f) = \frac{|M_H(f)|^2 G_{ww}(f)}{G_{pp}(f)} \quad (39)$$

Therefore, to estimate the hydrodynamic coherence function one would first estimate $M_H(f)$, and then apply the above equation.

The tilt coherence function is calculated deterministically from the measured slopes, so it would be unity if nonlinear effects were absent. Thus, we may determine the values of the overall coherence after correcting for nonlinear effects due to slope. To do this we write

$$\gamma_{total}^2(f) = \frac{|G_{pw}(f)|^2}{G_{pp}(f)G_{ww}(f)} + (1 - \gamma_T^2) \quad (40)$$

5.8) Some experimental results

The procedure for extracting the hydrodynamic modulation form was described in section 5.5. Basically, we obtain the hydrodynamic contribution by dividing the total radar signal power by the computed tilt modulation contribution. Figure 4.9 of Chapter 4, shows a sample run with its single-point MTF at a wind speed of 12 m/s in the upwind direction with VV polarization and an angle of incidence of 45°. The radar-signal spectrum shows a distinct peak at the dominant long-wave frequency of 0.117 Hz. Figure 5.12 shows the phase and the magnitude

of the hydrodynamic transfer function of the same run. At the dominant-wave frequency, the hydrodynamic MTF is small compared to the total, so the slope effect is dominant. At higher frequencies, however, the hydrodynamic component becomes more important as it increases and the total decreases. The phase of hydrodynamic modulation is about 120° (maximum on the lower part of the forward face of the wave) at the dominant frequency, but it moves toward the middle of the forward face for higher-frequency waves (phase of 90°). Figure 5.13 compares the total and hydrodynamic coherence functions for the same run. The higher value of coherence at the dominant wave frequency suggests that much of the hydrodynamic modulation is related to the position on the long wave. At higher long-wave frequencies, it is related less to the position on the smaller waves.

Figure 5.14 shows the dependence of the magnitude and phase of the hydrodynamic modulation transfer function on wind speed for an upwind-upwave situation. Points represent the averages over long-wave frequencies of 0.1 to 0.35 and 3-m/s wind speed ranges. The magnitude shows an inverse dependence on wind speed while the phase is relatively independent of wind speed. Figure 5.15 shows the phase and magnitude of the slope MTF versus the wind speed. Both the magnitude and phase of slope MTF increase with wind speed. The phase of slope MTF is close to 50° at the lower wind speeds and increases to about 90° for higher wind speeds.

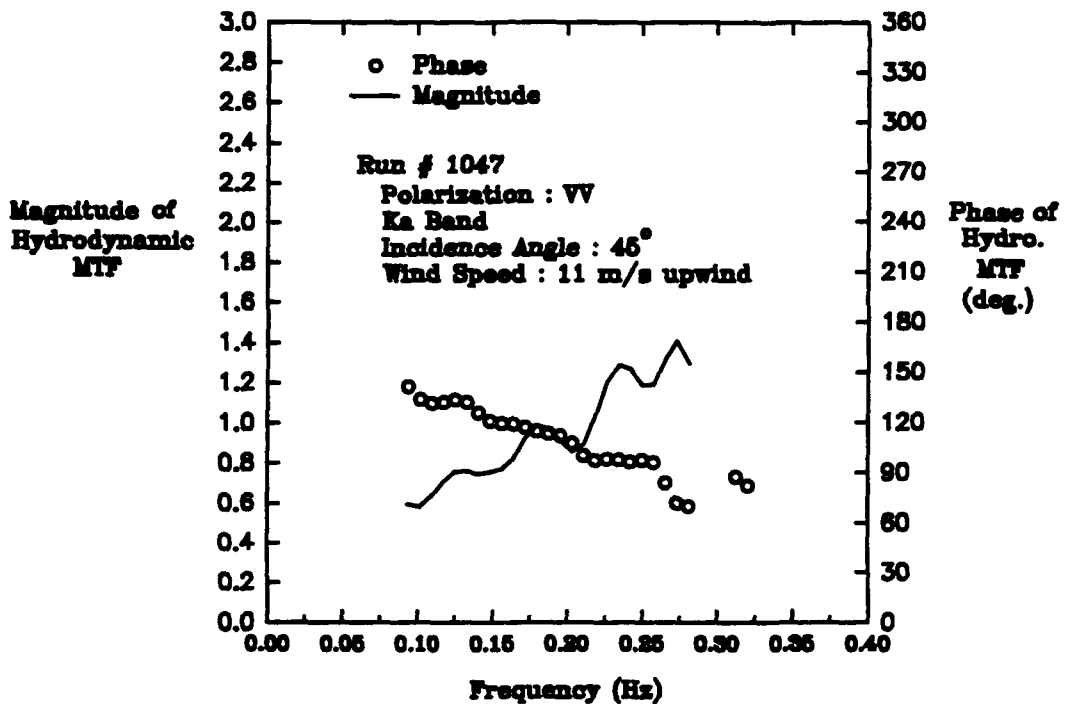


Figure 5.12 Magnitude and phase of hydrodynamic transfer function.

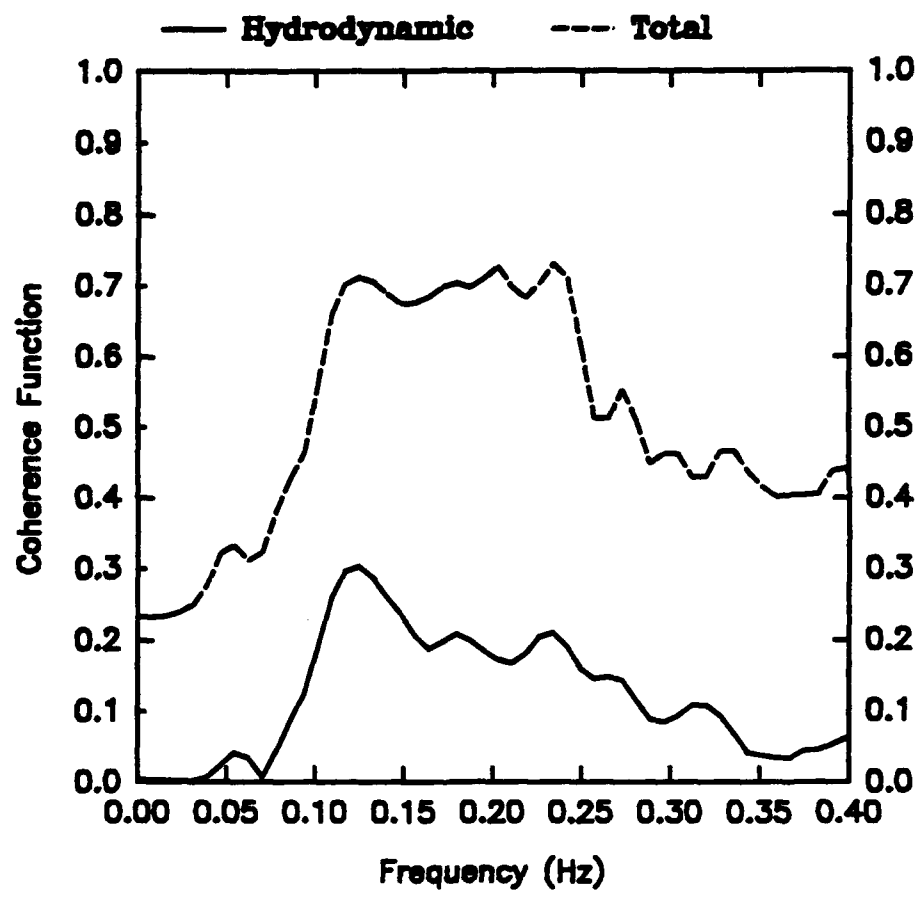


Figure 5.13 Total and hydrodynamic coherence functions.

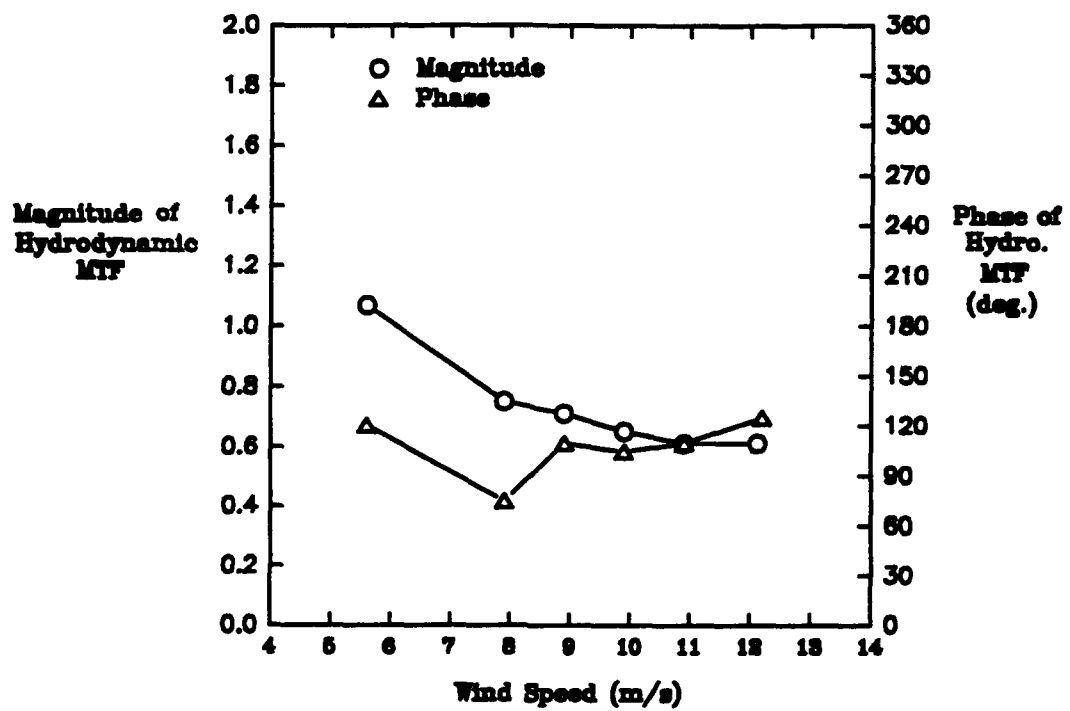


Figure 5.14 Dependence of the hydrodynamic modulation transfer function on wind speed.

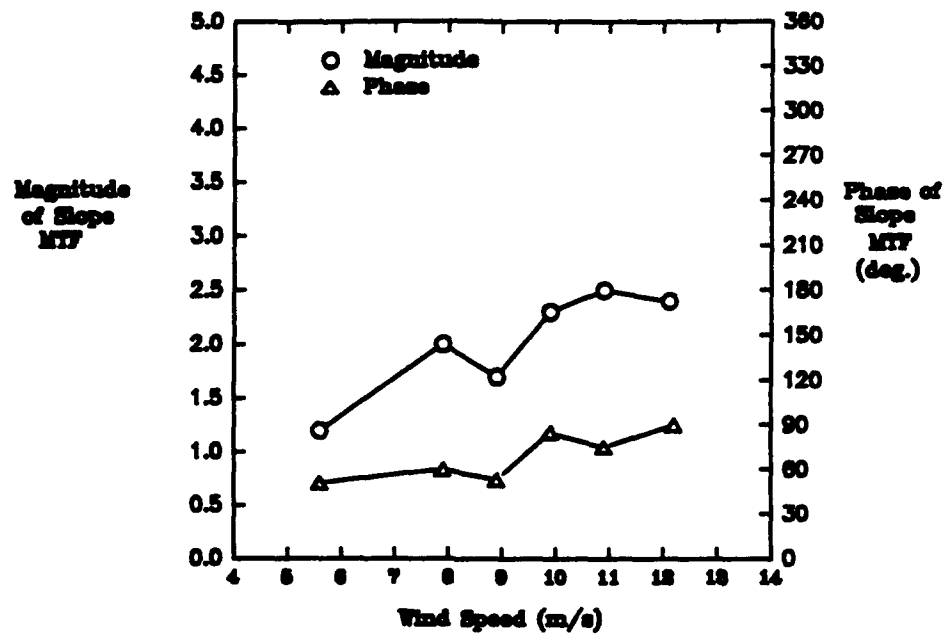


Figure 5.15 Magnitude and phase of slope MTF versus wind speed.

5.9) Conclusions

The radar returns to a scatterometer viewing the ocean surface are modulated by the passing large-scale waves. The modulation is due to tilting of the surface by large-scale waves (tilt modulation) and variations in ripple amplitude caused by the passing of the long waves. The VSG can measure two orthogonal components of the surface slopes. This new measurement capability allows separation of effects due to surface tilting from hydrodynamic effects caused by ripple-amplitude modulation. We have shown a procedure for separating the slope and hydrodynamic components of the radar modulation. For the examples shown, the hydrodynamic modulation is relatively small at the dominant frequency. At higher frequencies, it has more relative importance. The magnitude of the hydrodynamic modulation decreases with wind speed, while its phase is relatively independent of wind speed. Both the phase and magnitude of the slope MTF increase with wind speed.

Chapter 6

CONCLUSIONS AND RECOMMENDATIONS

6.1) Background

The brightness of high-resolution real- and synthetic-aperture radar images of the ocean surface correlates highly with the ocean surface profile. Cross-section variation is the primary source of brightness modulation for a real-aperture radar. The radar images are often assumed to be linearly modulated about the mean brightness by changes in backscatter associated with the large-scale waves. For synthetic-aperture radar systems the velocities of the water in the large-scale waves are also important in the image formation.

At moderate incidence angles, one often assumes that the microwave backscattering from the ocean surface is solely due to scattering from short surface ripples. This is commonly referred to as Bragg scattering. The passing of the large-scale waves modulate the radar cross section. Under a two-scale version of the Bragg theory, the radar cross section depends on the local angle of incidence, which changes with tilting of the ripples by the large-scale wave slopes, and with variations in Bragg ripple amplitude. The large-scale ocean waves change the local surface slope, and thus modify the Bragg-resonant condition. The scattering is, therefore, due to a different ripple, and its amplitude depends on its wavelength. This relation between long-wave slope and radar cross section is commonly referred to as the tilt modulation and can be modeled as a

memoryless nonlinear system. The hydrodynamic modulation results from a nonuniform distribution of the small-scale ripples of a given wavelength on the large-scale waves. For azimuthally traveling waves, the hydrodynamic modulation dominates, while for waves propagating in other directions both tilt and hydrodynamic modulation are significant.

Microwave scatterometers mounted on sea-based platforms show the most promise for measurement of hydrodynamic modulations. Previous methods for extracting the hydrodynamic modulation transfer functions from microwave measurements rely on three fundamental assumptions: a.) the ocean surface is a homogeneous and stationary surface that is represented by an ensemble of long-crested unidirectional waves that do not interact with each other and follow the linear wave theory, b.) first-order linear approximation of tilt modulation, as predicted by the Bragg theory, is valid, c.) the hydrodynamic and tilt modulation contributions to the total radar signal modulation are additive. Although, individually, an assumption may be satisfactory under specific circumstances, the collective use of these assumptions is questionable.

6.2) Vector slope gauge and its application

To address the limitations of these methods, we designed a Vector Slope Gauge (VSG) capable of measuring the instantaneous vector slope. Previous attempts at measuring the ocean surface profile involved the point measurements

of either wave height or velocity. Height or velocity (Doppler) measurements can be converted to slopes if one assumes long-crested linear waves. Since the VSG directly measures two orthogonal components of the surface, no assumptions regarding the linearity of the surface waves are needed.

The VSG uses switchable antenna beams to illuminate three closely spaced surface footprints. The beams are formed by a single parabolic dish antenna with switched feed. It has a beamwidth of roughly 2° . The beam switch at a 30 Hz rate and, therefore, the range is measured by each beam at a 10 Hz rate. The measured ranges are converted to heights. The three calculated height measurements are averaged to obtain the instantaneous height at the center of the three-beam footprint. Two orthogonal components of ocean slope are derived from the three range measurements. The instantaneous backscattered power is detected by a mean-square detector for each beam. The radar system operates at a frequency of 35GHz.

The hydrodynamic modulation accounts for changes in the ripple spectrum due to the passing of the large-scale waves. Under the two-scale Bragg theory, the tilt and hydrodynamic contributions to the total radar signal modulation are multiplicative. Yet previous attempts at separating hydrodynamic and tilt modulations assume an additive model (Alpers, 1981; Schroter, et al., 1986; Ocampo-Torres, et al., 1990). The relation between the long-wave slope and radar backscatter is nonlinear (Hesany, et al., 1985). Plant, et al. (1987) report

that both the measured MTF and the mean received power at X band are functions of the long-wave slope for near-neutral atmospheric conditions. They point out that the observed dependence can be partially explained by including the second-order effects of the long-wave slope.

Simultaneous measurements of the surface slope and radar cross section permit determination of the relative contribution of slope modulation to the overall fluctuation of the radar signal without resorting to first-order approximations. The hydrodynamic contribution is obtained by dividing the total radar signal power by the computed tilt modulation contribution. The procedure, outlined in Chapter 5, accounts for both the nonlinear relation between the vector slope and the radar backscatter and the multiplicative nature of the tilt and hydrodynamic contributions.

6.3) Measurements of MTF

During the SAXON-FPN experiment, we used the VSG data to compute VV-polarized Ka-band MTFs. For upwind-upwave cases, the magnitude of the total MTF decreases monotonically with increasing long-wave frequency, while the phase is relatively independent of the long-wave frequency. This inverse relation of the magnitude of the MTF to the long-wave frequency is consistent with previously reported measurements at C, X and Ku bands. Yet this dependence is contrary to theoretical predictions of both the tilt and the

hydrodynamic modulations. The models of the short-wave modulation predict an increase in hydrodynamic modulation with increasing long-wave frequency (Phillips, 1981; Alpers and Hasselmann, 1978). Under the two-scale model, the tilt modulation is almost independent of the long-wave frequency at mid-incidence angles.

The magnitude of the Ka-band MTFs shows a distinct inverse relation to the wind speed. The definition of MTF requires its normalization by average power. The average power is a strong function of wind speed and increases with increasing wind speed.

We used the procedure outlined in Chapter 5 to calculate the hydrodynamic transfer functions from the VSG data. The procedure was applied to a few upwind-upwave cases over a range of wind speeds. The results indicate that the phase of the hydrodynamic modulation is relatively insensitive to wind speed and the maximum of the hydrodynamic modulation occurs on the front face of the dominant wave near the position of maximum slope. The phase of the hydrodynamic transfer function decreases with long-wave frequency. The magnitude of the measured hydrodynamic transfer function shows little dependence on the wind speed and increases with increasing long-wave frequency.

We compared our measured results with the hydrodynamic theories of Alpers and Hasselmann (1978) and Phillips (1981). The observed dependence of both and magnitude and phase of the measured hydrodynamic modulation transfer

functions on long-wave frequency are consistent with the predictions of the theory. The phase of the hydrodynamic modulation, as predicated by theory, depends on an unknown quantity called the "relaxation time." For relaxation times approaching infinity, the short ripples are concentrated at the crest of the long-waves. Otherwise, the theory predicts a positive phase shift between the maximum of short-wave energy and the long-wave crest.

The phase of our measured hydrodynamic modulation transfer function shows no dependence on wind speed. Although this may indicate that the relaxation time of Ka-band ripples (wavelength about 0.5 cm) is independent of wind speed, this is by no means conclusive. The hydrodynamic modulation of the short ripples is complex and incompletely understood. The current hydrodynamic theories depend on many simplifying assumptions that limit their applications to only smooth surfaces with the ripples traveling in the same direction as the long-waves. Second-order effects, such as interactions between short ripples, and short-wave breaking, are also not included in these models (Alpers, 1981). Some higher order effects, such as modulations due to wind turbulence associated with the long-wave profile, may be particularly important at Ka band where the Bragg ripples are of the order of 0.5 cm (Findent, et al., 1986).

6.4) Recommendations

During a planned future experiment, the VSG will be operated along with a microwave scatterometer. It is important that the scatterometer provide simultaneous measurements of the cross section at both VV and HH polarizations. According to the two-scale Bragg model, the polarization ratio, $\sigma_{VV}^o / \sigma_{HH}^o$, is a function of only the orthogonal components of long-wave slope and the local angle of incidence. In other words, the polarization ratio is independent of the wind speed and direction, ripple spectrum, and other environmental factors. Simultaneous measurements of orthogonal components of slope allow calculation of the time series of the polarization ratio, which can then be compared to the actual polarization ratios measured by the scatterometer. This allows one to determine the range of the validity of the two-scale model under various environmental conditions. Moreover, the hydrodynamic transfer function derived simultaneously from VV and HH cross sections should be identical. This can then be used to validate the procedure used to derive the hydrodynamic transfer functions.

One possible improvement of the VSG system is to process the IF signal digitally. Since the IF spectrum is centered around 455 KHz, I&Q processing is not needed. A single-channel A/D board with a sampling rate of 2 MHz, accompanied with a DSP board for real-time FFT processing, will be adequate. This allows extracting the Doppler information by comparing the IF spectrum

during the up and down sweeps of the RF modulating triangular wave. The main advantage of this scheme is that the VSG can then measure three components of the surface velocity in conjunction with slope and height measurements. This permits comparison of slopes obtained from Doppler measurements with waveheight and slope measured directly. The relation between slope, height, and orbital velocity of the surface is presumably well understood for long-crested waves traveling in the range direction. However, for azimuth-traveling waves or situations where multiple wave trains exist, the relation between these surface parameters is not well established.

Proper calibration of the VSG system is difficult. Ideally, one would like to perform the calibration in the field, preferably before and after the actual data-gathering period. One possible arrangement would be to place the VSG antenna on a mount that would allow it to be moved independently in either azimuthal or vertical directions. With the antenna at a fixed azimuth angle, one varies the incidence angle in small increments over a small range, say, from 40° to 50° in increments of 2°. For each increment, the incidence angle is recorded along with the mean range corresponding to each antenna beam. The same procedure is then repeated by sweeping the antenna in azimuth while keeping the incidence angle fixed. In Chapter 3, we showed that the slope in each direction is the ratio of the weighted sum of the products of the three range measurements. With a proper set of calibration values, one can then invert these equations and

solve for the unknown constants that depend only on the antenna geometry. This procedure can be performed in the field before and after the actual experiment. One advantage of this calibration method is that it accounts for the finite beamwidth of each antenna beam.

In summary, the VSG is a viable tool for determining the range of validity of some of the proposed microwave backscattering models of the ocean. The VSG can measure orthogonal components of slopes of ocean waves. This is necessary if one is to obtain a proper measure of relation between radar backscatter and the ocean surface profile. As a stand-alone system, the VSG can be used to obtain the directional spectrum of the long waves, and various statistics of the ocean surface.

Appendix A

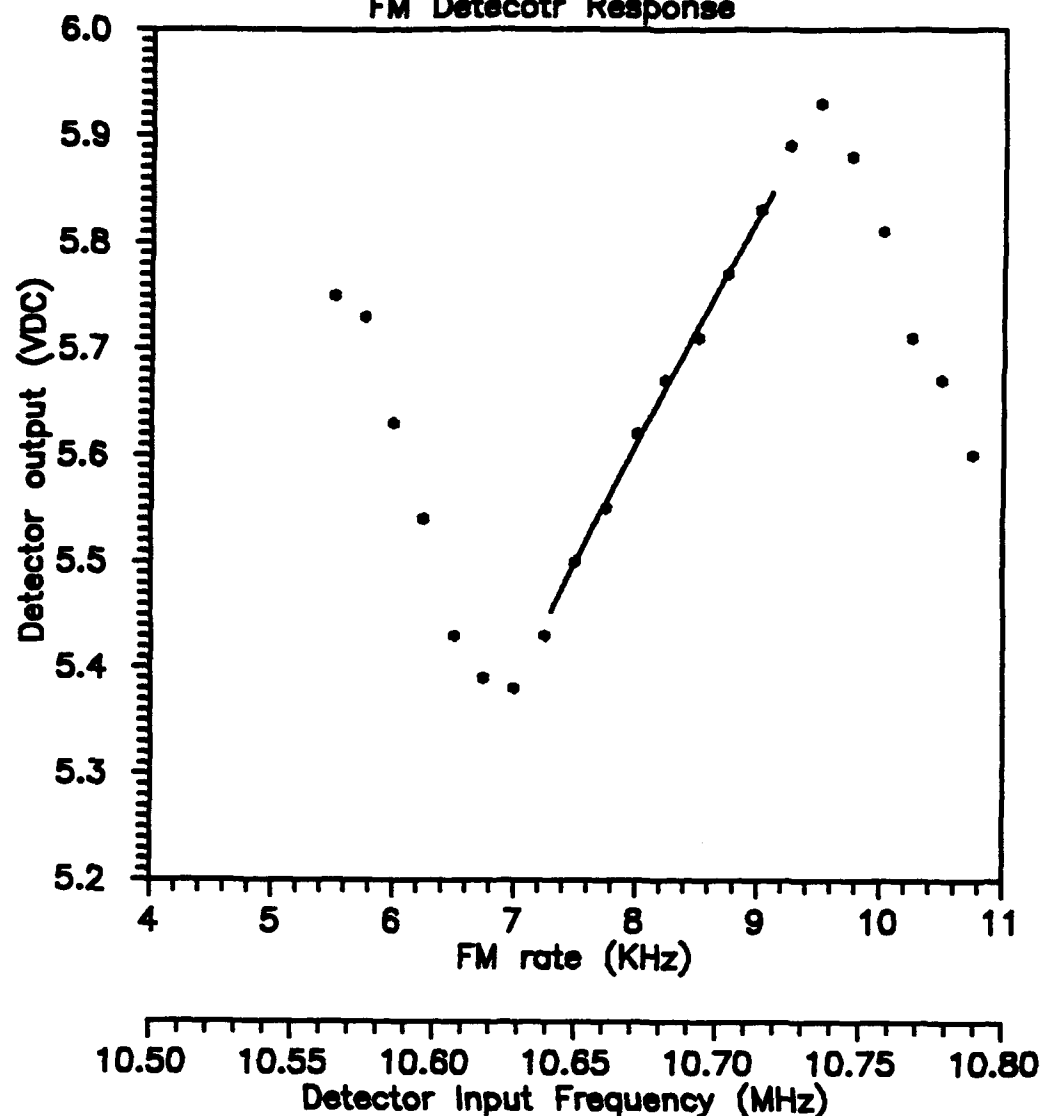
**THE VECTOR SLOPE GAUGE HARDWARE
DOCUMENTATION**

Table A1. VSG antenna pin assignment

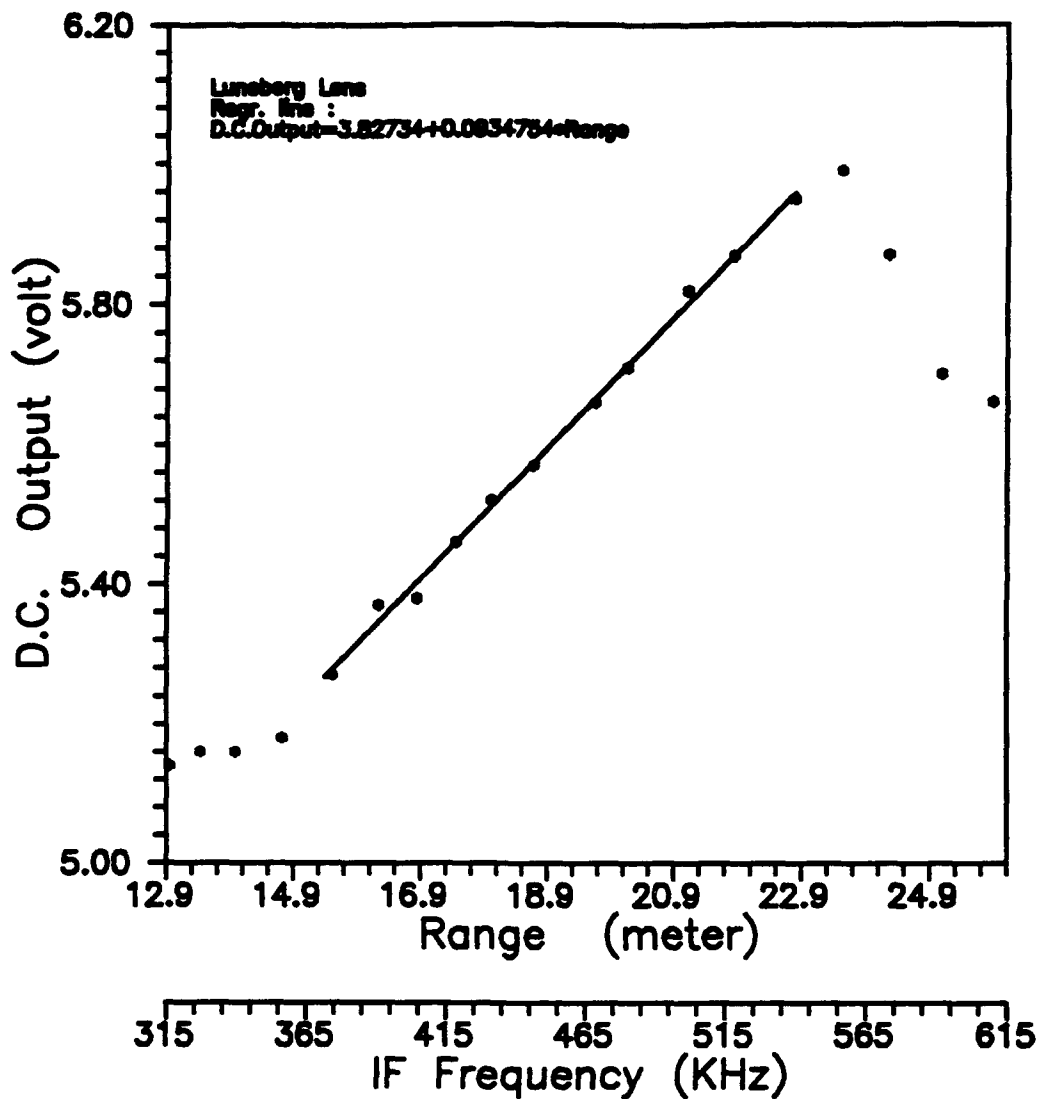
PIN number	Voltage assignment	Switch #
1	$15 \pm 0.1\text{V DC}$	Switch 1 (S ₁)
2	$5.2 \pm 0.2\text{V DC}$	
3	Ground	
4	Trigger CW	
5	Trigger CCW	
6	$15 \pm 0.1\text{V DC}$	Switch 2 (S ₂)
7	$5.2 \pm 0.2\text{V DC}$	
8	Ground	
9	Trigger CW	
10	Trigger CCW	
11	$15 \pm 0.1\text{V DC}$	Switch 3 (S ₃)
12	$5.2 \pm 0.2\text{V DC}$	
13	Ground	
14	Trigger CW	
15	Trigger CCW	

Table shows the pin assignment for the 15 pin connector that drives the antenna switching circuitry.

FM Detecotr Response



VSG Range Calibration



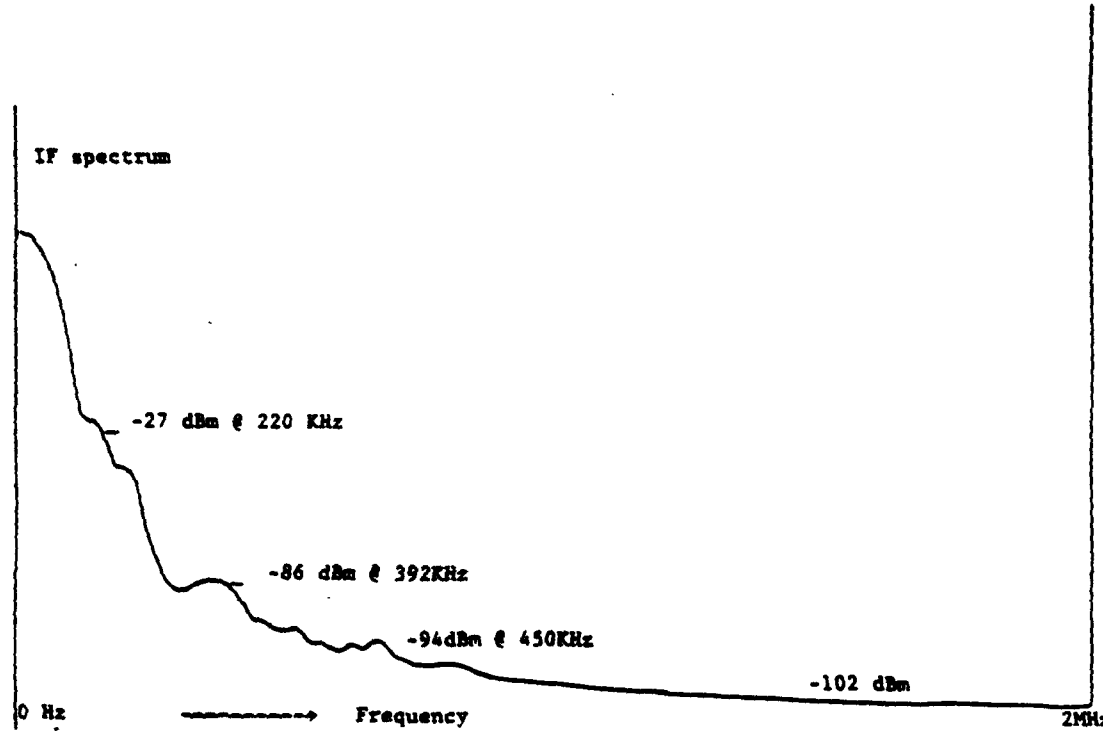


Figure shows the noise floor of the receiver at the first IF. The receiving antenna was covered with microwave absorbing material. At 455 kHz, the sidelobes are less than -90 dBm.

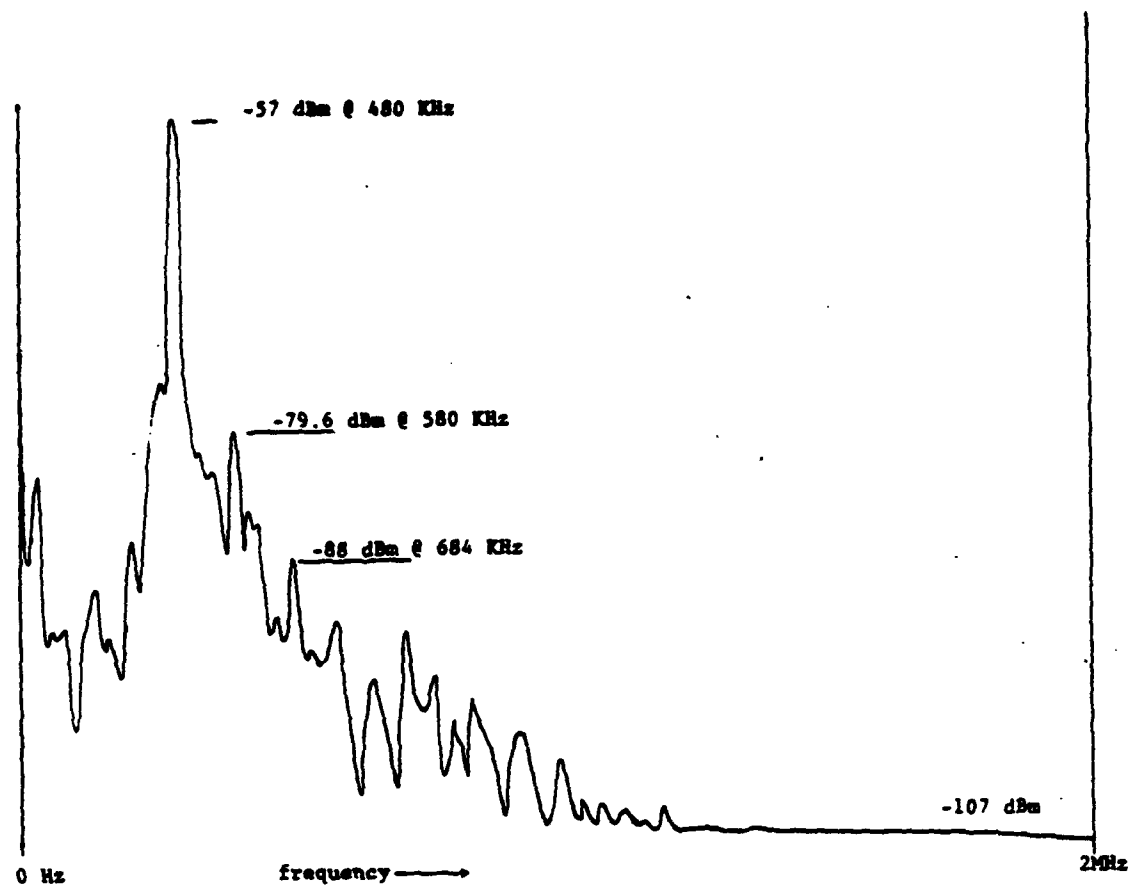


Figure shows an example of the IF spectrum during a delay line measurement.

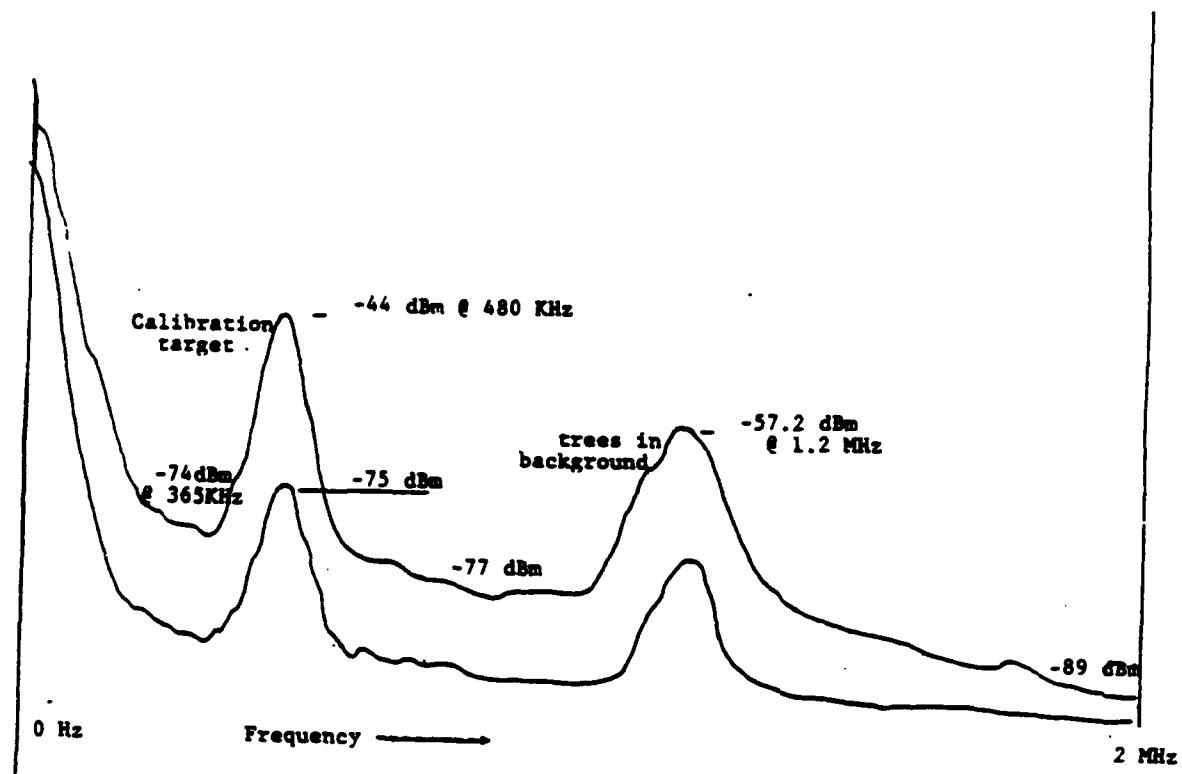
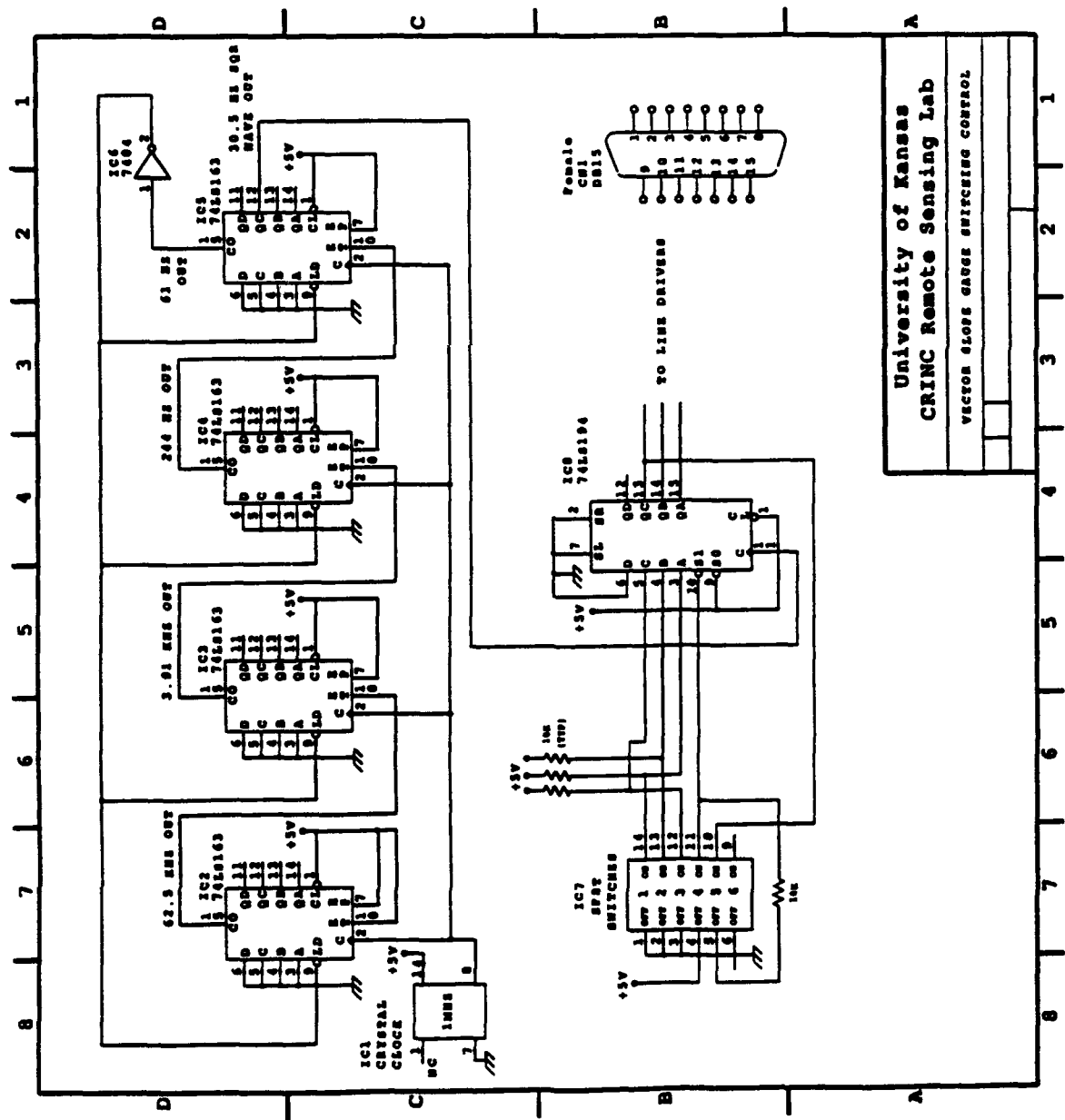
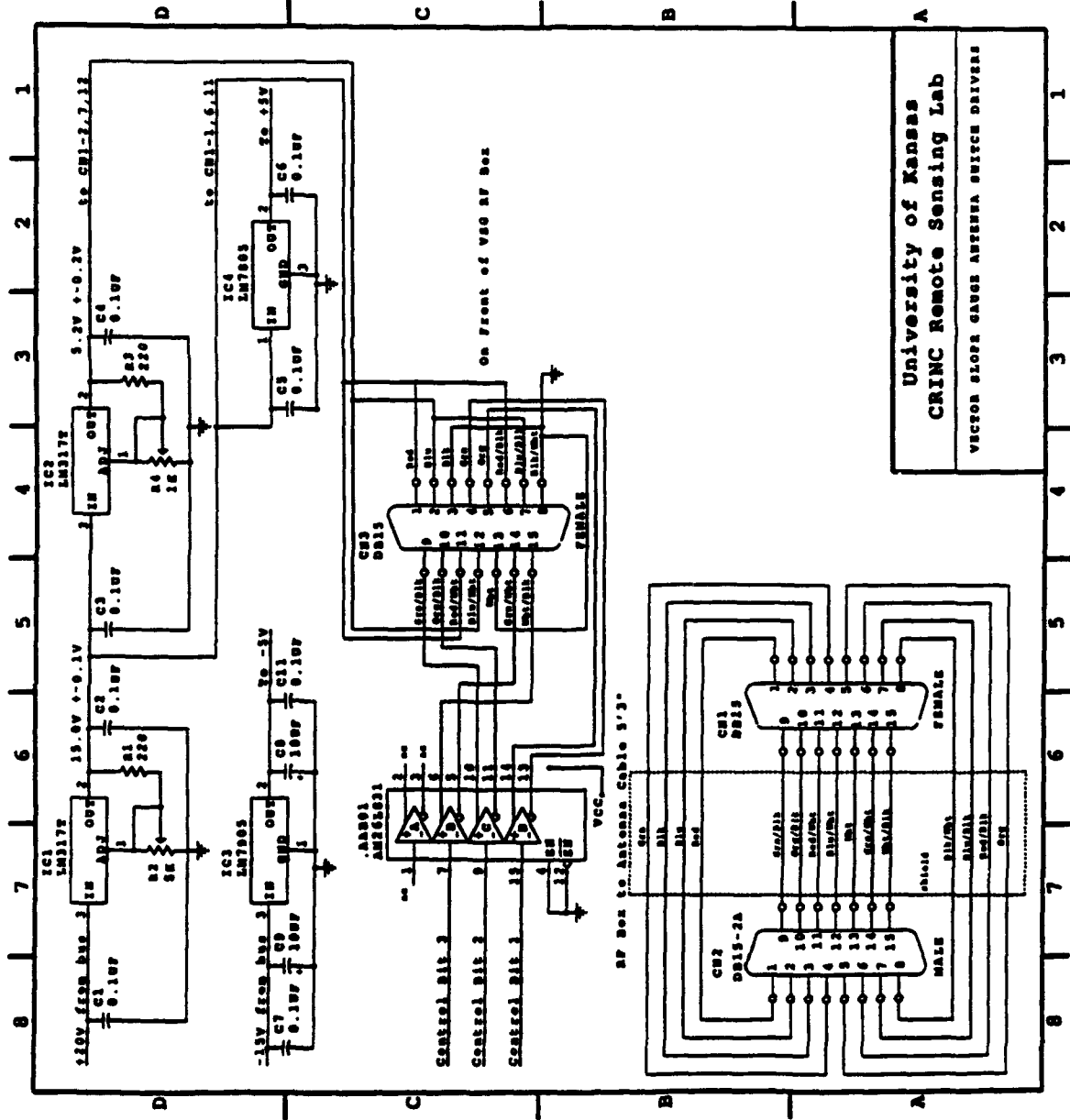
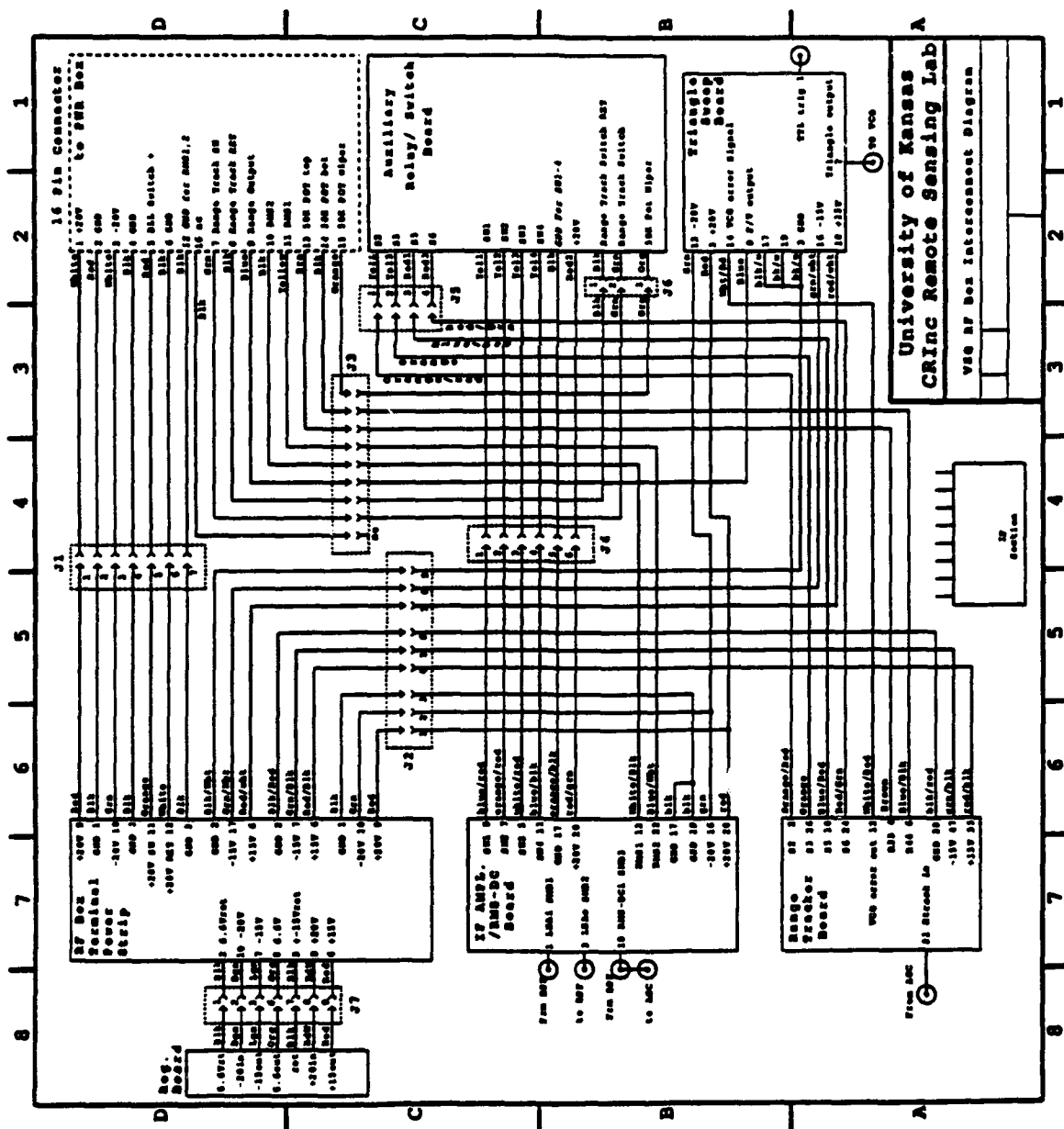


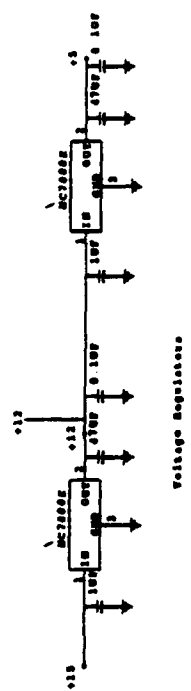
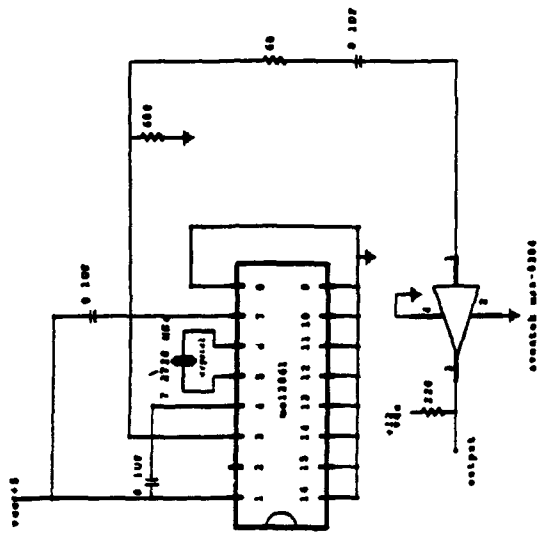
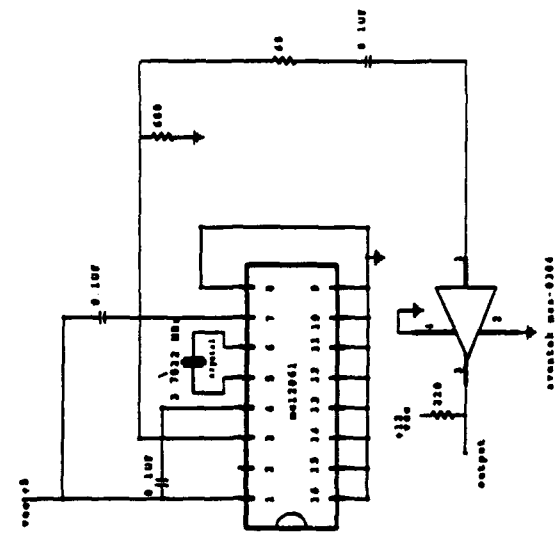
Figure shows an example of radar return from 8" sphere. The signal at 1.2 MHz is due to the bushes in the background. The lower trace is the return when the transmitter power amplifier was replaced with a short.



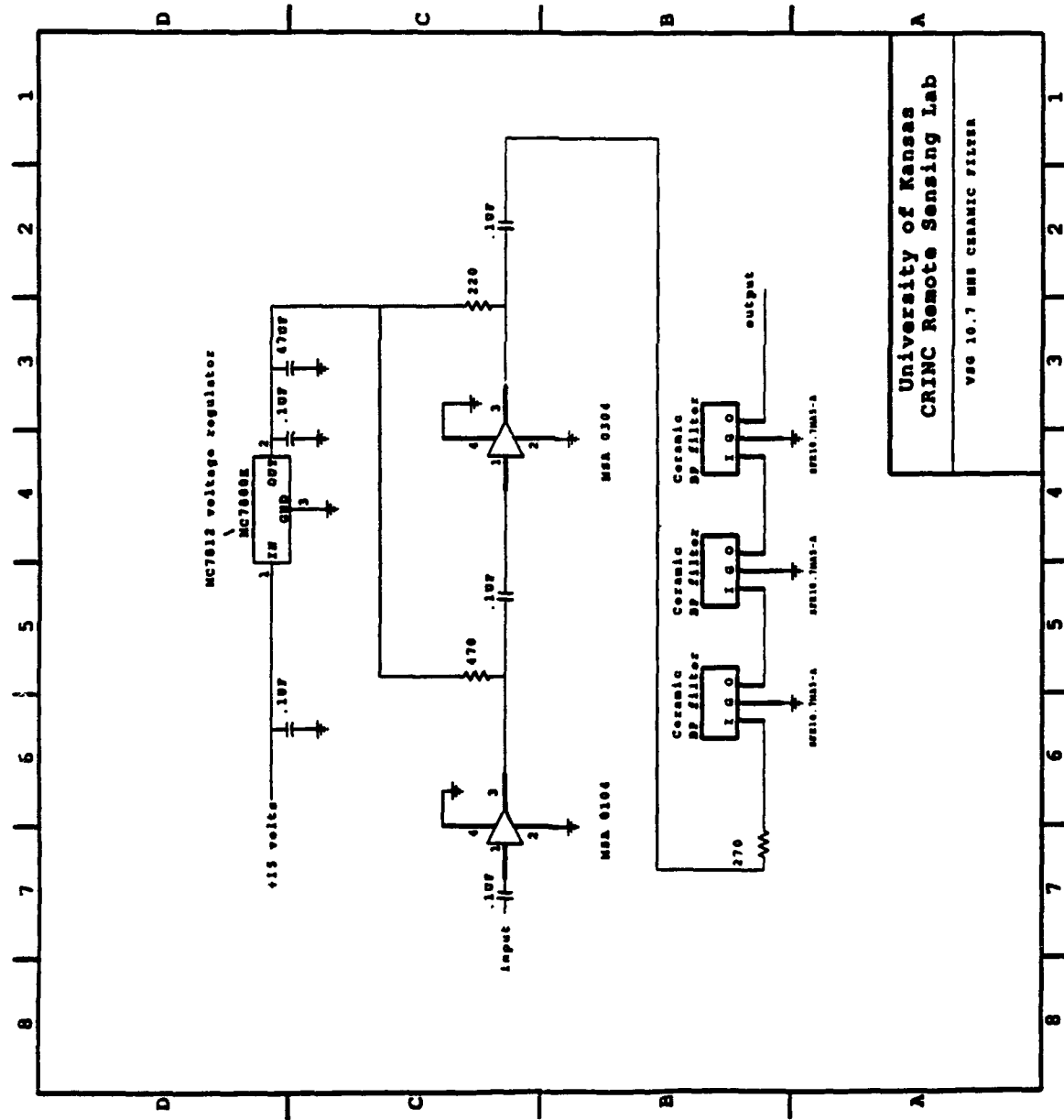




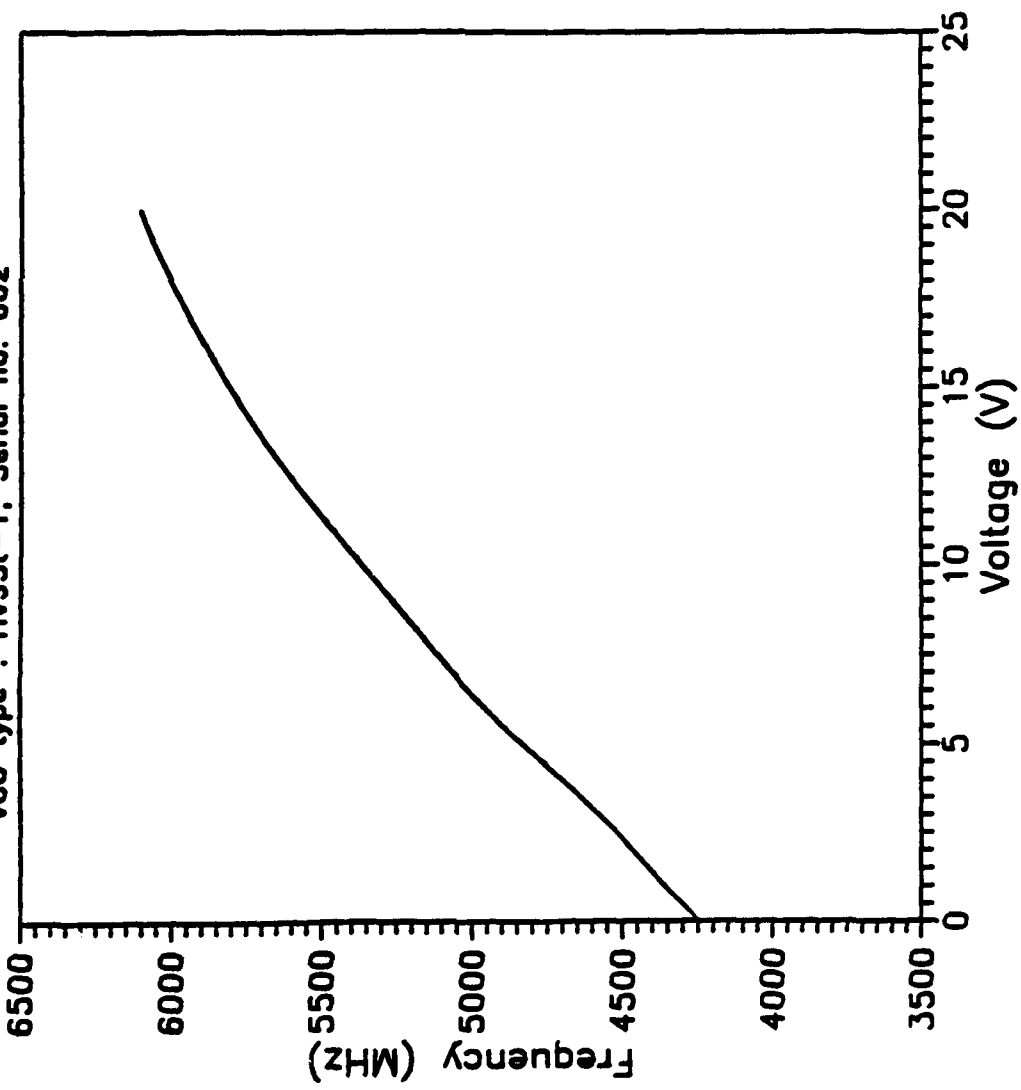
KU - REMOTE SENSING LAB.
VSG IF OSCILLATORS



Voltage Regulator.

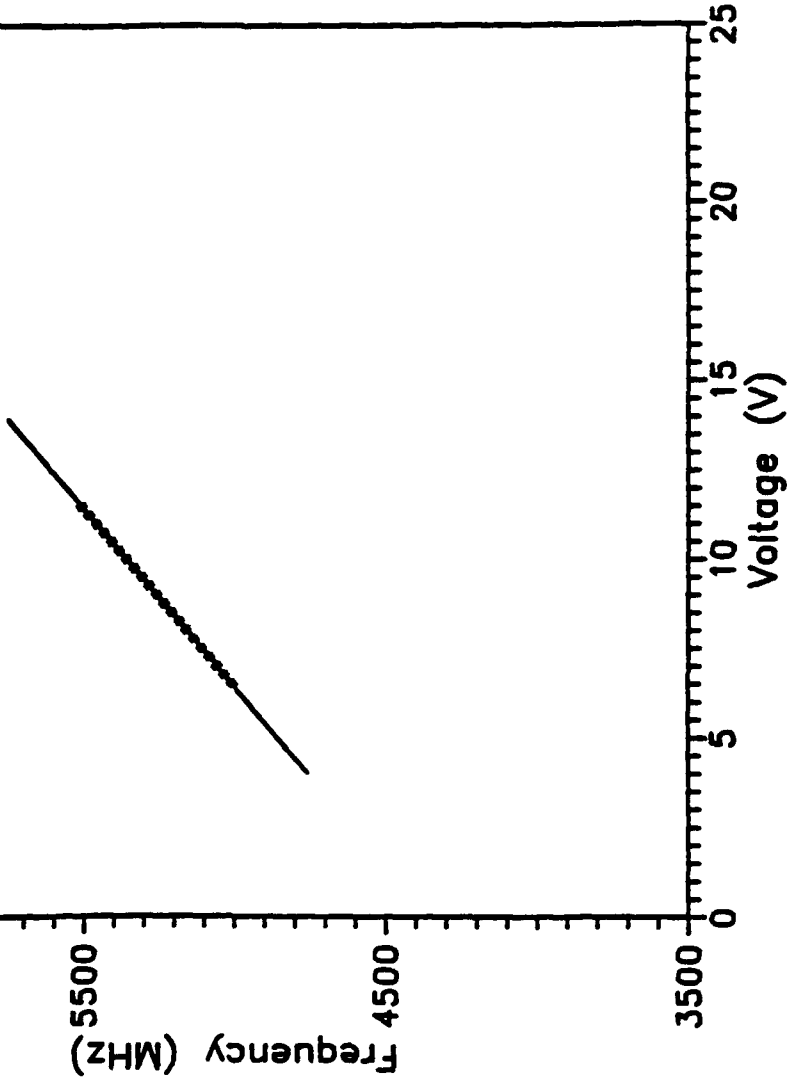


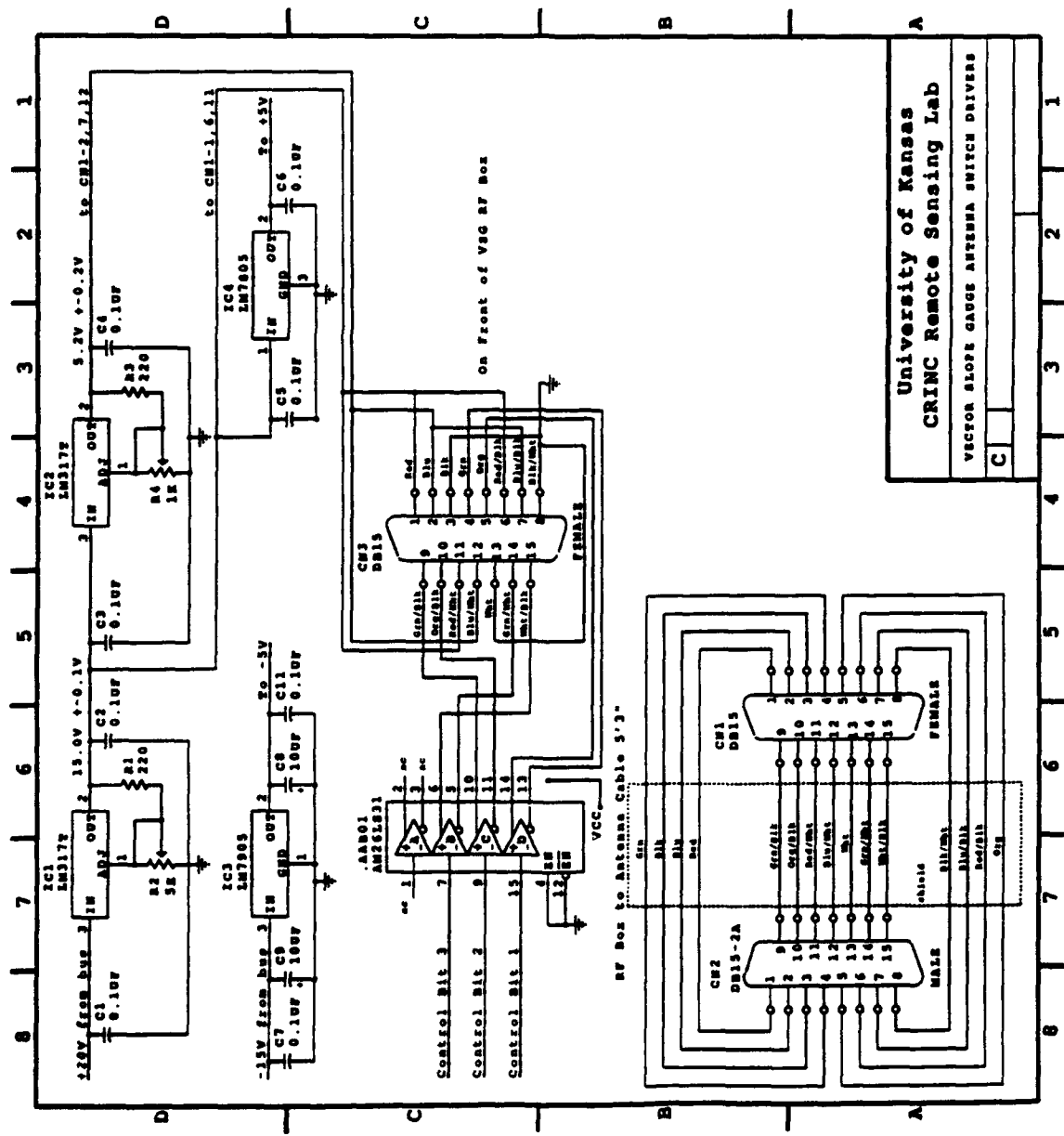
MAGNUM MICROWAVE - VCO TEST DATA
VCO type : HV931-1, Serial no. 002

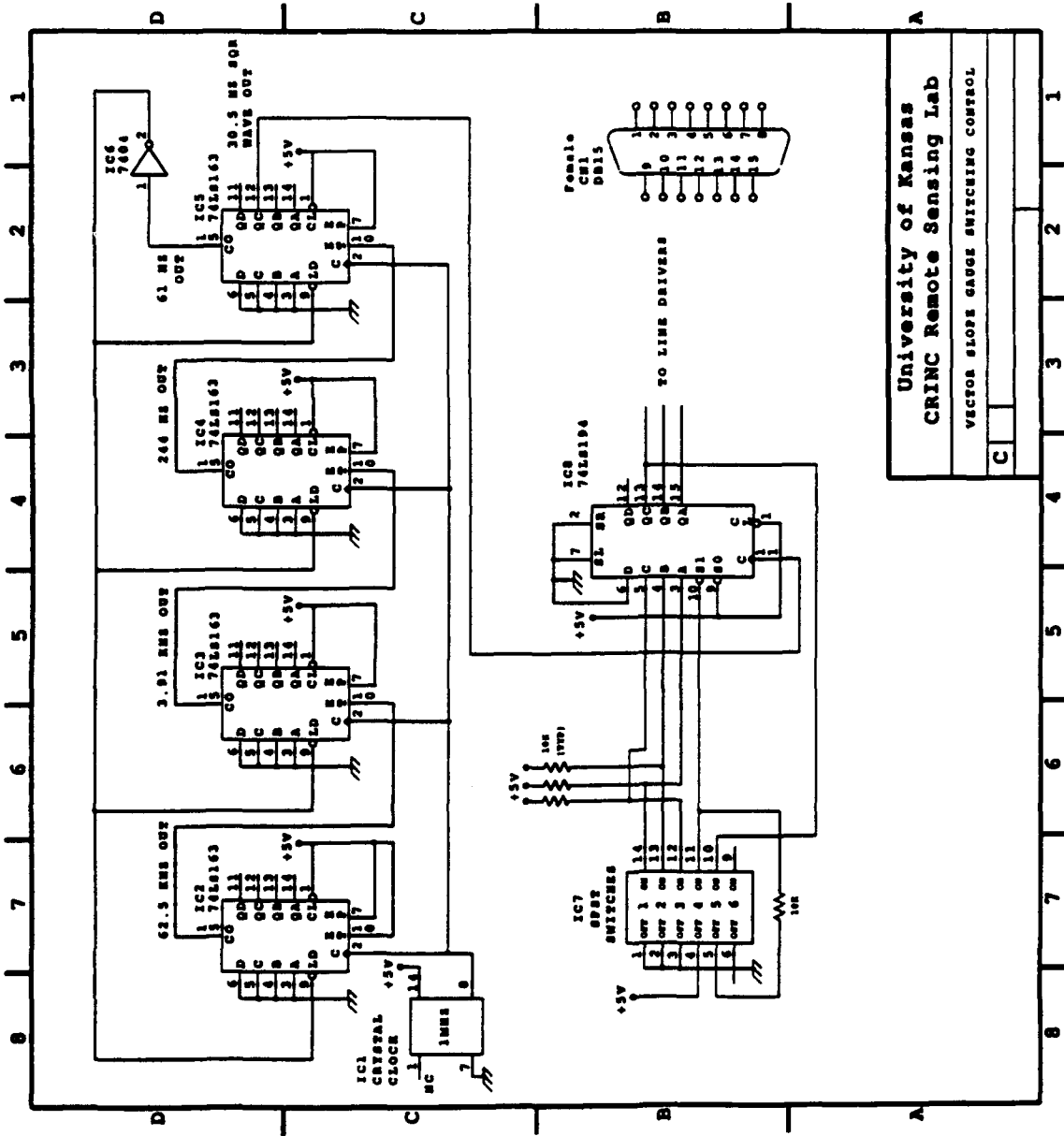


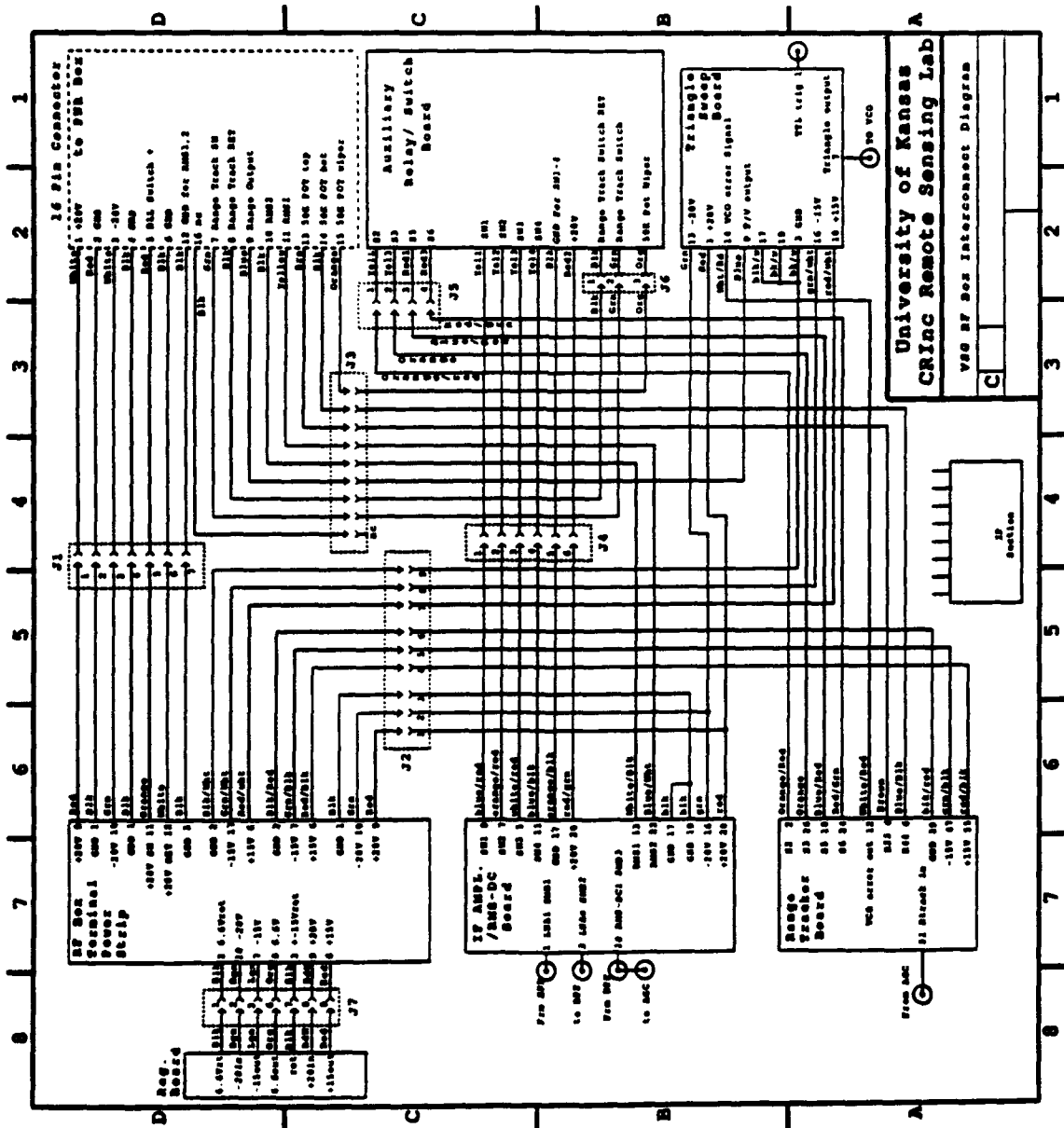
MAGNUM MICROWAVE - VCO TEST DATA
VCO type : HV931-1. Serial no. 002

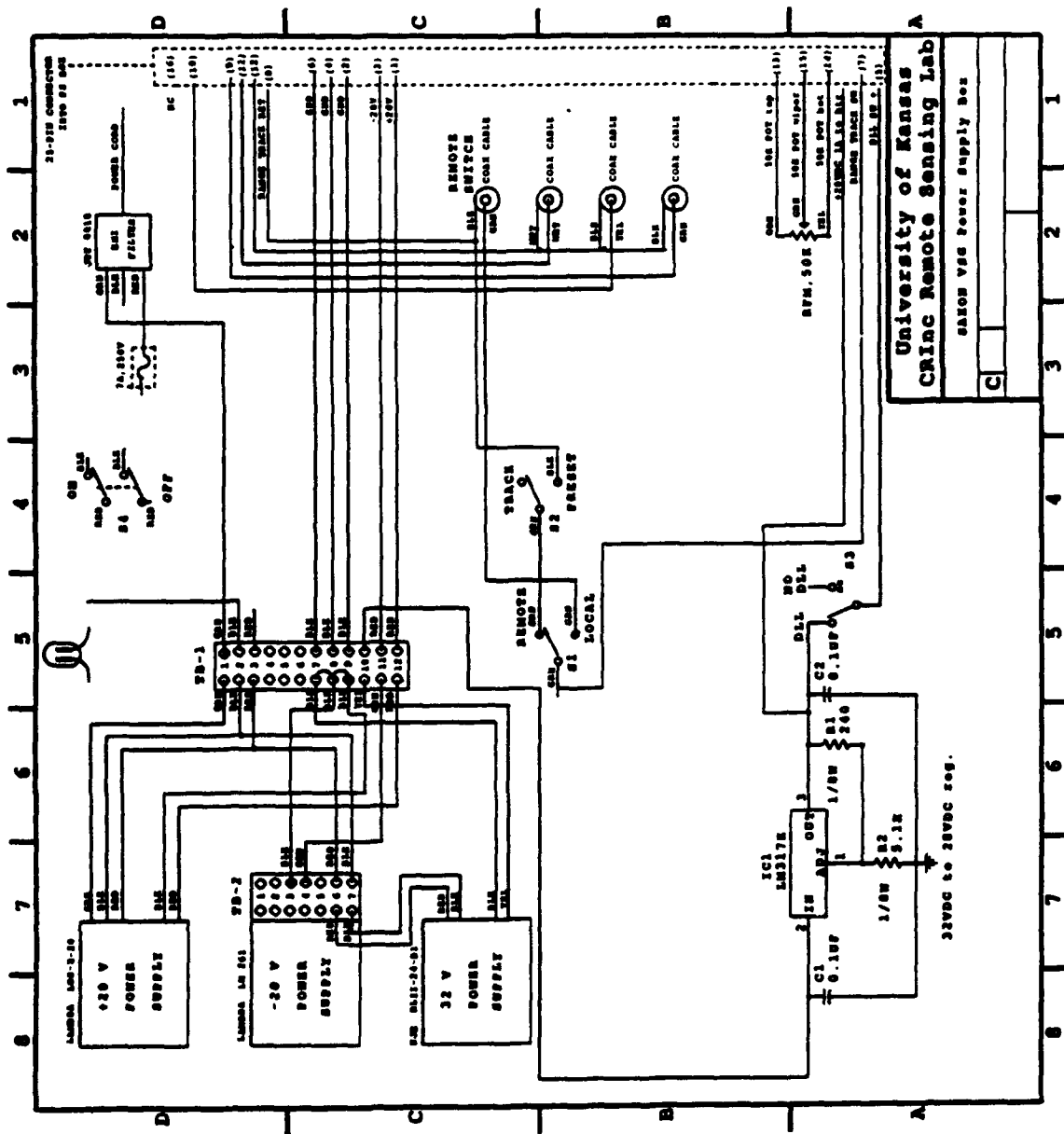
Req. Line : freq.(MHz) = $100.102 \times \text{Voltage(V)} + 4358.4$
Voltage Range: 9.50 - 11.50 (V)
Freq. Range : 5006.10 - 5509.30 (MHz)

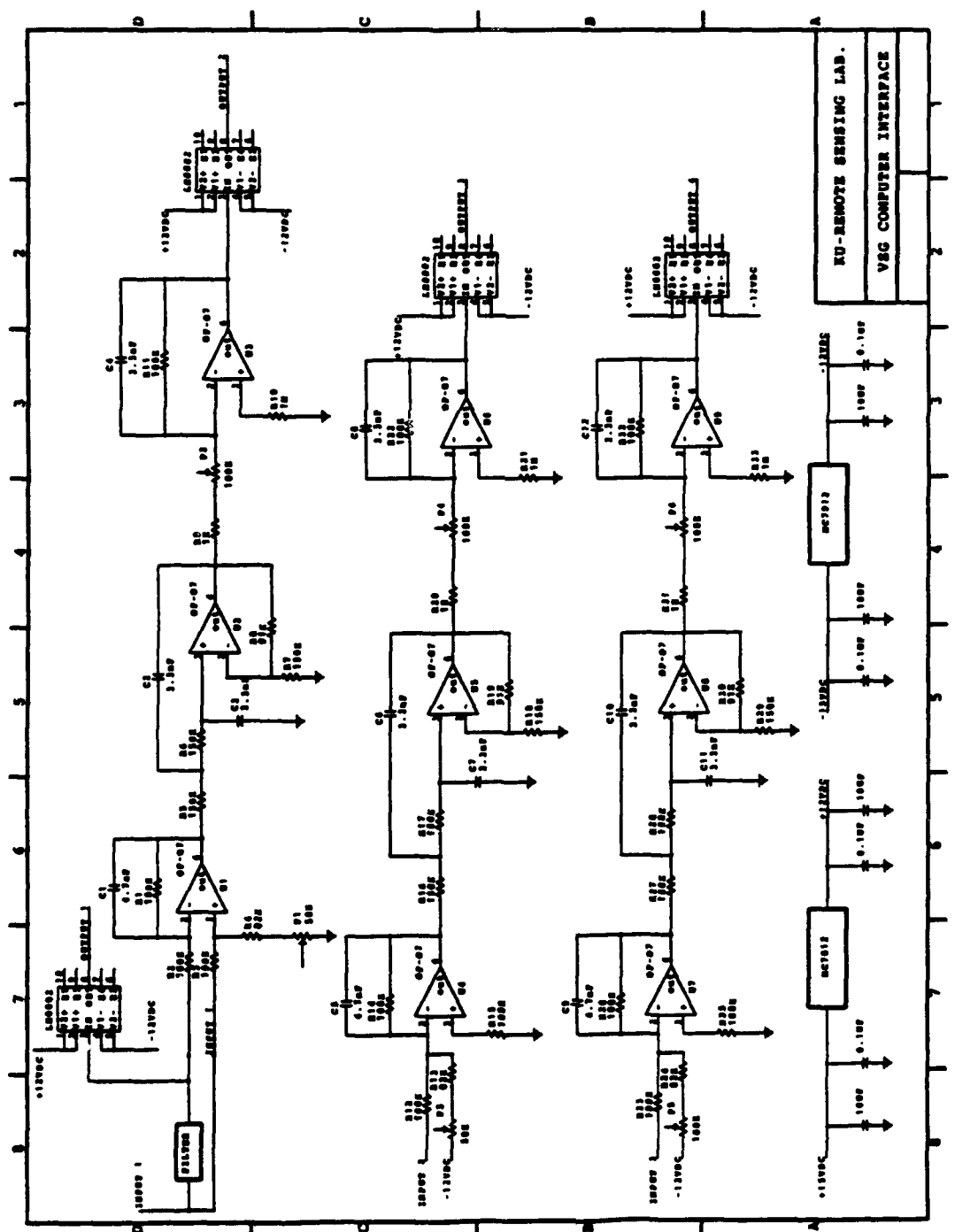


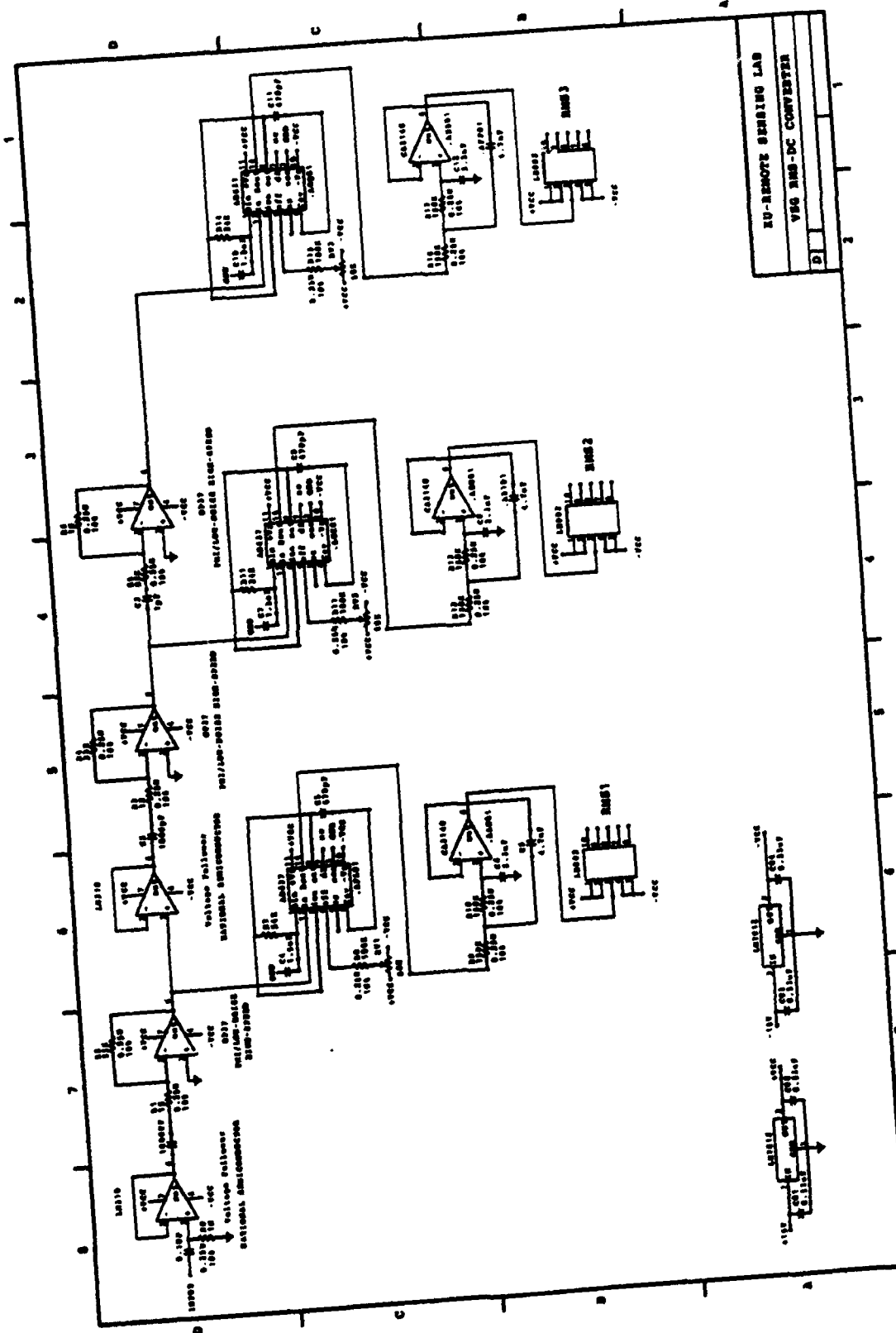












REFERENCES

- Alpers, W.R., and K. Hasselmann, "The two-frequency microwave technique for measuring ocean wave spectra from an airplane or satellite," *Boundary Layer Meteorol.*, vol. 13, pp. 215-230, 1978.
- Alpers, W.R., D.B. Ross, and C.L. Rufenach, "On the detectability of ocean surface waves by real and synthetic aperture radar," *J. Geophys. Res.*, vol 86, pp. 6481-6498, 1981.
- Barton, D. K., and H.R. Ward, *Handbook of Radar Measurement*, Artech House Inc., Dedham, Ma, 1984
- Bass, F.G., I.M. Fuks, A.I. Kalmykov, I.E. Ostrovski, and A.S. Rosenberg, "Very high frequency radiowave scattering by the disturbed sea surface," *IEEE Trans. Ant. and Prop.*, vol. AP-16, pp 554-568, 1968.
- Bendat, J.S., and A.G. Piersol, *Measurement and analysis of random data*, Jhon Wiely, New York, 1971.
- Bilotti, A., "FM Detection Using a Product Detector," Proc. IEEE, 56, pp. 755-757, April 1968.
- Bush, D. A., "A video-aided study of sea spikes on radar backscatter at moderate incidence," MS Thesis in Electrical Engineering, University of Kansas, 1990.
- Clarke K.K., and D.T. Hess, *Communication Circuits: Analysis and Design*, Addison-Wesley Publishing Company, Reading Massachusetts, 1978.
- Donelan, M.A. and W.J. Pierson, Jr., "Radar scattering and equilibrium ripples in wind-generated waves with application to scatterometry," *J. Geophys. Res.*, vol. 92, pp 4971-5029, 1987.
- Feident, F., J. Schroter, and W. Alpers, "Measurement of the ocean wave-radar modulation transfer function at 35 GHz from a sea-based platform in the North sea," *J. Geophys. Res.*, vol. 91, no. C8, pp. 9701-9708, 1986.
- Fung, A. K. and H. J. Eom, "An approximate model for backscattering and emission from land and sea," in *IGARSS' 81 Digest*, vol. I, 1981, pp. 620-628.

- Gardner, F.M., *Phaselock Techniques*, John Wiley & Sons, New York, 1967.
- Hasselmann K., R.K. Raney, W.J. Plant, W. Alpers, R.A. Shuchman, D.R. Lyzenga, C.L. Rufenach, and M.J. Tucker, "Theory of synthetic aperture radar ocean imaging: A MarSEN view," *J. Geophys. Res.*, vol. 90, pp. 4659-4686, 1985.
- Hesany, V. and R.K. Moore, "Modulation Transfer Functions of radar return power from the ocean," *Proceedings of IGARSS*, vol. 2, Ann Arbor, Michigan, pp. 993-998, 1987.
- Hesany V., R.K. Moore, S.P. Gogineni, "Slope-induced nonlinearities on imaging of ocean waves," *IEEE J. of Oceanic Engineering*, vol. 16, no. 3, pp. 279-284, July 1991.
- Hesany, V., R. K. Moore, and S. Haimov, "Comparison of slope, waveheight, and radar spectra, slope and hydrodynamic modulation of radar scatter from the sea," *IGARSS'92*, Houston Texas, May 1992.
- Hesany, V., B. Sistani, S. Haimov, and R. K. Moore, "Modulation Transfer Functions at Ka Band," *IGARSS'92*, Houston Texas, May 1992.
- Jähne, B., and K.S. Riemer, "Two-dimensional wave number spectra of small-scale water surface waves," *J. Geophys. Res.*, vol. 95, pp 11531-11546, 1990.
- Jackson, F.C., W.T. Walton, and P.L. Baker, "Aircraft and satellite measurements of ocean wave directional spectra using scanning beam microwave radar," *J. Geophys. Res.*, vol 90, pp 987-1005.
- Jessup, A. T., W. C. Keller, and W. K. Melville, "Measurements of sea spikes in microwave backscatter at moderate incidence," *J. Geophys. Res.*, vol. 95, no. C6, pp. 9679-9688, June 1990.
- Kalmykov A.I., S.A. Velichko, V.N. Tsymbal, A.Y. Kuleshov, A.J. Weinman, "Observation of the marine environment from spaceborne side-looking real aperture radars," *Remote Sensing of Environment*, vol. 45, no. 2, pp. 193-208, Aug. 1993.
- Keller, W.C., W.J. Plant, and D.E. Weissman, "The dependence of X band microwave sea return on atmospheric stability and sea state," *J. Geophys. Res.*, vol. 90, no. C1, pp. 1019-1029, July 1985.

- Keller, W. C. and J. W. Wright, "Microwave scattering and the straining of wind-generated waves," *Radio Sci.*, vol. 10, pp. 139-147, 1975.
- Kitaigorodskii, S.A., "On the theory of the equilibrium range in the spectrum of wind-generated waves," *J. Phys. Oceanography*, vol 13, pp. 816-828, 1983.
- Khan, Fitratullah, "A Data Aquisition/Controller System," RSL Techincal Report, University of Kansas, January 1992.
- Kitaigorodskii,S.A., " The equilibrium range in the spectrum of wind generated waves," *J. Phys. Ocean.*, vol 13, pp. 816-827, 1983.
- Lawner, R.T. and R.K. Moore, " Short gravity and capillary wave spectra from tower-based radar," *IEEE J. Oceanic Eng.*, vol OE-9, 317-324.
- Long, M.W., *Radar Reflectivity of Land and Sea*, Lexington, Massachusetts, 1975.
- Longuet-Higgins, M.S, D.E. Cartwright, and N.D. Smith, Observation of the directional spectrum of sea waves using the motions of a floatong buoy, *Ocean Wave Spectra*, Englewood Cliffs, N.J., Prentice Hall, Inc., pp. 111-132, 1961.
- Marsden, R.F, and B.A. Juszko, " An eigenvector method for the calculation of the directional spectra from Heave, Pitch and Roll Buoy Data," *J. Phys. Oceanogr.*, No. 17, pp 2157-23167, 1987.
- Ocampo-Torres, F.J., and I.S. Robinson,"wind wave directionality effects on the radar imaging of ocean swells," *J. Geophys. Res.*, vol 95, 20347-20362, 1990.
- Oltman-Shay, J., and R.T. Guza, "A data-adaptive ocean wave direction estimator for pitch and roll measurements," *J. Phys. Oceanogr.*, No. 14, pp 1800-1810, 1984.
- Phillips, O.M., "The structure of short gravity waves on the ocean surface,"in *Spaceborne Synthetic Aperture Radar for Oceanography*; Beal, De leonibus and Katz (Eds.), John Hopkins Press, pp. 24-31, 1981.
- Phillips, O. M., *The Dynamics of the Upper Ocean*, Cambridge University Press, Cambridge, UK, 1977.
- Phillips, O.M., "The equilibrium range in the spectrum of wind-generated waves," *J. Fluid Mech.*, vol 4, pp. 426-434, 1958.

- Plant, W.J., W.C. Keller, and J.W. Wright, "Modulation of coherent microwave backscatter by scrolling waves," *J. Geophys. Res.*, vol 83, pp. 1347-1352, 1978.
- Plant, W.J., and W. Alpers, "The SAXON-FPN experiment," *IGARSS'91 Digest*, Espoo, Finland, pp 1983-1986, 3-6 June 1991.
- Plant, W.J., and W.C. Keller, "Parametric dependence of ocean wave radar modulation transfer functions," *J. Geophys. Res.*, vol. 88, pp. 9747-9756, 1983.
- Plant, W.J., "Comment on 'wind wave directionality on the radar imaging of ocean swells' by F.J. Ocampo-Torres and I.S. Robinson," *J. Geophys. Res.*, vol. 96, pp. 18527-18529, 1991.
- Plant, W.J., and W. Alpers, "The SAXON-FPN experiment," *Proceedings of IGARSS'91*, p. 1983, Espoo, Finland, 1991.
- Populis, A., *Probability, Random Variables, and Stochastics Processes*, McGraw-Hill Book Company, New York, 1965.
- Rauch, Sol, and Howard A. Grant, "Performance Analysis of the Modulation Cancellation Altimeter," *IEEE Trans. on Aerospace and Electronic Systems*, vol. 7, no. 2, March 1971.
- Rice, D.W., and K.H. Wu, "Quadrature Sampling with High Dynamic Range," *IEEE Trans. on Aerospace and Electronic sys.*, vol. 18, no. 6, November 1982.
- Rummer, D., V. Khan, B. Sistani, A. Salam, and C. Roberts, "A data acquisition/controller system for scatterometers," *Proceedings of the URSI/Commission-F-sponsored, Microwave Signatures Conference*, Igls-Innsbruck Austria, July 1992.
- Salam, A., S. Haimov, V. Hesany , "Sea spikes at moderate incidence and their relation to position on the waves," *IGARSS'92*, Houston, Texas, May 26-29, 1992.
- Schroter,J., F. Feindt, A. Alpers, W.C. Keller, "Measurement of the Ocean wave-radar modulation transfer functions at 4.3 Ghz," *J. Geophys. Res.*, vol 91, no. C1, pp 923-932, 1986.
- Sistani, B., "Measurement and analysis of ocean-radar modulation transfer function at Ka-band (SAXON-FPN experiment)," MS thesis, University of Kansas, 1993.

Skolnik, M. I., *Introduction to Radar Systems*, New York, McGraw-Hill Inc., 1980.

Ulaby, F.T., R.K. Moore, and A.K. Fung, *Microwave Remote Sensing*, Vol. II, Artech House, Norwood, Massachusetts, 1982.

Valenzuela, G.R., "Theories for the interaction of electromagnetic and oceanic waves - A review," *Boundary Layer Meteorology*, vol 13, pp 61-85, 1978.

Valenzuela, G.R., "The growth of gravity-capillary waves in a couples shear flow," *J. Fluid Mech.*, vol. 76, pp. 229-250, 1976.

Waters, W.M., and B.R. Jarrett, "Bandpass Signal Sampling and Coherent Detection," *IEEE Trans. on Aerospace and Electronic sys.*, vol. 18, no. 6, November 1982.

Wright, J. W., "A new model for sea clutter," *IEEE Trans. on Ant. Prop.*, vol. AP-16, pp. 217-223, 1968.

Wright, J. W., W. J. Plant, W. C. Keller, and W. L. Jones, "Ocean wave-radar modulation transfer functions from the west coast experiment," *J. Geophys. Res.*, vol. 85, no. C9, pp. 4957-4966, September 1980.

Wright, J. W., "Backscattering from capillary waves with application to sea clutter," *IEEE Trans. on Ant. Prop.*, vol. 14, pp. 749-754, 1966.

Yousefi, E., "SAXON-FPN: University of Kansas Vector Slope Gauge Data," RSL Techinal Report 8620-2, University of Kansas, September 1992.